

ELECTRON PARAMAGNETIC RESONANCE STUDIES OF SYMMETRY ENFORCED  
QUANTUM TUNNELING IN MOLECULE-BASED MAGNETS

By

JUNJIE LIU

A DISSERTATION PRESENTED TO THE GRADUATE SCHOOL  
OF THE UNIVERSITY OF FLORIDA IN PARTIAL FULFILLMENT  
OF THE REQUIREMENTS FOR THE DEGREE OF  
DOCTOR OF PHILOSOPHY

UNIVERSITY OF FLORIDA

2012

© 2012 Junjie Liu

To my parents

## ACKNOWLEDGMENTS

I would like to take this opportunity to acknowledge many people who have directly or indirectly helped me during my five years PhD life in the University of Florida and the National High Magnetic Field Laboratory at Tallahassee.

I am deeply indebted to my PhD advisor, Prof. Stephen Hill, for his patient guidance and continuous support during the past four years. I joined Prof. Hill's group in 2008 knowing very little about experimental condensed matter physics. Prof. Hill mentored me patiently through my graduate studies and gave me lots of helpful suggestions for my research. Furthermore, he also provided me with financial support so I could focus on my research. In addition, I was afforded the opportunity to attend several conferences, both regional and international, where I was able to interact with some of the best-known experts in our field. Prof. Hill had a profound effect on my English skills, both written and spoken, and for this I am truly thankful.

I would like to thank Prof. David Tanner for willing to serve as my PhD committee chair and helping me through the last three years. Without his support, it is impossible for me finish my graduate study at UF.

I would like to thank the other members of my PhD committee who monitored my PhD studies and provided me with valuable suggestions and comments on my dissertation: Prof. Hai-Ping Cheng, Prof. Christopher Stanton and Prof. George Christou.

During my PhD studies, I was lucky to that I had chances to work with many research groups, both in condensed matter physics and in chemistry. It has been a privilege to work with them. I would like to express my thanks to my collaborator Prof. Enrique del Barco and his group at the University of Central Florida. We have collaborated in several projects and I was always able to learn a lot from our discussions. Prof. Guillem Aromi, Prof. Euan K. Brechin,

Prof. David Hendrickson and Prof. Jeffery Long have provided me with samples to study. I am really grateful to them for the collaborations.

I want to thank all the former and current group members, especially Dr. Saiti Datta and Dr. Changhyun Koo, who taught me the basic skills about being an experimental physicist. I wish them have a great career. Dr. Christopher Beedle, who is the only expert in chemistry in our group, helped me a lot with chemistry and my written English. Dr. Alexey Kovalev is an excellent experimental physicist, who I have learnt a lot from our discussions. My labmates, Sanhita Ghosh and Muhandis Muhandis, had provided me many helps for my experiments. I also want say thank you to the scientists in the EMR group at the NHMFL for their helps and all the meaningful discussions.

I would like to acknowledge the US NSF (grant number DMR-0804408 and CHE-0924374) for the financial supports. The NHMFL is supported by the NSF (DMR-0654118) and the State of Florida.

Last, but not least, I would like to thank my parents. Through all the years, they have always been supportive of me, encouraging me and loving me. We are nothing without our family. I wish they have a happy life and I will always love them.

## TABLE OF CONTENTS

	<u>page</u>
ACKNOWLEDGMENTS .....	4
LIST OF TABLES .....	8
LIST OF FIGURES .....	9
LIST OF ABBREVIATIONS.....	12
ABSTRACT.....	13
<b>CHAPTER</b>	
<b>1 INTRODUCTION TO MOLECULE-BASED MAGNETS .....</b>	<b>16</b>
1.1 Introduction.....	16
1.2 Spin Hamiltonian .....	18
1.2.1 Giant-Spin Approximation Hamiltonian .....	19
1.2.1.1 Second Order Anisotropies .....	19
1.2.1.2 High-Order Anisotropies.....	23
1.2.2 Multi-Spin Hamiltonian.....	25
1.3 Experimental Techniques in Studying SMMs.....	26
1.3.1 Electron Paramagnetic Resonance .....	27
1.3.2 Quantum Tunneling of Magnetization .....	29
1.4 Single-Chain Magnets .....	35
<b>2 INTERPLAY BETWEEN ANISOTROPY AND EXCHANGE IN DINUCLEAR MOLECULAR MAGNETS .....</b>	<b>49</b>
2.1 Introduction.....	49
2.2 Ferromagnetically Coupled Dinuclear [Mn <sup>III</sup> ] <sub>2</sub> Molecule .....	51
2.2.1 Discussions of Magnetometry Results .....	51
2.2.1 EPR Spectroscopy .....	54
2.3 Antiferromagnetically Coupled Dinuclear [Mn <sup>III</sup> ] <sub>2</sub> Molecule .....	58
2.3.1 EPR Spectroscopy .....	59
2.3.2 Magnetic Measurements.....	67
2.4 Summary.....	69
<b>3 QUANTUM TUNNELING OF MAGNETIZATION IN TRIGONAL SINGLE- MOLECULE MAGNETS .....</b>	<b>79</b>
3.1 Introduction.....	79
3.2 Quantum Tunneling of Magnetization in the Mn <sub>3</sub> Single-Molecule Magnet.....	80
3.2.1 The Mn <sub>3</sub> Single-Molecule Magnet .....	80
3.2.2 Quantum Tunneling of Magnetization in Mn <sub>3</sub> .....	82

3.2.3 Berry-Phase Interference in Mn <sub>3</sub> .....	87
3.3. Quantum Tunnel of Magnetization in the Ni <sub>4</sub> Single-Molecule Magnet .....	89
3.3.1 The Ni <sub>4</sub> Single-Molecule Magnet.....	89
3.3.2 Quantum Tunneling of Magnetization in Ni <sub>4</sub> .....	91
3.4 Summary.....	94
4 ELECTRON PARAMAGNETIC RESONANCE AND QUANTUM TUNNELING OF MAGNETIZATION STUDIES OF MN <sub>4</sub> SINGLE-MOLECULE MAGNETS: REVEALING COMPETING ZERO-FIELD INTERACTIONS.....	108
4.1 Introduction.....	108
4.2 The Mn <sub>4</sub> -Bet SMM .....	111
4.2.1 The Structure of the Mn <sub>4</sub> -Bet SMM.....	111
4.2.2 Discussion of Electron Paramagnetic Resonance Results.....	114
4.2.3 Discussion of Quantum Tunneling of Magnetization Results.....	119
4.3 Summary.....	124
5 SLOW MAGNETIC RELAXATION INDUCED BY A LARGE TRANSVERSE ZERO-FIELD SPLITTING IN A MN <sup>II</sup> RE <sup>IV</sup> (CN) <sub>2</sub> SINGLE-CHAIN MAGNET .....	135
5.1 Introduction.....	135
5.2 Introduction to the Structures of 1-4.....	138
5.3 Discussions of Magnetometry and EPR Results .....	139
5.3.1 Complex 1 .....	139
5.3.2 Complex 2 .....	142
5.3.3 Complex 3 .....	143
5.4 Discussion of the Magnetic Relaxation Process.....	146
5.5 Summary.....	149
6 SUMMARY.....	161
APPENDIX STEVENS OPERATORS .....	164
LIST OF REFERENCES.....	166
BIOGRAPHICAL SKETCH .....	173

## LIST OF TABLES

<u>Table</u>		<u>page</u>
3-1	Comparison of tunneling gaps obtained from the MS and GS models for resonances $k = 0, 1, 2$ and $3$ , for the two cases $\theta = 0$ (top) and $\theta = 8.5^\circ$ (bottom). .....	84
5-1	Selected Interatomic Distances ( $\text{\AA}$ ) and Angles ( $^\circ$ ) for compounds 1-4.....	139

## LIST OF FIGURES

<u>Figure</u>	<u>page</u>
1-1 The molecular structures of several SMMs studied in this dissertation. ....	39
1-2 Schematic representation for the energy levels of an $S = 6$ molecule with easy-axis type anisotropy ( $D < 0$ ). ....	40
1-3 Potential energy surface corresponding to the 2 <sup>nd</sup> -order anisotropy. ....	41
1-4 Potential energy surfaces corresponding to the fourth order Stevens operators. ....	42
1-5 Schematic sketches demonstrating the concept of the MS Hamiltonian for a trinuclear molecule. ....	43
1-6 Schematic plots illustrating the theory of EPR measurements. ....	44
1-7 Quantum tunnel of magnetization in a $S = 6$ SMM. ....	45
1-8 The tunnel splitting associated with QTM. ....	46
1-9 A schematic sketch of various tunneling paths on a Bloch sphere. ....	47
1-10 The process of the relaxation of magnetization in SCMs. ....	48
2-1 The molecular structure and magnetic core of complex <b>1</b> . ....	70
2-2 Hard plane EPR spectra of complex <b>1</b> obtained at 171 GHz as a function of temperature from 20 K (top) to 2.5 K (bottom). ....	71
2-3 Representative easy axis EPR spectra of complex <b>1</b> obtained at 2 K (391.5 GHz) and 15 K (310.1GHz and 248.6 GHz). ....	72
2-4 Frequency dependence of EPR peak positions of <b>1</b> . ....	73
2-5 The molecular structure of complex <b>2</b> . ....	74
2-6 EPR spectrum of complex <b>2</b> as a powder at 652.8GHz and 10 K, recorded in the first-derivative mode. ....	75
2-7 Single-crystal EPR studies for complex <b>2</b> . ....	76
2-8 Powder EPR studies for complex <b>2</b> . ....	77
2-9 Plot of the isofield reduced magnetization measurements. ....	78
3-1 The molecular structure and the magnetic core of the $Mn_3$ SMM. ....	95

3-2	Zeeman diagram for a spin $S = 6$ multiplet with easy-axis anisotropy ( $D < 0$ in Equation 3-1) and $H//z$ .....	96
3-3	Zeeman diagram of $Mn_3$ generated by Equation 3-2 with different magnitudes of $J$ .....	97
3-4	The symmetries of the ZFS interactions and the tunnel splittings.....	98
3-5	Tunnel splittings of the $Mn_3$ SMM as a function of the coupling constant $J$ .....	99
3-6	Color contour polar plot of the ground state $\Delta_{\bar{66}}$ gap as a function of $H_T$ , calculated using Equation 3-1 with $B_4^3 = 0$ .....	100
3-7	Shift of $H_L$ for $\Delta_{\bar{66}}$ as a function of the magnitudes of the applied $H_T$ .....	101
3-8	The BPI patterns for the ground QTM resonances of the $Mn_3$ SMM.....	102
3-9	The structure and the magnetic core of the $Ni_4$ SMM.....	103
3-10	Zeeman diagram for the $Ni_4$ SMM simulated employing Equation 3-3.....	104
3-11	The ground state QTM gaps for the $Ni_4$ SMM as a function of $H_T$ .....	105
3-12	Color contour polar plot of the ground $\Delta_{k=0}$ gap as a function of $H_T$ , calculated using Equation 3-3 with the parameters given in the main text.....	106
3-13	The effect of disorder on the ground state QTM gaps for the $Ni_4$ SMM.....	107
4-1	The molecular structures and the magnetic cores of the $Mn_4$ SMMs.....	125
4-2	Temperature dependent EPR spectra for $Mn_4$ -Bet obtained at 139.5 GHz with the applied field close to the molecular easy-axis.....	126
4-3	Temperature dependent EPR spectra for $Mn_4$ -Bet obtained at 67.3 GHz with the applied field in the molecular hard-plane.....	127
4-4	Zeeman diagram for the ground multiplet ( $S = 9$ ) of $Mn_4$ -Bet with the field applied in the molecular $xy$ -plane.....	128
4-5	Temperature dependence of the EPR spectra for $Mn_4$ -anca.....	129
4-6	Plots of frequency versus field for $Mn_4$ -Bet showing the observed ground state EPR peak positions.....	130
4-7	Hysteresis loops for $Mn_4$ -Bet recorded as a function of $H_L$ at different temperatures.....	131
4-8	Modulation of the QTM probabilities for resonances of $Mn_4$ -Bet.....	132

4-9	Contour plots of the QTM probabilities for resonances $k = 0$ and $k = 1$ of $Mn_4$ -Bet as a function of $H_T$ and $\Phi$ .....	133
4-10	Simulations of the magneto-anisotropy and QTM probabilities of $Mn_4$ -Bet. ....	134
5-1	The structures of complexes <b>1-4</b> presented in Chapter 5.....	151
5-2	The EPR studies for complex <b>1</b> . ....	152
5-3	Temperature dependence spectra for <b>1</b> collected at $f = 126.9$ GHz.....	153
5-4	Frequency dependence of the high-frequency EPR peak positions deduced from studies of a powder sample of <b>1</b> at 5 K.....	154
5-5	Zeeman diagram for complex <b>1</b> generated employing Equation 5-1 with $D = +15.8$ K and $g_z = 1.58$ . ....	155
5-6	Frequency dependence of the EPR peak positions deduced from powder studies of complex <b>2</b> at 5 K.....	156
5-7	Frequency dependence of the EPR peak positions obtained from studies of a powder sample of <b>3</b> at 3.5 K.....	157
5-8	Structure and spin arrangement of chain compound <b>4</b> .....	158
5-9	The ground tunnel splitting as a function of the size ( $N$ ) of the SCM.....	159
5-10	Classical magneto-anisotropy energy surface corresponding to the zero-field operator equivalent terms given in Equation 5-1. ....	160

## LIST OF ABBREVIATIONS

EPR	Electron Paramagnetic Resonance
GSA	Giant-Spin Approximation
JT	Jahn-Teller
MS	Multi-Spin
QTM	Quantum Tunneling of Magnetization
SCM	Single-Chain Magnet
SMM	Single-Molecule Magnet
ZFS	Zero-Field Splitting

Abstract of Dissertation Presented to the Graduate School  
of the University of Florida in Partial Fulfillment of the  
Requirements for the Degree of Doctor of Philosophy

ELECTRON PARAMAGNETIC RESONANCE STUDIES OF SYMMETRY ENFORCED  
QUANTUM TUNNELING IN MOLECULE-BASED MAGNETS

By

Junjie Liu

May 2012

Chair: David Tanner  
Cochair: Stephen Hill  
Major: Physics

This dissertation presents studies of several molecule-based magnets using both experimental and theoretical methods to understand the quantum tunneling and thermally assisted magnetic relaxation at the single-ion level. The molecule-based magnets presented in this dissertation can be sorted into two categories: a) single-molecule magnets (SMMs) and b) single-chain magnets (SCMs). In these systems, the quantum tunneling and thermally assisted magnetic relaxation play critical roles both in terms of fundamental scientific reasons and due to the potential applications of SMMs and SCMs in information technologies. Electron paramagnetic resonance (EPR) and quantum tunneling of magnetization (QTM) were employed as two spectroscopic techniques to probe the rich physics of these magnetic materials.

Detailed EPR measurements were performed on two dinuclear  $[\text{Mn}^{\text{III}}]_2$  molecular magnets to study the interplay between magnetic anisotropy and exchange interactions. These results show the importance of considering both interactions in interpreting magnetometry measurements performed at both high and low temperatures. The presented analyses shows that EPR is a particularly powerful technique for determining magneto anisotropies, as well as

magnetic exchange interactions, in weakly coupled systems; furthermore, these studies paved the way for using EPR to study magneto-structural correlations under pressures in these compounds.

Theoretical studies regarding quantum tunneling in SMMs were conducted on a trinuclear  $[\text{Mn}^{\text{III}}]_3$  SMM with idealized  $C_3$  symmetry. We considered the origin of the three-fold transverse anisotropy by mapping the spectrum of the ground spin multiplet generated by a multi-spin Hamiltonian onto that of a giant-spin approximation Hamiltonian. The rotation of the easy-axes of the individual ions leads to the emergence of a three-fold transverse anisotropy term,  $\hat{O}_4^3$ , which unfreezes  $k$ -odd resonance ( $k = m + m'$ , where  $m$  and  $m'$  are the spin projections of the states involved in the QTM resonance) and shifts the ground  $k = 0$  QTM resonance away from zero longitudinal field. For comparison, theoretical studies of quantum tunneling in a tetranuclear  $[\text{Ni}^{\text{II}}]_4$  SMM were performed. In these studies we considered the effects of disorder, which significantly change the QTM selection rules.

EPR studies were performed on two tetranuclear  $[\text{Mn}_2^{\text{II}}\text{Mn}_2^{\text{III}}]$  SMMs,  $\text{Mn}_4\text{-Bet}$  and  $\text{Mn}_4\text{-anca}$ , to probe the magneto anisotropies of these molecules. The Berry-phase interference (BPI) patterns were measured in QTM experiments as a function of the transverse field for the  $\text{Mn}_4\text{-Bet}$  complex, leading to the first observation of an intriguing motion of the BPI minima in the magnitude-direction phase space of the applied transverse field in SMMs. This motion was attributed to the competition between the zero-field anisotropies of inequivalent magnetic ions,  $\text{Mn}^{\text{III}}$  and  $\text{Mn}^{\text{II}}$ , within the molecule.

Finally, we considered the thermally assisted magnetic relaxation dynamics in a  $\text{Re}^{\text{IV}}$  based SCM. EPR studies of molecules mimicking fragments of this chain suggest that the  $\text{Re}^{\text{IV}}$  ions in these compounds possess an easy-plane type anisotropy and a significant transverse anisotropy. Theoretical analyses reveal that quantum tunneling is suppressed in the one-dimensional chain,

which leads to the observation of slow magnetic relaxation in an easy-plane type system. Within this picture, it is the transverse anisotropy which gives rise to the anisotropy barrier for the relaxation of spins. These results demonstrate the first example of slow magnetic relaxation through transverse anisotropy; thus, it provides a new strategy for the design of single-chain magnets.

# CHAPTER 1 INTRODUCTION TO MOLECULE-BASED MAGNETS

## 1.1 Introduction

Rapid developments of molecule-based magnets have attracted much interest in the past two decades due to both fundamental scientific reasons<sup>1</sup> and their potential applications in information technologies<sup>2,3</sup>. A particularly appealing area in molecule-based magnets is the study of single-molecule magnets (SMMs) which exhibit slow relaxation of magnetization<sup>4</sup> and magnetization hysteresis loop<sup>5</sup> at the molecular level at low temperatures. The SMMs' capability of preserving spin polarizations without application of external fields places them as candidates for high-density spin-based information storage materials. Their discovery has motivated chemists in designing and synthesizing new SMMs as well as physicists who work on interpreting their novel properties.

The magnetic properties of a SMM mostly originated from its magnetic core, which is constituted by magnetic ions with unpaired electrons. The core of a SMM is surrounded by large non-magnetic ligands which minimize inter-molecular interactions. The most important feature of SMMs is that the slow relaxation of magnetization and hysteresis have a molecular origin, as confirmed by the observation of these phenomena in dilute frozen solutions.<sup>6,7</sup> The first SMM,  $[\text{Mn}_{12}\text{O}_{12}(\text{CH}_3\text{COO})_{16}(\text{H}_2\text{O})_4] \cdot 2\text{CH}_3\text{COOH} \cdot 4\text{H}_2\text{O}$  (hereafter  $\text{Mn}_{12}\text{Ac}$ ), was first synthesized in 1980.<sup>8</sup> However, it was not identified as a SMM until more than a decade later, when slow relaxation of magnetization was observed in ac susceptibility measurements.<sup>4</sup> Since then, many SMMs with various topologies and magnetic cores have been synthesized and studied<sup>9-17</sup> in order to increase the blocking temperature,  $T_B$ , below which the relaxation of magnetization in a SMM becomes slow. However, the record of  $T_B$  set by  $\text{Mn}_{12}\text{Ac}$ <sup>18,19</sup> remained unbroken until a  $\text{Mn}_6$  SMM was synthesized by Brechin and his collaborators<sup>15</sup>. Recently, studies on lanthanide-based

SMMs have yielded several groundbreaking results which have led to substantial improvements of  $T_B$ .<sup>20-27</sup>

The SMMs presented in this dissertation possess magnetic cores which are constituted by transition metal ions coupled through chemical bonds. Figure 1-1 shows the structures of several SMMs which will be studied in this dissertation; detailed descriptions of these molecules are presented in the following chapters. The sizes of atoms in Figure 1-1 have been adjusted to emphasize the transition metal ions, i.e., the magnetic cores of these molecules. Instead of pursuing high  $T_B$ , which is critical for applications of SMMs in information technology, the studies presented in this dissertation focus on understanding fundamental quantum mechanical phenomena in SMMs. To achieve this, we studied SMMs with relatively simple magnetic cores (2~4 magnetic ions or 1D chains). The simple structures of these SMMs allow one to clearly understand several nanoscale quantum phenomena, which are often obscured by structural complexities in large SMM clusters.

A SMM is usually characterized by the two features:

- (a) a high spin ground state ( $S$ ),
- (b) significant negative uniaxial magnetic anisotropy ( $D$ )

As shown in Figure 1-2, the combination of  $S$  and  $D$  gives rise to a parabolic shape energy barrier ( $\Delta$ ) between the “spin up” and “spin down” states which leads to a magnetic bistability at low temperatures. Supposing all the molecules are magnetized in one orientation (up), at zero field, in order for the spins to relax to the opposite orientation (down), they must obtain enough energy to jump over the relaxation barrier. Such a process is thermally activated and, thus, suppressed with decreasing temperature. The characteristic relaxation time for such a process follows the Arrhenius Law that:

$$\tau = \tau_0 \exp(\Delta/k_B T) \quad (1-1)$$

where  $\tau_0$  is independent of temperature. Roughly speaking,  $\Delta$  equals to  $|D|S^2$  for integer spins and  $|D|(S^2-1/4)$  for half-integer spins. As shown by Equation 1-1, the relaxation time grows exponentially as the temperature decreases; thus, at very low temperatures, a SMM can be treated as a permanent magnet.

Another source of magnetization relaxation in SMMs is the quantum tunneling of magnetization (QTM).<sup>28</sup> Unlike the thermally assisted relaxation process, QTM is a purely quantum-mechanical effect which is temperature-independent if only ground state tunneling is involved. The theorem of QTM will be discussed in more detail later in this chapter.

## 1.2 Spin Hamiltonian

In order to explain the magnetic properties of SMMs, one needs to introduce a proper Hamiltonian to describe a SMM. A widely used approach involves a spin Hamiltonian, which ignores the orbital angular momentum of the constituent atoms and treats the system as its total angular momentum is contributed only by spins. Such an approximation is valid when the orbital angular momentum is quenched, which is a good approximation for all the SMMs presented in this dissertation.

The spin Hamiltonian can be divided into two parts:  $\hat{H} = \hat{H}_{\text{ZFS}} + \hat{H}_{\text{Zeeman}}$ . The first part is the zero-field Hamiltonian which corresponds to the zero-field splittings (ZFS) originating from spin-orbit interactions and the super exchange interactions. The second part characterizes the Zeeman interaction with an applied external magnetic field. In this dissertation we introduce two types of spin Hamiltonian: the giant-spin approximation (GSA) Hamiltonian and the multi-spin (MS) Hamiltonian. Both Hamiltonians are used in data interpretations and the correlations between these two types of Hamiltonian are discussed in this dissertation.

### 1.2.1 Giant-Spin Approximation Hamiltonian

For a polymetallic SMM, the total magnetic moment varies depending on the relative alignment of spins within the molecule. If the ground spin state is well defined and separated from other excited spin states, only the ground spin multiplet is thermally populated at low temperatures. In this case, it is reasonable to treat the spin of the molecule as a rigid number and neglect all other excited spin multiplets. This approximation is called the giant-spin approximation (GSA).

A convenient way for exploiting SMMs with a GSA Hamiltonian is by using the so-called Stevens operators.<sup>29</sup> The zero-field spin Hamiltonian of a molecule is given by:

$$\hat{H} = \sum_p \sum_{q=0}^p B_p^q \hat{O}_p^q \quad (1-2)$$

$B_p^q$  are anisotropy parameters and  $\hat{O}_p^q$  are Stevens operators. The explicit forms of the Stevens operators (up to the 6<sup>th</sup>-order) are included in Appendix A; more generalized forms of Stevens operators can be found elsewhere<sup>30</sup>. The subscript,  $p$ , is a positive even-integer which stands for the order of the Stevens operator. Due to the fact spin-orbit interaction are invariant under time reversal, the order of the Steven operator must be even. For a molecule with spin  $S$ , the highest order of Stevens operator is limited by  $S$ , where  $2 \leq p \leq 2S$ . The superscript,  $q$ , denotes the rotational symmetry of the operator about the  $z$ -axis.

#### 1.2.1.1 Second Order Anisotropies

Even though high order Stevens operators ( $p \geq 4$ ) are allowed for a molecule with  $S \geq 2$ , it is not always necessary to include all of them up to  $p = 2S$ . For SMMs constituted by transition metal ions, the dominant energy scales are usually determined by the second order anisotropies. Therefore, the simplest zero-field GSA Hamiltonian used in characterizing SMMs can be written as:

$$\hat{H}_{\text{zfs}} = D\hat{S}_z^2 + E(\hat{S}_x^2 - \hat{S}_y^2) \quad (1-3)$$

Equation 1-3 includes only the second order anisotropies, where  $D$  is the second order uniaxial anisotropy ( $D = 3B_2^0$ ) and  $E$  is the second order rhombic anisotropy ( $E = B_2^2$ ). In an axial system,  $D$  is the dominant anisotropy and the  $z$ -axis is chosen as the quantization axis. The magnitude of  $E$  is restricted by the ratio between  $E$  and  $D$  where  $|E/D| < 1/3$ ; otherwise, the quantization axis is no longer the  $z$ -axis and one can rotate the coordinate frame so that  $|E/D| < 1/3$  is satisfied. As can be seen, when  $E = 0$ , Equation 1-3 is diagonal in the  $|m\rangle$  basis where  $m$  is the spin projection onto the molecular  $z$ -axis, and  $m = -S, -S+1 \dots +S$ . The energy of each state is then given by  $\varepsilon(m) = Dm^2$  where the ground states are the  $m = \pm S$  states if  $D < 0$ ; therefore, the  $z$ -axis is the easy-axis (preferred magnetization axis) and the  $xy$ -plane is called the hard-plane. In the situation where  $E$  is non-zero ( $> 0$ ), the  $x$ -axis is called the hard-axis and the  $y$ -axis is the intermediate axis.

One of the major objects of this dissertation is to understand the influences of symmetries on quantum tunneling in SMMs. Hence, it is important to examine the symmetry of Equation 1-3 since, strictly speaking, the symmetry of the Hamiltonian should be compatible to the symmetry of the molecule. In general, a spin Hamiltonian must be invariant under time reversal, which is assured by the nature of spin-orbit coupling. Therefore, any spin Hamiltonian should naturally possess  $C_i$  symmetry, which means a spin Hamiltonian should remain invariant under the reversal of applied fields. Figure 1-3 shows the classical analogy of Equation 1-3, with using  $|E| = |D|/5$  and  $D < 0$ . This analogy is performed by substituting the spin operators in Equation 1-3 by their classical counterpart as follows:

$$\begin{aligned} \hat{S}_x &= S \sin \theta \cos \varphi \\ \hat{S}_y &= S \sin \theta \sin \varphi \\ \hat{S}_z &= S \cos \theta \end{aligned} \quad (1-4)$$

where  $\theta$  and  $\varphi$  are the inclination and azimuthal angles in spherical coordinates, respectively. In this classical analogy, a spin is treated as a macroscopic magnetic moment where all the three components ( $S_x$ ,  $S_y$  and  $S_z$ ) can be determined simultaneously. The surface shown in Figure 1-3 represents the energy of a spin as a function of its orientation, where the radial distance to the surface corresponds to the spin's energy. As shown in Figure 1-3, Equation 1-3 contains the following symmetry elements: a) three orthogonal  $C_2$  axes, which are the  $x$ ,  $y$  and  $z$ -axes and b) three orthogonal mirror planes, which are the  $xy$ ,  $yz$ , and  $zx$ -planes. These symmetry elements, together with the  $C_i$  symmetry, give rise to a  $D_{2h}$  symmetry for Equation 1-3, which is essentially much higher than  $C_i$  symmetry. Consequently, even though Equation 1-3 can successfully account for most of the low temperature magnetic measurements, such as the ac susceptibility and magnetization versus temperature data, it may fail to explain symmetry-sensitive measurements, e.g., Berry-phase interference in quantum tunneling of magnetization and/or electron paramagnetic resonance experiments.

As one may notice from the preceding discussions, the  $B_2^1 \hat{O}_2^1$  ( $\hat{O}_2^1 = [\hat{S}_x \hat{S}_z + \hat{S}_z \hat{S}_x] / 2$ ) term was neglected. The  $\hat{O}_2^1$  operator possesses only  $C_1$  rotational symmetry about the  $z$ -axis; therefore, the symmetry of a second order spin Hamiltonian may be expected to be lower than  $D_{2h}$  when including  $\hat{O}_2^1$ . However, as we will show, the  $\hat{O}_2^1$  term can be annihilated by choosing a proper coordinate frame; hence, a Hamiltonian with 2<sup>nd</sup>-order ZFS anisotropy always possesses  $D_{2h}$  symmetry. To prove this, we write the 2<sup>nd</sup>-order ZFS terms in a more general form which includes  $D$ ,  $E$  and  $B_2^1$ :

$$\hat{H}_{zfs} = \hat{S}' \cdot \vec{D} \cdot \hat{S} \quad (1-5)$$

where  $\vec{D}$  is a  $3 \times 3$  matrix corresponding to the full 2<sup>nd</sup>-order anisotropy tensor. In Equation 1-5,  $D$  and  $E$  are related to the diagonal elements of  $\vec{D}$  while  $B_2^1$  appears as off-diagonal elements, where  $B_2^1 = 2D_{xz} = 2D_{zx}$ . The only restriction on  $\vec{D}$  is that it must be Hermitian in order to guarantee a Hamiltonian that is Hermitian. Therefore, as a property of a Hermitian matrix,  $\vec{D}$  can always be diagonalized by choosing a proper Cartesian coordinate frame, i.e. all the matrix elements except  $D_{xx}$ ,  $D_{yy}$ , and  $D_{zz}$  vanish. By doing so,  $\vec{D}$  can be expressed in a new Cartesian coordinate frame where  $B_2^1 = 0$ . Finally, because the absolute values of energy levels can be arbitrarily chosen, one can subtract  $\frac{1}{2}(D_{xx} - D_{yy})\mathbf{I}$  from  $\vec{D}$  ( $\mathbf{I}$  is the  $3 \times 3$  identity matrix) while the physical properties of the molecule should not be changed. The resultant zero-field Hamiltonian can be written as Equation 1-3 with

$$D = D_{zz} - \frac{1}{2}(D_{xx} + D_{yy}); E = \frac{1}{2}(D_{xx} - D_{yy}) \quad (1-6)$$

Hence, Equation 1-5 is essentially equivalent to Equation 1-3, where only the axial and rhombic anisotropy terms are needed to describe the 2<sup>nd</sup>-order anisotropies; thus, the 2<sup>nd</sup>-order ZFS Hamiltonian must possess at least  $D_{2h}$  symmetry.

The preceding discussions show something considerably important. Even though the dominant energy scales for a SMM are determined by the second order anisotropy, it possesses an artificially high symmetry ( $D_{2h}$ ) which may not be compatible with the structural symmetry of a molecule. The consequences of this symmetry on quantum tunneling will be discussed in more detail in Chapters 3 and 4. Furthermore, in Chapter 4, we will show an example of a SMM which possesses only  $C_i$  symmetry.

### 1.2.1.2 High-Order Anisotropies

For a SMM with  $S$  being equal to or greater than 2, high-order Stevens operators are allowed in the zero-field spin Hamiltonian. The high order anisotropy parameters are usually of orders smaller than the 2<sup>nd</sup>-order anisotropies; however, they can still be clearly observed in spectroscopic type measurements.<sup>31-33</sup> Furthermore, high order anisotropies may introduce several features which cannot be generated by 2<sup>nd</sup>-order anisotropies. The high order axial anisotropies ( $q = 0$ ) lead to a non-parabolic magnetic relaxation barrier which causes non-even spacings between EPR and/or QTM resonance fields (see examples in Chapters 2 and 4), whereas the high order transverse anisotropies ( $q \neq 0$ ) can cause the zero-field spin Hamiltonian to possess a symmetry other than  $D_{2h}$ . In this dissertation, we focus on the changes of symmetry introduced by the inclusion of high order transverse anisotropies. In order to demonstrate the symmetry of high order operators, we show the classical analogies for the potentials of the fourth order Stevens operators in Figure 1-4. The  $\hat{O}_4^0$  operator is not shown since it commutes with  $\hat{S}_z$  and possesses  $C_\infty$  (cylindrical) rotational symmetry. As shown in the figure, all the operators exhibit a rotational symmetry which is compatible with the superscript  $q$ . However, one could note a systematic difference between the  $q$ -odd and  $q$ -even operators. It is clearly shown in the figure that the  $q$ -even operators have the  $xy$ -plane as an additional symmetry plane. In particular, the “nodes” of the  $\hat{O}_4^2$  and  $\hat{O}_4^4$  operators lie within the  $xy$ -plane while the nodes of the  $\hat{O}_4^1$  and  $\hat{O}_4^3$  operators point out of the  $xy$ -plane. The symmetries of these operators can be understood in terms of the combinations of rotational symmetries and the intrinsic  $C_i$  symmetry of spin Hamiltonians. For the  $q$ -even operators, the direct products of the rotational groups and inversion group lead to  $C_2 \times C_i = C_{2h}$  symmetry for  $\hat{O}_4^2$  and  $C_4 \times C_i = C_{4h}$  for  $\hat{O}_4^4$ ; thus, the  $xy$ -plane is introduced as a new symmetry element for  $q$ -even operators. By contrast, for the  $q$ -odd operators,

$C_1 \times C_i = C_i$  for  $\hat{O}_4^1$  and  $C_3 \times C_i = S_6$  for  $\hat{O}_4^3$ ; the resultant symmetry groups corresponding to these operators include an improper rotation ( $C_i$  can be treated as the improper rotation  $S_2$ ). The absence of the  $xy$ -mirror plane in the presence of  $q$ -odd operators implies that the molecular hard plane may not coincide with the  $xy$ -plane, which leads to several intriguing phenomena described in Chapters 3 and 4.

The inclusion of high order Stevens operators has a significant influence on interpreting experimental results for SMMs, especially the data collected in QTM measurements. If a system is limited to 2<sup>nd</sup>-order anisotropies, the zero-field Hamiltonian can only lead to states mixing between energy levels with even  $|\Delta m|$  ( $|\Delta m|$  is the difference between the spin projections of two states), which means quantum tunneling can only occur between states with even  $|\Delta m|$ . However, as we will show in Chapter 3, high-order operators introduce new spin-mixing rules, which can lead to quantum tunneling between odd  $|\Delta m|$  states. Moreover, in systems where the 2<sup>nd</sup>-order rhombic anisotropy is forbidden by structural symmetry,  $m$  is strictly a good quantum number if the Hamiltonian is limited to 2<sup>nd</sup>-order anisotropy; hence, no quantum tunneling should occur. In this circumstance, it is necessary to include high order anisotropies in order to explain experimental results.

The advantage of the GSA Hamiltonian lies in that one only needs to deal with a handful of parameters. The number of zero-field anisotropy parameters involved in data analysis can be restricted by considering the overall symmetry of a molecule. In the GSA Hamiltonian, the Hilbert space only includes the  $2S+1$  states which belong to the ground spin multiplet; therefore, it makes data analyses for complicated large clusters computationally possible. However, the GSA model ignores the internal degrees of freedom within a molecule, thus completely failing to capture the underlying physics in cases where the total spin can fluctuate.<sup>34-36</sup> On the other hand,

when a molecule only possesses  $C_i$  or  $C_1$  structural symmetry, the zero-field anisotropy parameters cannot be restricted on the basis of symmetry, and all possible Stevens operators should be taken into account in data analysis. In these scenarios, it is more reasonable to introduce another kind of spin Hamiltonian for studying SMMs, the multi-spin Hamiltonian.

### 1.2.2 Multi-Spin Hamiltonian

In the multi-spin (MS) model a molecule is treated as a cluster of ions which are coupled with the others through exchange or super-exchange interactions. The corresponding zero-field Hamiltonian is:

$$\hat{H}_{zfs} = \sum_i \hat{s}_i \cdot \vec{R}_i^T \cdot \vec{d}_i \cdot \vec{R}_i \cdot \hat{s}_i + \sum_{i,j,i < j} \hat{s}_i \cdot \vec{J}_{i,j} \cdot \hat{s}_j \quad (1-7)$$

where  $\hat{s}_i$  stands for the spin operator of the  $i^{\text{th}}$  ion.  $\vec{d}_i$  is the 2<sup>nd</sup>-order anisotropy tensor of the  $i^{\text{th}}$  ion. For the reason of simplicity,  $\vec{d}_i$  is written in the diagonal form:

$$\vec{d}_i = \begin{bmatrix} e_i & 0 & 0 \\ 0 & -e_i & 0 \\ 0 & 0 & d_i \end{bmatrix} \quad (1-8)$$

where the local coordinate frame of  $\vec{d}_i$  is chosen to be the local principal anisotropy axes of the  $i^{\text{th}}$  ion.  $\vec{R}_i$  is the Euler rotation matrix specified by the Euler angles  $\theta_i$ ,  $\varphi_i$  and  $\psi_i$  which transform the local coordinate frame of the  $i^{\text{th}}$  ion into the molecular coordinate frame.  $\vec{J}_{i,j}$  is the interaction between the  $i^{\text{th}}$  and  $j^{\text{th}}$  ions. Figure 1-5(a) shows a representative sketch for the MS Hamiltonian of a trinuclear SMM ( $\text{Mn}_3$  in Chapter 3), where the molecule is treated as three coupled anisotropic spins. Figure 1-5(b) illustrate the transformation between the local coordinate frame and the molecular frame via Euler rotations. The black arrows in Figure 1-5(b) represent the molecular coordinate frame while the red arrows represent the local anisotropy axes

of the spin. It should be emphasized that all of the parameters in the MS should be constrained by the structure of a molecule, i.e., the overall symmetry of the Hamiltonian must be compatible with the molecular symmetry.

The MS model considers the internal degrees of freedom within a molecule. Consequently, the MS Hamiltonian can naturally characterize the ground spin multiplet as well as excited spin states, as shown in Figure 1-5(c), which implies that a MS Hamiltonian is capable of describing phenomena where the total spin of a molecule fluctuates. In addition, all of the parameters in the MS Hamiltonian have clear physical relevance, which allows one to understand some in-depth physics in SMMs. By comparing the energy diagrams generated by GSA and MS models, one can track the origin of high order anisotropies in the GSA Hamiltonian and relate them to the molecular structure. For instance, several studies on SMMs have shown that the high order anisotropies arise from the interplay between single-ion anisotropy and magnetic interactions between the ions, which leads to mixing of excited spin states into the ground spin multiplet.<sup>35, 37</sup> In Chapters 3 and 4, we will discuss the emergence of high order anisotropies based on molecular symmetries to demonstrate the correlations between structural symmetry and anisotropy. However, the size of the Hilbert space involved in a MS Hamiltonian grows exponentially as the size of a magnetic core increase, which makes it impractical to apply the MS model to very large systems. Hence, with the exception of Chapter 5, this dissertation is primarily restricted to simple molecules.

### **1.3 Experimental Techniques in Studying SMMs**

The novel properties of SMM have attracted many researchers in the fields of both physics and chemistry to employ various experimental techniques to study them. One of the first landmark experiments was the observation of an unusual out-of-phase signal in the ac susceptibility measurements of  $\text{Mn}_{12}\text{Ac}$ .<sup>4</sup> Since then, numerous types of thermodynamic and

spectroscopic techniques have been applied in the studies of SMMs. In this section we introduce two kinds of spectroscopy, Electron Paramagnetic Resonance (EPR) and Quantum Tunneling of Magnetization (QTM), which are used in the studies presented in this dissertation.

### 1.3.1 Electron Paramagnetic Resonance

Electron Paramagnetic Resonance (EPR) is a microwave spectroscopy technique which is used to study chemical species with unpaired electrons. To illustrate the theorem of EPR measurements on SMMs, we consider a molecule described with the giant-spin Hamiltonian in the presence of an external field. The spin Hamiltonian is:

$$\hat{H} = D\hat{S}_z^2 + \mu_B \mathbf{B} \cdot \vec{g} \cdot \hat{S} \quad (1-9)$$

The second term is the Zeeman interaction where  $\vec{g}$  is the Landé- $g$  tensor. Figure 1-6(a) shows a representative Zeeman diagram simulated with  $S = 6$ ,  $D = -1.2$  K and  $g = 2$ . With the application of an external magnetic field parallel to the  $z$ -axis, the energy levels split into  $2S+1$  non-degenerated states. These states can be labeled according to their spin projections onto the molecular  $z$ -axis,  $m$ . The magnetic dipole radiation selection rule for EPR transitions is  $\Delta S = 0$  and  $|\Delta m| = 1$ , which suggests that it probes transitions between two states within the same spin multiplet. In a typical continuous wave EPR experiment, the frequency of the incident microwaves is fixed while a magnetic field is swept. The transmission microwave signal through the sample is recorded as a function of the applied magnetic field. When the selection rule is satisfied and the energy difference between two states,  $\Delta\varepsilon$ , equals to the incident microwave frequency  $f$  ( $\Delta\varepsilon = hf$ ), a molecule can absorb the incident microwave; this absorption can be observed as a dip in the magnitude of transmission microwave signal. Figure 1-6(b) shows the simulated single-crystal EPR spectrum with  $f = 300$  GHz at the temperature of 15 K upon sweeping the magnetic field up to 10 T. As shown in the figure, a series of equally spaced EPR

transitions is observed. These transitions are labeled  $A_6, A_5 \dots A_2$  where  $A_i$  denotes the transition from  $m = -i$  to  $-(i - 1)$ , where  $m$  is the spin projection onto the quantization axis ( $z$ -axis). In the low-power regime, where there is no saturation effect caused by the incident microwaves, the intensity of an EPR transition,  $I_i$ , is proportional to the difference between the thermo-population of the initial and final states of molecules. In addition,  $I_i$  is proportional to the transition matrix element connecting the initial and final states. Therefore,  $I_i \propto (N_i - N_f) \times \left| \langle f | \hat{H}_{ac} | i \rangle \right|^2$ .  $N_i$  and  $N_f$  stand for the number of molecules at the initial state and final state in the thermo-equilibrium condition, respectively.  $|i\rangle$  and  $|f\rangle$  represent the initial and final states of the molecule, respectively.  $\hat{H}_{ac}$  describes the Zeeman interaction associated with the magnetic fields of the incident microwaves. By comparing EPR spectra collected at various temperatures with the same frequency, the intensity shift between different transitions distinguishes the ground state EPR transition from excited transitions. In EPR performed at the NHMFL, field sweeps are carried out at multiple frequencies to generate a 2D frequency versus field plot where the slopes and intercepts of resonance branches are related to the  $g$ -tensor and zero-field anisotropy parameters, respectively. The magnetic parameters of a molecule can thus be deduced by simulating the frequency dependence and/or the real spectra by using a proper Hamiltonian.

EPR serves as a powerful technique for accurately probing the ground spin states ( $S$ ), the zero-field splitting parameters ( $D, E, B_4^0 \dots$ ), and the Landé  $g$ -tensor for a given SMM. In the studies of SMMs, it is often combined with other magnetic measurements, e.g., susceptibility measurements, to determine the magnetic properties. However, as we mentioned above, the general selection rule for EPR transitions is  $\Delta S = 0$ , which means the transition between different spin multiplets is not usually observed, unless strong  $S$ -mixing presents. Therefore, in the

situations where the interactions between the magnetic ions are strong ( $J \gg d$ ), an EPR measurement is insensitive to the coupling constant  $J$ , where it can be measured by other spectroscopic techniques, e.g., inelastic neutron scattering.<sup>38</sup> However, as we will show in Chapter 2, when the exchange coupling is relatively weak, we have found that the influence of  $J$  on EPR transitions is non-trivial; therefore, the interactions between spins can be deduced from EPR experiments.

### 1.3.2 Quantum Tunneling of Magnetization

For the magnetic moment to reverse in a SMM, the spin can either acquire enough energy to jump over the barrier shown by Figure 1-2, or it can circumvent the barrier by quantum tunneling. Such tunneling is called quantum tunneling of magnetization (QTM) and was first observed in  $\text{Mn}_{12}\text{Ac}$ .<sup>5</sup> QTM in SMMs has elicited great interest since it is related to superpositions of quantum states, which is one of the key ingredients for quantum computations.<sup>2</sup> Figure 1-7 shows the scheme of QTM for an  $S = 6$  SMM. In general, QTM in SMMs can be understood with the following GS Hamiltonian:

$$\hat{H} = D\hat{S}_z^2 + \mu_B g_z B \hat{S}_z + \hat{H}' \quad (1-10)$$

where  $\hat{H}'$  is the portion of the zero-field Hamiltonian which does not commute with  $\hat{S}_z$ . The exact expression  $\hat{H}'$  should be determined by the symmetry of a molecule. For the reason of simplicity, we assume that  $\hat{H}'$  can be treated as a perturbation ( $\hat{H}' \ll D\hat{S}_z^2$ ) and the external field is applied parallel to the molecular easy-axis ( $z$ -axis). At this stage, we assume that the external field is applied along the  $z$ -axis (the transverse field equals to zero). The effects of the transverse fields will be discussed later.

QTM in SMMs occurs only between the degenerate states on the two sides of the potential barrier. At zero field, the energies of the 0<sup>th</sup>-order eigenvectors with opposite spin projections are

degenerate, where  $\varepsilon(m) = \varepsilon(-m)$  for all  $|m\rangle$  states. This corresponds to the energy levels crossing at zero field in Figure 1-7(a). Tunneling between  $|m\rangle$  and  $|-m\rangle$  states is allowed if there is mixing between these two states caused by  $\hat{H}'$ . In a QTM experiment, the tunneling between these two states is observed as a step in the magnetization versus field plot at zero field ( $k = 0$  step), as shown in the hysteresis loop in Figure 1-7(b). It is noteworthy that usually an ensemble of molecules, e.g., a single crystal, is measured in experiments, where only the magnetic moments of a portion of the molecules will tunnel when the field is swept through a QTM resonance. The height of the QTM step is proportional to the probability of quantum tunneling, which will be discussed in the next section. When an external longitudinal field is applied, the states become non-degenerate; thus, QTM is switched off. However, at certain fields, the energies of  $|m\rangle$  and  $|m'\rangle$  states can become degenerate again and QTM between these two states is allowed. This corresponds to the level crossings at non-zero magnetic field as shown in Figure 1-7(a). If the axial anisotropy of a SMM is restricted to the 2<sup>nd</sup>-order axial term,  $D$ , these fields are given by the following equation:

$$B = \frac{D(m + m')}{\mu_B g_z} \quad (1-11)$$

Because the spin projection,  $m$ , can only take discrete integer or half integer values, the longitudinal fields corresponding to QTM steps must be multiples of  $D/\mu_B g_z$ ; therefore, discrete QTM steps are observed with evenly spaced steps in SMM experiments, as shown in Figure 1-7(b). In the presence of high-order anisotropies, such as  $B_4^0 \hat{O}_4^0$ , the magnetic relaxation barrier deviates from parabolicity, which causes non-even spacings between QTM steps.

Crucially speaking, the selection rules of spin tunneling in SMMs should be determined by  $\hat{H}'$  and, hence, the symmetry of the molecule. Depending on the symmetry of the molecule, not all of the level crossings correspond to non-zero tunneling steps. In order to have a better understanding about spin tunneling, one needs to look more closely at the energy level crossings in the Zeeman diagram. Figure 1-8(a) shows the two possible scenarios for the energies of the two crossing states close to a QTM resonance field. For the sake of simplicity, we treat the molecule as a two level system with the basis of the Hilbert space constituted by  $|+m\rangle$  and  $|-m\rangle$  states. The dash lines correspond to the energy levels of the unperturbed states ( $\hat{H}' = 0$ ) where the red dash line is the  $|+m\rangle$  state and the black dash line is the  $|-m\rangle$  state. When the two states are not connected by  $\hat{H}'$ , the two crossing states are not mixed and the eigenvectors of the molecule are exactly  $|+m\rangle$  and  $|-m\rangle$ , i.e., the spin is strictly located on one side of the relaxation barrier. Thus, QTM between these states is forbidden. For instance, supposing that the longitudinal field is initially at  $H_-$  and all molecules are polarized in the  $|+m\rangle$  state, when the longitudinal field is swept through the QTM resonance field,  $H_0$ , to  $H_+$ , all molecules will follow the red arrows in Figure 1-8(a) and remain in the  $|+m\rangle$  state. In such a scenario, no tunneling of magnetization will be observed at  $H_0$ .

When the two states are connected by  $\hat{H}'$ , i.e.  $\langle m | \hat{H}' | m' \rangle \neq 0$  (and/or higher order perturbation results are non-zero), quantum tunneling between these two states is allowed. The energy levels of these two states are shown as the thick solid curves in Figure 1-8(a). As shown in the figure, the two states do not cross at the resonance field  $H_0$ . Instead, the energy levels exhibits an avoided crossing, with one level has an energy minimum and the other has a maximum. The minimum energy difference between these two levels is called the tunnel

splitting, as shown in the figure. The state with lower (higher) energy is labeled as  $|\Phi_g\rangle$  ( $|\Phi_e\rangle$ ), as shown in Figure 1-8(a). In this situation, the eigenvectors of these states are linear superpositions of  $|+m\rangle$  and  $| -m\rangle$ . Figure 1-8(b) shows the projections of  $|\Phi_g\rangle$  onto the basis eigenvectors where  $|C(m)|^2 = |\langle m|\Phi_g\rangle|^2$ . When the longitudinal field is at  $H_0$  ( $H_+$ ),  $|\Phi_g\rangle \approx |+m\rangle$  ( $| -m\rangle$ ). At these fields, the spin is well localized on one side of the relaxation barrier, either in the  $|+m\rangle$  or  $| -m\rangle$  state, where no QTM occurs. However, at the resonance field,  $H_0$ , the spin is strongly delocalized with equal probabilities on both sides of the relaxation barrier, which leads to tunneling of the magnetization. In this situation, supposing that initially all the molecules are in the  $|+m\rangle$  state and the field is swept from  $H_0$  to  $H_+$ , a portion of the molecules will tunnel through the barrier at  $H_0$  and relax to the  $| -m\rangle$  state, while the rest of the molecules remain in the  $|+m\rangle$  state.

The QTM rate between two states,  $|m\rangle$  and  $|m'\rangle$ , which corresponds to the height of the QTM step, is directly related to the tunnel splitting  $\Delta_{m,m'}$ .<sup>39,40</sup> Generally speaking, a non-zero QTM step must correspond to delocalization of spins; hence, a non-zero tunnel splitting. Experimentally, QTM has been used as a technique to measure small tunnel splittings.<sup>41</sup> However, the probability for spin tunnelings at a QTM resonance is complicated by many factors. The simplest theorem for estimating tunneling probabilities is the Landau-Zener-Stuckelberg formula<sup>42-44</sup>, which treats molecules as non-interacting spins. According to this theorem, the tunneling probability at very fast sweeping rates is given by<sup>45</sup>:

$$P = 1 - \exp\left[-\frac{\pi\Delta_{m,m'}^2}{2\hbar\mu_B |m - m'| dH_L/dt}\right] \quad (1-12)$$

where  $dH_I/dt$  is the longitudinal field sweeping rate. The dependence of the field sweeping rate can be understood intuitively. If  $dH_I/dt \rightarrow \infty$ , the spins would not be able to tunnel at  $H_0$  since the tunnel frequency, which is proportional to  $\Delta_{m,m'}$ , is finite. In this case,  $P = 0$ , as predicted by Equation 1-12. On the other hand, if  $dH_I/dt \rightarrow 0$ , which corresponds to the adiabatic limit, the magnetic moments of all the molecules will tunnel. This corresponds to  $P = 1$ , which is also consistent with Equation 1-12. However, between this two limits, the Landau-Zener-Stuckelberg formula is valid only in the very fast sweeping rate regime. In most experiments, application of Equation 1-12 is somewhat naive due to limitations of field sweeping rates. For slower sweeping rates, the effects of both nuclear spins<sup>46-48</sup> and dipolar interactions between molecules<sup>40, 46, 48, 49</sup> become significant; thus, the Landau-Zener-Stuckelberg formula, which is valid for an isolated spin, fails to explain experimental results. In addition, defects within a crystal can lead to a distribution of tunnel splittings, with the experimental results giving an average of these splittings.<sup>50, 51</sup> So far, there is no generally accepted formula for tunneling probabilities in QTM experiments.

Finally, we discuss the influence of transverse fields on QTM. Besides the zero-field transverse anisotropy  $\hat{H}'$ , the presence of an external transverse field  $H_T$  (perpendicular to the  $z$ -axis) also causes state mixing and contributes to tunnel splittings. For instance, application of a transverse field parallel to  $x$ -axis introduces a new term,  $H_x \hat{S}_x = H_x (\hat{S}_+ + \hat{S}_-)/2$ , which does not commute with the axial part of the Hamiltonian. The presence of a transverse field introduces the first order raising and lowering operators which can connect any two states with arbitrary  $\Delta m$  through first- or high-order perturbations. Therefore, in principle, the application of a transverse field should unfreeze all tunnel splittings regardless of the symmetry of a molecule.

A purely quantum-mechanical phenomenon observed in QTM measurements is the Berry Phase Interference (BPI) patterns observed upon applications of transverse fields. As we discussed previously, the presence of a transverse field should increase tunneling. However, it has been predicted that the tunnel splittings may not vary monotonically with increasing transverse fields, especially when applied along the hard axis of the molecule. In this case, the tunnel splitting will vanish at certain magnitudes of the transverse field.<sup>52</sup> This phenomenon can be understood as an analogy of the Aharonov-Bohm effect in spin space, as shown in Figure 1-9. In the case of 2<sup>nd</sup>-order anisotropy, i.e., Equation 1-3, there are two different spin tunneling paths with the same least action, which correspond to two classical paths between two states on the Bloch sphere. These two paths should wind around the hard axis in opposite directions, as illustrated by the thick red lines in Figure 1-9. These two paths can interference, where the destructive interference between the two paths leads to a vanishing tunnel splitting.<sup>53, 54</sup> The difference in the phase between these two tunneling paths is related to the solid angle enclosed by the two paths, which is labeled  $\Omega$  in the figure. Furthermore, for the ground state tunneling between  $|m = +S\rangle$  and  $|m = -S\rangle$ , it has been shown that when a magnetic field is applied along the hard axis, the topologic phase between these two paths varies from  $2\pi S$  to 0, where the tunnel splitting vanishes when the phase difference is an odd multiple of  $\pi$ .<sup>52, 55</sup> The points where tunnel splittings vanish are called diabolical points.<sup>56</sup> This oscillation of the tunnel splitting upon application of a transverse field is called BPI, as shown by the inset of Figure 1-9. In a QTM experiment, the BPI appears as the height of a QTM step oscillates upon application of a transverse field, which has been observed in QTM experiments on SMMs.<sup>39, 41</sup>

The symmetry of a BPI pattern is determined by the transverse anisotropy of a molecule, consequently the molecular symmetry. Therefore, BPI provides an extremely sensitive technique

for probing the symmetry of a SMM. In this dissertation, we will discuss BPI patterns in two SMMs with different symmetries in Chapters 3 and 4. Both theoretical and experimental studies have been performed in order to understand the influences of molecular symmetry on QTM.

### 1.4 Single-Chain Magnets

Recently, a new type of one-dimensional molecule-based magnet has been synthesized which exhibits slow relaxation of magnetization at low temperatures.<sup>57-63</sup> This type of compound is called a single-chain magnet (SCM), which is named by analogy to SMM. SCMs are one-dimensional isolated chains which are composed of anisotropic spin units repeatedly connected in series. Even though SCMs do not undergo long-range order at finite temperatures, the combination of the large anisotropy of the spin units and strong interaction between these units within a single chain causes an energy barrier for the relaxation of a chain's magnetic moment; therefore, the relaxation time of SCMs at low temperatures are so long that one can treat them as permanent magnets. Compared with SMMs, the obstacles to increasing the relaxation barriers in SCMs seem to be less severe.<sup>58, 64</sup> Since the first discovery of SCMs in 2001, they have attracted much interest due to their potential application as high density information storage materials.

Although the terminology, SCM, is analogous to SMM, the relaxation mechanisms in these two types of magnets are somewhat different. A SCM can be describe with the following Hamiltonian

$$\hat{H} = D \sum \hat{S}_{iz}^2 + J \sum \hat{S}_i \cdot \hat{S}_{i+1} \quad (1-13)$$

where  $\hat{S}_i$  is the spin operator of the  $i^{\text{th}}$  unit.  $D$  is the anisotropy of a single spin unit and  $J$  is the Heisenberg interaction between spin units.

The spin relaxation mechanism in SCMs was first predicted by Glauber based on an Ising-type chain in contact with a thermal bath.<sup>65</sup> While the relaxation barrier in a SMM corresponds to

the energy required to flip the entire magnetic moment of the molecule simultaneously, the relaxation barrier in SCMs corresponds to the energy to flip one spin unit within the chain. Glauber's theory predicts an exponential decay of the magnetization with a relaxation time of

$$\tau = \frac{\tau_i}{1 - \tanh(\Delta_\xi/k_B T)} \quad (1-14)$$

where  $\Delta_\xi$  is the correlation energy for creating a domain wall in the chain.  $\tau_i$  is the characteristic relaxation time for flipping an isolated spin unit and is given by

$$\tau_i = \tau_0 \exp(\Delta_A/k_B T) \quad (1-15)$$

where  $\tau_0$  is temperature independent and  $\Delta_A$  is the anisotropy barrier of each spin unit. Therefore, at low temperatures where  $\Delta_\xi \gg k_B T$ , the relaxation time can be written as

$$\tau = \frac{\tau_0}{2} \exp[(\Delta_A + 2\Delta_\xi)/k_B T] \quad (1-16)$$

As can be seen, the relaxation dynamics follows the Arrhenius law and the relaxation barrier is

$$\Delta = \Delta_A + 2\Delta_\xi \quad (1-17)$$

The activation energy for spin reversal requires creation of two domain walls, which separates a domain structures with different spin orientations. In the situation where the spin units in a chain possess easy-axis type anisotropy as described by Equation 1-3,  $\Delta_A = |D|S^2$ . The magnitude of the correlation energy for chains is  $\Delta_\xi = 2|J|S^2$  in the Ising limit ( $|D/J| > 2/3$ ), while  $\Delta_\xi = S^2\sqrt{2JD}$  in the Heisenberg limit ( $|D| \ll |J|$ ).<sup>66</sup> However, between these two limits, the correlation energy is a complex function of S, D and J, and the theorem for  $\Delta_\xi$  is still under investigation.

Equation 1-17 corresponds to the energy required for the nucleation of reversed spins, i.e., the creation of a domain structure, in an infinite chain. In SCMs, once the domain structure is

created, the domain walls can propagate in the chain without causing additional energy, as shown in Figure 1-10. We illustrate this process with a SCM in the Ising limit, where the domain structures are separated by narrow domain walls, i.e., the width of the domain wall is a single spin unit. The local field introduced by the interactions for the spins in inside a domain structure (as indicated by the blue box in Figure 1-10(a)) is equal to  $2JS^2$ , which is due to the fact that the two nearest neighbors of this spin are parallel to each other (Figure 1-10(a)). However, this local field vanishes for the spins of the domain wall (the spins indicated by the red boxes in Figure 1-10) because the two nearest neighbors of these spins are aligned anti-parallel to each other; hence, the spins of the domain wall can flip with the characteristic time  $\tau_i$  defined by Equation 1-15. At low temperatures, the relaxation of the magnetic moments of SCMs is mainly due to the random walks of the domain walls, where each step of the propagation of the domain structures process has the characteristic time  $\tau_i$ .

The previous discussion is based on the assumption that the system is an ideal 1D chain, which means the length of a chain can be considered to be infinite. However, in a real system, due to the presence of small crystallographic defects, a SCM can only have a finite length,  $L$ . The effect of finite lengths can have a significant influence on the magnetic dynamics of a chain at low temperatures. The correlation length  $\zeta$ , which is defined as the characteristic length of the spatial decay of the two spin correlation, grows very fast as the temperature decreases. Below a certain temperature,  $T^*$ ,  $\zeta$  exceeds the average length of the chains,  $L$ . When  $T > T^*$ , the SCM behaves the same as an infinite chain and Equation 1-17 is valid. When  $T < T^*$ , the probabilities for flipping spins at the ends of a chain are much larger since these spins are only connected to one nearest neighbor.<sup>67</sup> The activation energy for reversing spins at the ends of a chain requires the creation of only one domain wall, and it is given by:

$$\Delta = \Delta_A + \Delta_\xi \quad (1-18)$$

The activation energy required by Equation 1-18 is smaller than that of Equation 1-17. Therefore, for a finite chain at very low temperatures, the nucleation of spin reversal always starts at the ends of a chain, where only one domain wall is needed for the domain structure. After that, the domain wall can propagate along the chain, which leads to the relaxation of magnetization of the chain. Therefore, small crystallographic defects lead to decreasing of the relaxation barrier in the SCMs at very low temperatures.<sup>63, 64, 68</sup>

It is generally believed that there are three criteria for building a SCM:

- (a) Ferro- or ferri-magnetic interactions within a chain,
- (b) The spin units in a chain should possess large easy-axis type anisotropy,
- (c) Inter-chain interactions should be small.

While the first and the third criteria for building a SCM are absolutely required by definition, the second criterion seems to be arguable. Kajiwara and his collaborators have shown that a SCM can be built by a twisted alignment of easy-plane type ions.<sup>61</sup> In Chapter 5, we will discuss a Re<sup>IV</sup> based SCM which is formed with positive  $D$  anisotropy. EPR measurements on the building blocks of this SCM indicate that the Re<sup>IV</sup> ions possess a strong biaxial anisotropy with  $D > 0$ , as well as a significant transverse anisotropy. We found that quantum fluctuations in this SCM are suppressed as the length of the chain increases, while the transverse anisotropy of the Re<sup>IV</sup> ions gives rise to an anisotropy barrier and leads to magnetic bistability. The results demonstrate for the first time that slow relaxation of magnetization can be achieved through anisotropy barriers created by transverse anisotropy, which suggests a new strategy in designing SCMs.

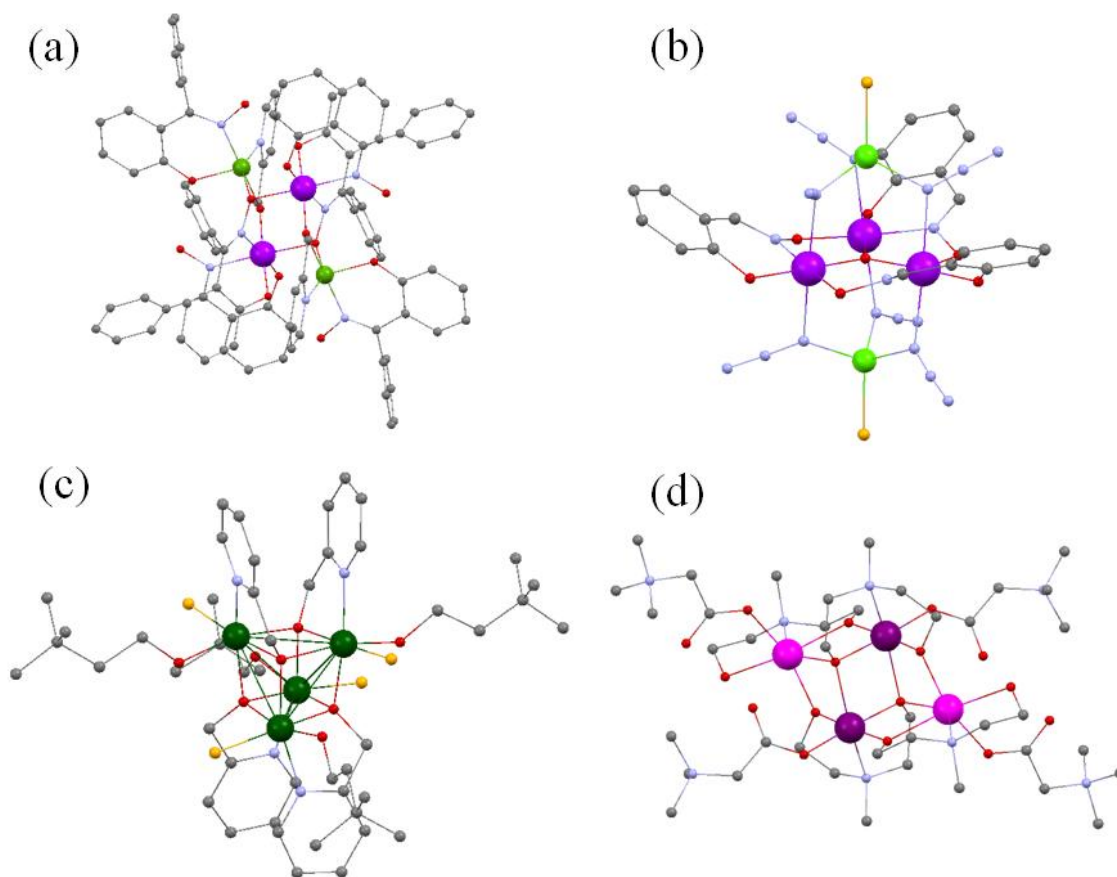


Figure 1-1. The molecular structures of several SMMs studied in this dissertation. The structures will be discussed in more detail in Chapters 2 (a), 3 ((b) and (c)) and 4 (d). Color code: Mn<sup>III</sup> = purple, Mn<sup>II</sup> = magenta, Ni = olive, Zn = green, Cl = dark gold, O = red, N = blue and C = black. H-atoms have been omitted for clarity.

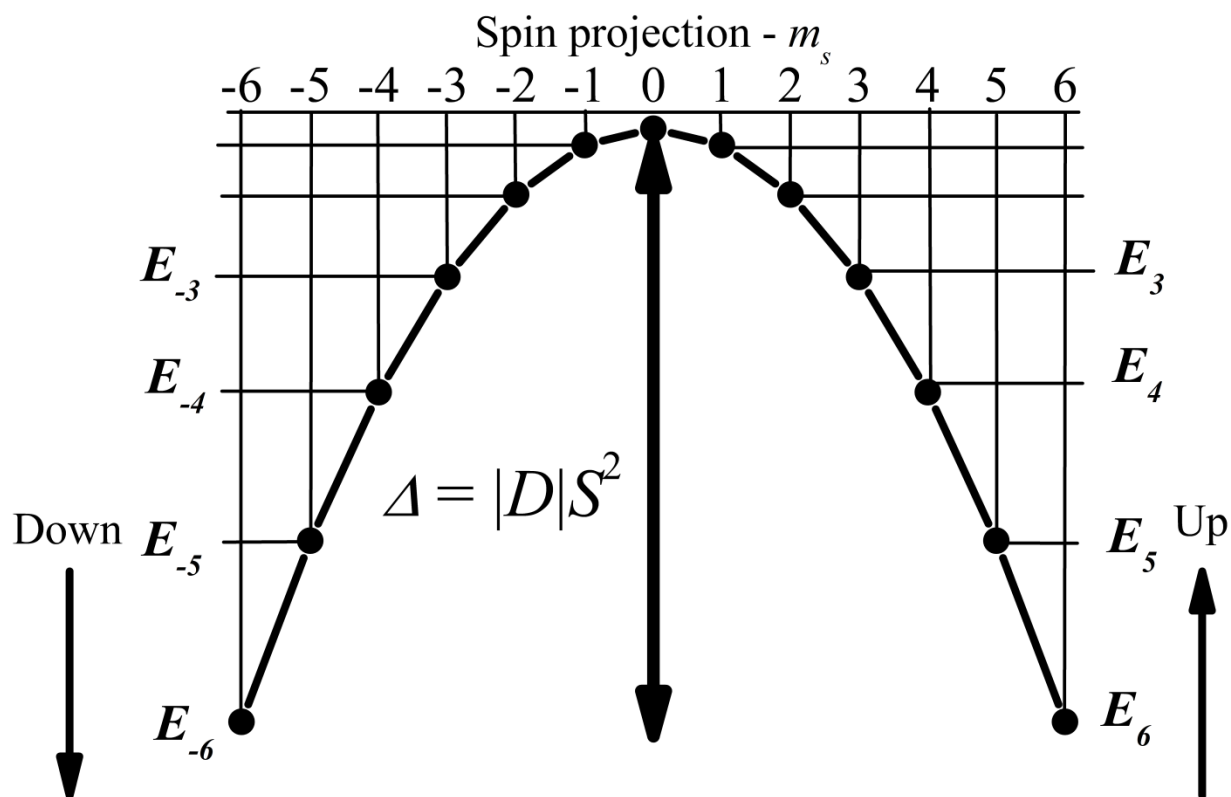


Figure 1-2. Schematic representation for the energy levels of an  $S = 6$  molecule with easy-axis type anisotropy ( $D < 0$ ). The “spin up” and “spin down” states are separated by the energy barrier  $\Delta$ , which leads to magnetic bistability at low temperatures.

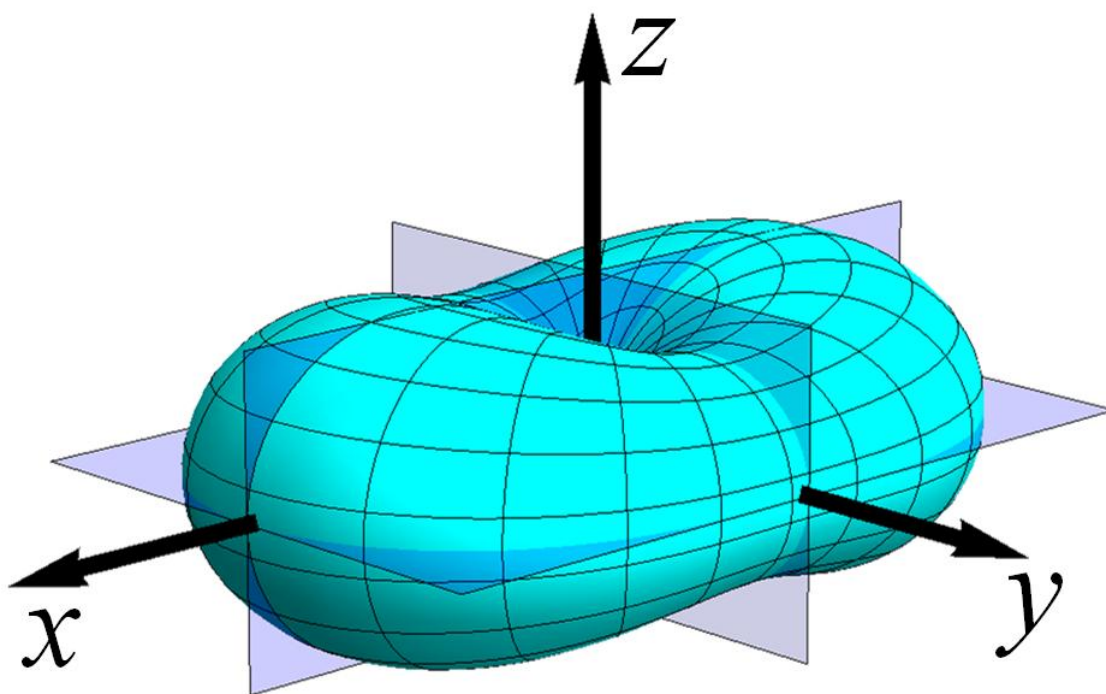


Figure 1-3. Potential energy surface corresponding to the 2<sup>nd</sup>-order anisotropy. The surface is generated employing Equation 1-3 with  $|E/D| = 1/5$  and  $D < 0$ . The radial distance to the surface represents the energy of a spin as a function of its orientation.

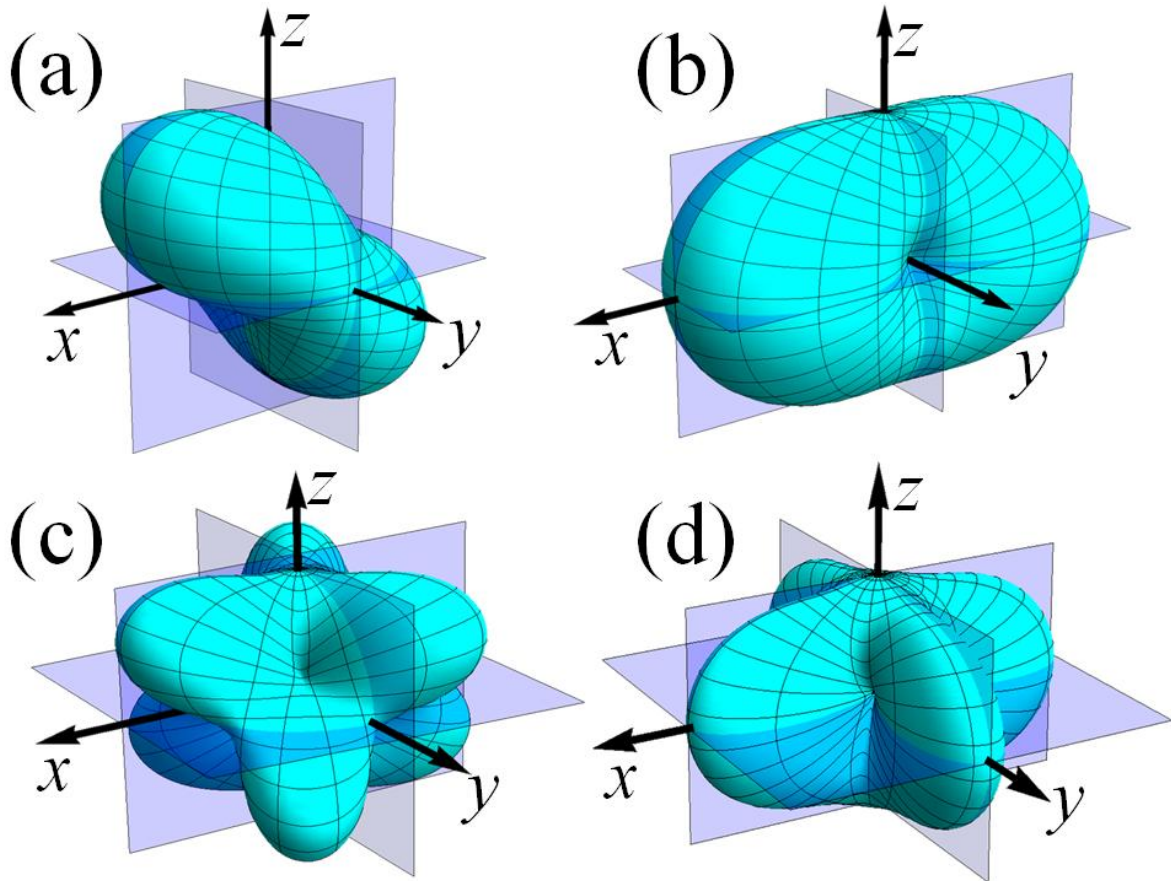


Figure 1-4. Potential energy surfaces corresponding to the fourth order Stevens operators.  $\hat{O}_4^1$  (a),  $\hat{O}_4^2$  (b)  $\hat{O}_4^3$  (c) and  $\hat{O}_4^4$  (d). As can be seen, the  $q$ -even operators include the  $xy$ -plane as an extra symmetry operation while the  $q$ -odd operators include an improper rotation.

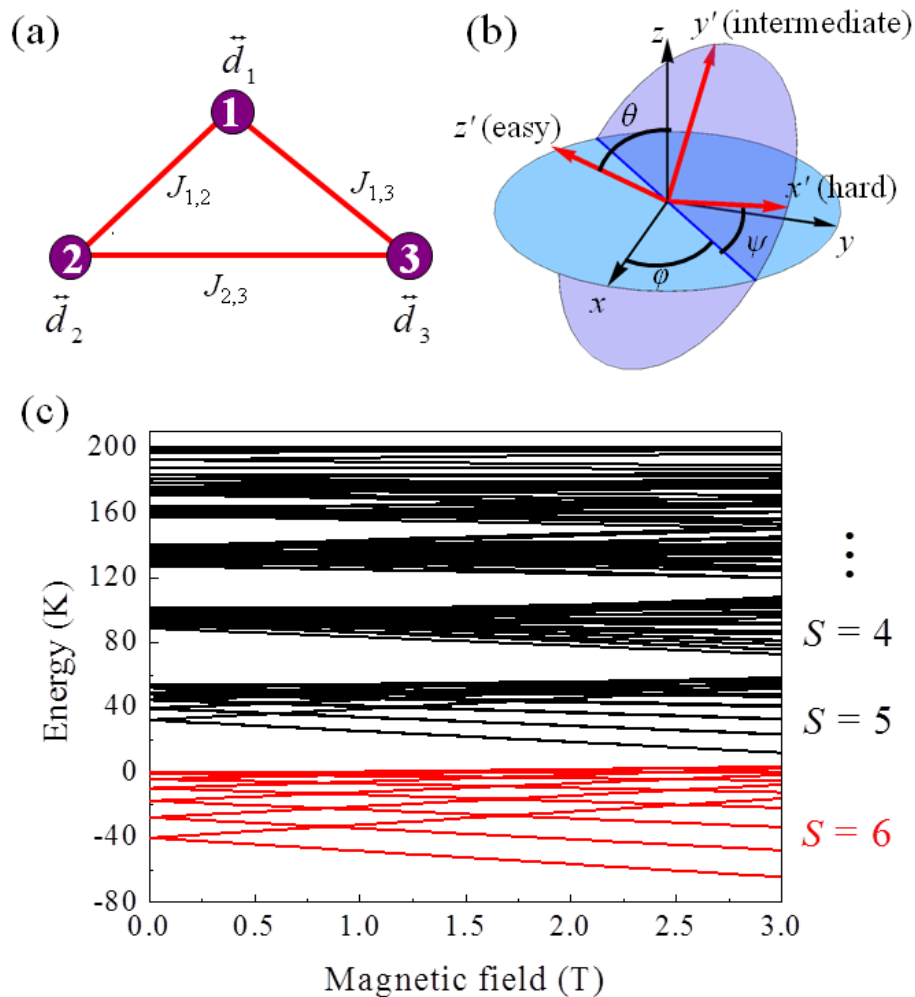


Figure 1-5. Schematic sketches demonstrating the concept of the MS Hamiltonian for a trinuclear molecule. (a) The molecule is treated as a cluster of anisotropic spins coupled via intra-molecular interactions. (b) The transformation from the local coordinate frame of a single spin ( $x'$ ,  $y'$  and  $z'$ ) to the molecular coordinate frame ( $x$ ,  $y$  and  $z$ ). (c) Zeeman diagram for the MS Hamiltonian. The ground spin multiplet ( $S=6$ ) is colored in red and the excited spin multiplets are colored in black.

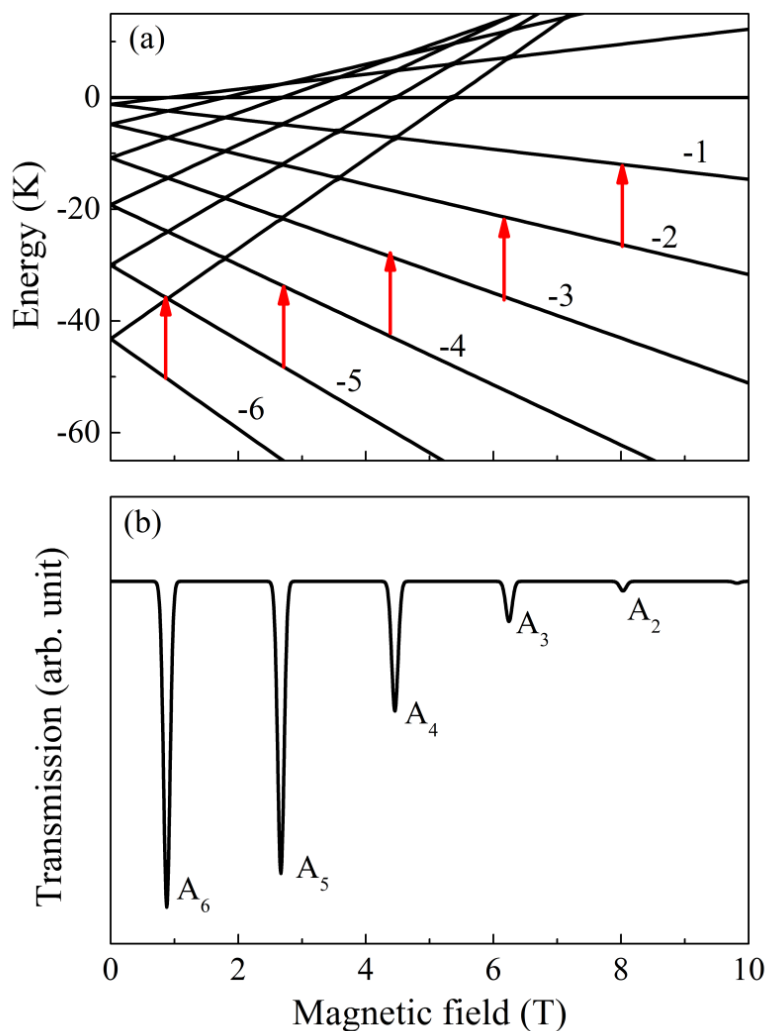


Figure 1-6. Schematic plots illustrating the theory of EPR measurements. (a) Zeeman diagram for an  $S = 6$  and  $D = -1.2$  K SMM with the field applied parallel to the molecular  $z$ -axis. The spin projections ( $m$ ) for each state are labeled in the figure. The red arrows indicates the EPR transitions with  $f = 300$  GHz. (b) Simulated EPR spectrum at  $f = 300$  GHz and  $T = 15$  K. The peaks are labeled according to  $m$ .

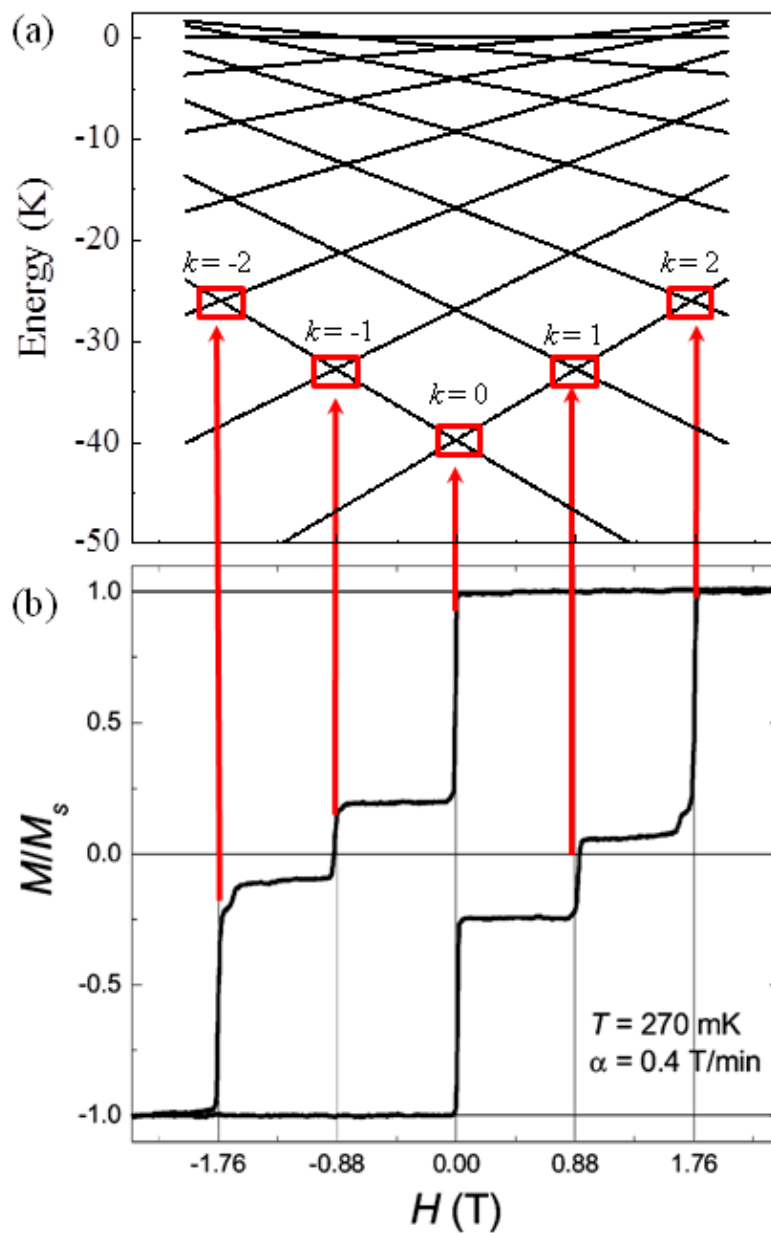


Figure 1-7. Quantum tunnel of magnetization in a  $S = 6$  SMM. (a) Zeeman diagram for an  $S = 6$  SMM. (b) Magnetization hysteresis loop for a single crystal of  $[\text{NEt}_4]_3[\text{Mn}_3\text{Zn}_2(\text{salox})_3\text{O}(\text{N}_3)_6\text{Cl}_2]$ . Detailed descriptions of this SMM are included in Chapter 3.

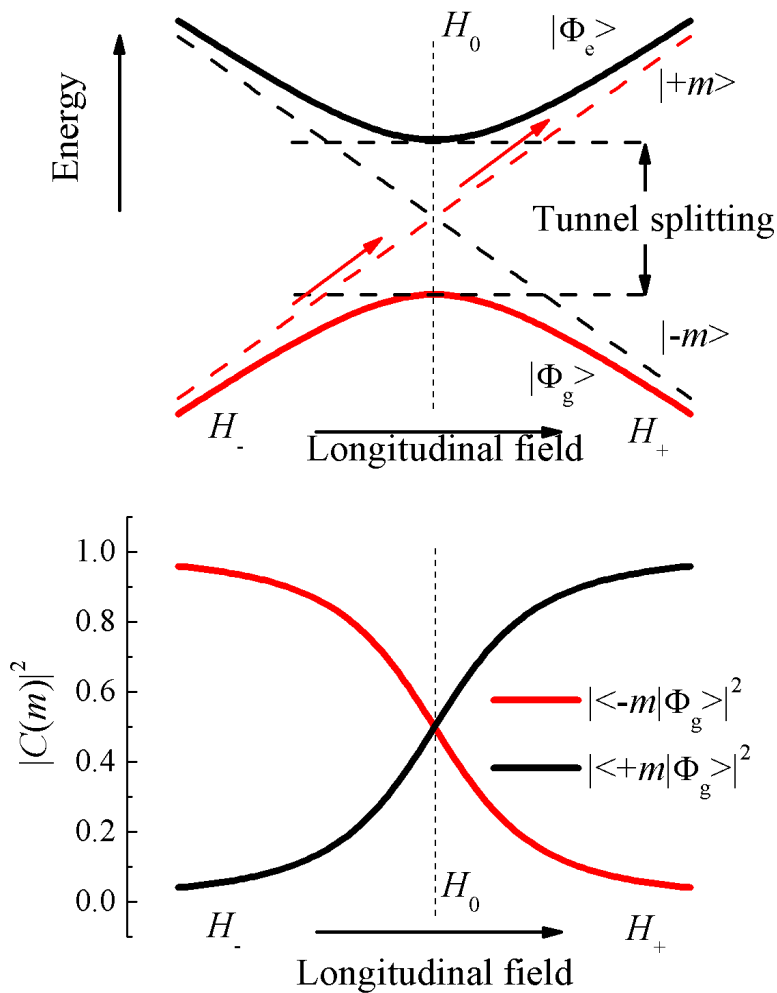


Figure 1-8. The tunnel splitting associated with QTM. (a) Energy levels of two crossing states close to a QTM resonance field. The solid black lines show the energy levels with avoid crossing. The tunnel splitting is non-zero and QTM between these two states is allowed. The dashed red lines correspond to the energy level when tunneling is forbidden. (b) Spin projections of the ground state onto the basis functions.  $|\Phi_g\rangle$  has equal projections onto  $|+m\rangle$  and  $|-m\rangle$  state at the resonance field, which is indicative of strong delocalizations of a spin as  $H_0$ .

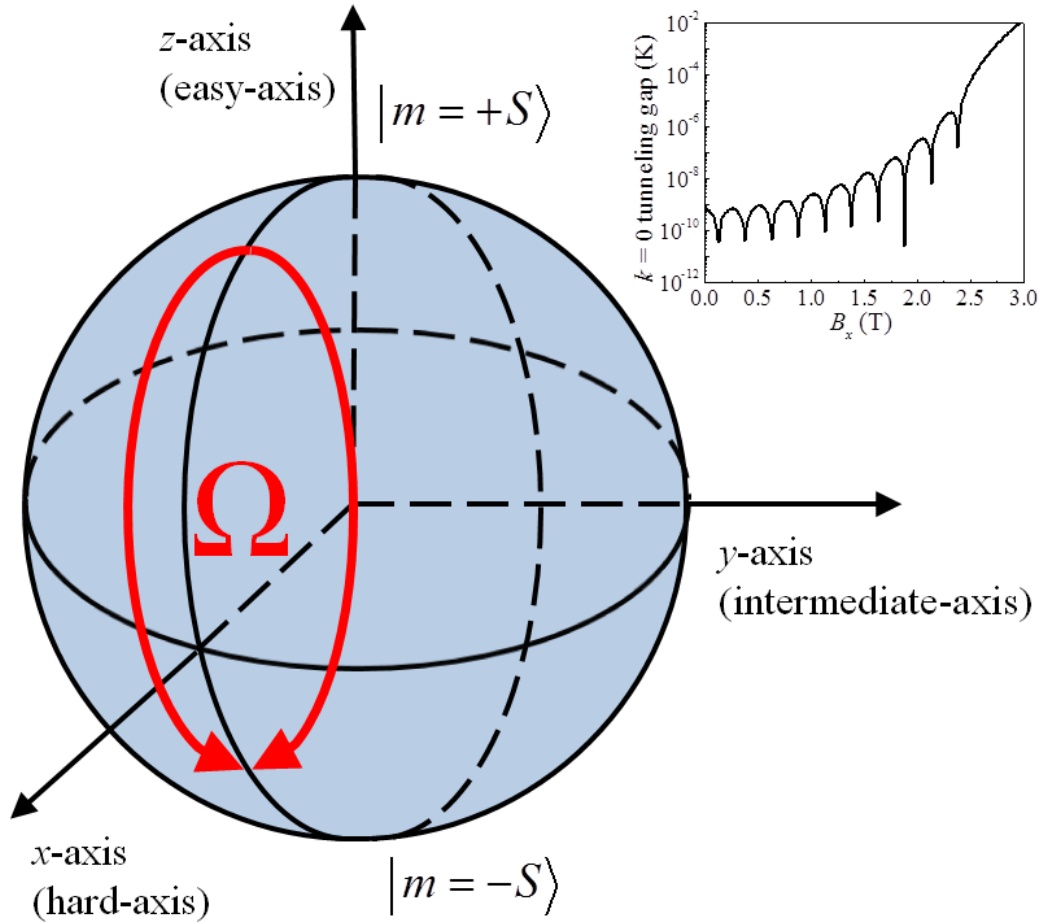


Figure 1-9. A schematic sketch of various tunneling paths on a Bloch sphere. The red thick arrows represent two possible tunneling paths from  $|m = +S\rangle$  to  $|m = +S\rangle$ . The solid angle enclosed by these two paths is  $\Omega$ , which is related to the phase difference between these two paths. (inset) The ground  $k = 0$  tunnel splitting of a  $S = 10$  SMM as a function of the applied transverse field,  $H_x$ .

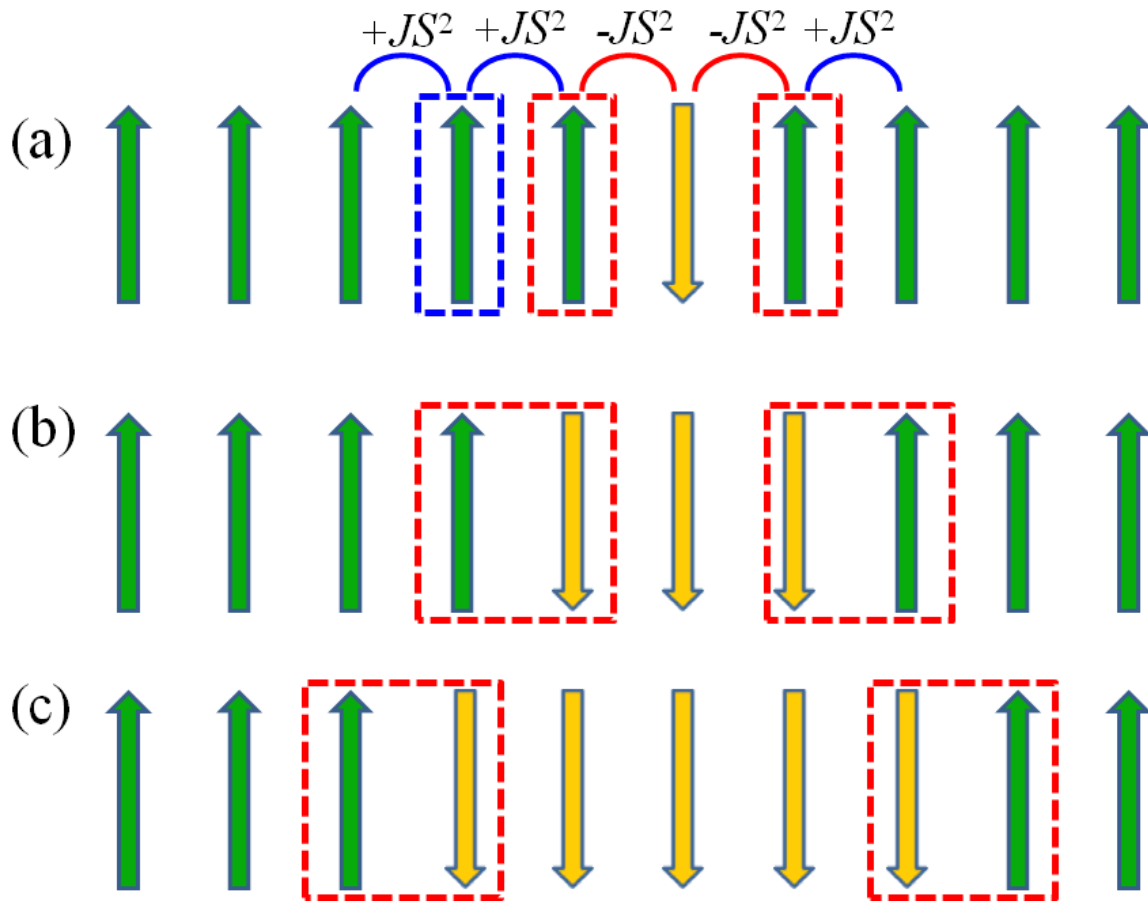


Figure 1-10. The process of the relaxation of magnetization in SCMs. (a): The nucleation of spins reversal in an infinite SCM. (b) and (c): The propagation of the domain walls in an infinite SCM. The spins on the domain walls are labeled by red boxes. Note that the local fields introduced by the nearest neighbor interactions vanish for these spins.

## CHAPTER 2 INTERPLAY BETWEEN ANISOTROPY AND EXCHANGE IN DINUCEAR MOLECULAR MAGNETS

Portions of the work presented in this chapter can be found in the following articles: Inglis, R.; Houton, E.; Liu, J.; Prescimone, A.; Cano, J.; Piligkos, S.; Hill, S.; Jones, L. F.; Brechin, E. K., Accidentally on purpose: construction of a ferromagnetic, oxime-based [MnIII<sub>2</sub>] dimer. Dalton Trans. 2011, 40 (39), 9999-10006. (reused with permission from The Royal Society of Chemistry)

### 2.1 Introduction

The magneto anisotropy barrier ( $\Delta$ ) plays a significant role for single-molecule magnets (SMMs) since this barrier determines the blocking temperature ( $T_B$ ). In the picture of the giant-spin approximation (GSA) model, the anisotropy barrier is mostly defined by the molecular axial anisotropy,  $D$ , and the ground spin state,  $S$ , where  $\Delta \approx |D|S^2$ . It is commonly believed that the magneto anisotropy of a molecule is mostly contributed by the anisotropies of the single ions within a molecule. Therefore, the axial anisotropy of a molecule is strongly related to the anisotropy parameters of single ions. On the other hand, the ground spin state of a molecule is mainly determined by the interactions between magnetic ions. Moreover, when the interactions within a SMM are weak, the internal degrees of freedom can have non-trivial influences on its magnetic relaxation barrier. Consequently, it is important to understand the interplay between anisotropy and exchange interactions, as well as any correlations with the molecular structures, in order to build SMMs with high  $T_B$ .

Unfortunately, deducing single-ion anisotropies and exchange interaction parameters for a large SMM cluster is not trivial. The interactions between spins within a molecule are usually determined by fitting the dc susceptibility measurements carried out over a wide temperature range.<sup>1</sup> However, given the complexity of a large molecule, it is almost impossible to deduce a

“unique” parameter set owing to the presence of multiple interaction parameters. This can be understood intuitively, where the procedure of data analysis involves deducing multiple parameters from one dc susceptibility versus temperature curve; hence, the Hamiltonian used in the analysis is likely to be over-parameterized. On the other hand, in magnetic measurements, the anisotropy of a molecule is usually deduced by fitting the magnetization measurements at various fields and temperatures conducted at the low temperature regime. This fit is strongly affected by the initial guess values used in the fitting program where, in most cases, both easy-axis ( $D < 0$ ) and easy-plane ( $D > 0$ ) type anisotropies can be obtained by fitting the same group of data, depending on the initial guess values. This dependence will be discussed in more detail in the data analysis for complex **1** in this chapter. Even though low temperature spectroscopic measurements such as electron paramagnetic resonance (EPR) can give a clear determination of the anisotropy of a molecule, it is still too ambitious to deduce a unique set of parameters for the exchange interactions of a large complicated molecule. Therefore, in order to understand the SMM behavior at the microscopic level, it is advantageous to study simple, low-nuclearity molecules. Studying such systems provides information about magneto-structural correlations, while the molecules may also be used as building blocks for larger clusters.

The simplest (and still extremely useful) platform for one to study the interplay between anisotropy and exchange interactions is dinuclear molecules composed of two identical magnetic ions. Especially when the molecule possesses inversion symmetry, the interaction parameters reduce to one exchange coupling tensor,  $\vec{J}$ , which can be simplified to a Heisenberg interaction,  $J$ , in most compounds. In these molecules, the single-ion anisotropies and exchange interactions can be deduced unambiguously by combining magnetic measurements and low temperatures

EPR. The information learned from these dinuclear compounds is of great help in revealing the correspondence between bond structures and magnetic interactions.

Among transition metal ions,  $\text{Mn}^{\text{III}}$  has been used extensively in synthesizing SMMs due to its large spin ground state ( $s = 2$ ) and strong anisotropy caused by Jahn-Teller (JT) distortions. In this chapter, we present EPR studies on two dinuclear  $\text{Mn}^{\text{III}}$  molecular magnets,  $[\text{Mn}^{\text{III}}_2\text{Zn}^{\text{II}}_2(\text{Ph-sao})_2(\text{Ph-saoH})_4(\text{hmp})_2]$  (**1**)<sup>69</sup> and  $[\text{Mn}^{\text{III}}_2(\text{L2})_2(\text{py})_4]$  (**2**)<sup>70</sup> (where L2 is the trianion of 3-(3-oxo-3-phenylpropionyl)-5-methylsalicylic acid, and py is pyridine). Compound **1** has a magnetic core constituted by two ferromagnetically coupled  $\text{Mn}^{\text{III}}$  ions while the  $\text{Mn}^{\text{III}}$  ions in the core of compound **2** are antiferromagnetically coupled. These compounds have attracted our interests because a) they provide ideal platforms to study magneto-structural correlations and b) they are proposed as candidates for pressure studies. The molecular structure, e.g., the bond lengths and bond angles, can be varied upon applying pressures, which will lead to variations in the magnetic properties of the molecule. EPR experiments were conducted on both compounds to explore the magnetic interactions and anisotropies associated with them.

## 2.2 Ferromagnetically Coupled Dinuclear $[\text{Mn}^{\text{III}}]_2$ Molecule

### 2.2.1 Discussions of Magnetometry Results

Complex **1** crystallizes in the triclinic space group  $P-1$  and lies about an inversion centre. The structure of compound **1** is shown in Figure 2-1(a). The magnetic core of this molecule is shown in Figure 2-1(b). The molecule contains a butterfly-like core of four metal ions with two  $\text{Mn}^{\text{III}}$  ions at the body position and two  $\text{Zn}^{\text{II}}$  ions at the wing-tip positions. The  $\text{Mn}^{\text{III}}$  are six-coordinate in a Jahn-Teller elongated octahedral geometry. The  $\text{Zn}^{\text{II}}$  ions are diamagnetic which block any interaction through them. As a result, the two  $\text{Mn}^{\text{III}}$  are only coupled via the super-exchange interactions through the two identical -N-O- bridges.

Complex **1** was synthesized to study the magneto-structural relationship in oxime-bridged Mn<sup>III</sup> cluster compounds. It is also a candidate for studying the influences of large pressure on the magnetic properties of molecules. The bonds between the two Mn<sup>III</sup> ions are likely to be distorted in the presence of large pressure; thus, the interactions within the molecule should vary upon applying pressure. Magnetic measurements for complex **1** were carried out in Dr. Euan Brechin's group in the University of Edinburgh, Scotland. High-frequency EPR measurements were carried out in the NHMFL and form the subject of this section.

Complex **1** possesses inversion symmetry, which guarantees the anisotropy tensors of the two Mn<sup>III</sup> ions to be identical and parallel to each other. In the data analysis, we simplified the system by only considering the Heisenberg interaction between the two Mn<sup>III</sup> ions. The molecule is modeled by the following multi-spin (MS) Hamiltonian:

$$\hat{H} = \sum_{1,2} [d\hat{s}_{iz}^2 + e(\hat{s}_{ix}^2 - \hat{s}_{iy}^2)] + J\hat{s}_1 \cdot \hat{s}_2 \quad (2-1)$$

where  $\hat{s}_i$  is the spin operator for the  $i^{\text{th}}$  ion;  $d$  and  $e$  are the 2<sup>nd</sup>-order anisotropy parameters of the single Mn<sup>III</sup> ions; and  $J$  is the Heisenberg interaction between them.

At this point, we would like to briefly review some discussions about the magnetic data made by Dr. Brechin's group. These discussions demonstrate several important issues involved in interpreting magnetic measurement results; furthermore, these discussions emphasize the significance of EPR. In the magnetometry data analysis for most SMMs, the exchange interactions and the anisotropy parameters of a molecule are obtained by fitting different measurement results to different models. The exchange interactions are usually obtained via fitting the dc susceptibility versus temperature data ( $\chi_m T$  vs.  $T$ ) to an isotropic MS Hamiltonian, which treats the molecule as a cluster of isotropic ions coupled through an isotropic exchange interaction, i.e., it ignores the zero-field splittings (ZFS) of individual ions. This measurement is

usually carried out at a wide temperature range (from the helium temperature to room temperature), where the main features of the obtained curve are dominated by the energy separations between different spin multiplets. On the other hand, the anisotropy parameters are usually deduced by fitting the low temperature magnetization measurements at various fields and temperatures, namely reduced magnetization (RM), to a GSA Hamiltonian, which assume that only the ground spin multiplet is populated. In the data analysis for complex **1**, Dr. Brechin's group tried to fit the magnetic measurements to Equation 2-1, which allows both the anisotropy parameters,  $d$  and  $e$ , as well as the exchange interaction,  $J$ , to vary simultaneously. The details of these discussions can be found in Ref. [31]. In their analysis, they showed that the  $\chi_m T$  vs.  $T$  data provides a tight constraint on the exchange interaction, where the best-fit results always converge at approximately the same  $J$  value with  $J = -6.4$  K, regardless of the initial guess values used in the fit. By contrast, the axial anisotropy values are not well constrained by the  $\chi_m T$  vs.  $T$  data, depending strongly on the initial guess values. Meanwhile, varying  $d$  has little influence on the obtained  $J$  value. This is a clear indication that  $\chi_m T$  vs.  $T$  data cannot be used as a reliable criterion in the determination of magnetic anisotropy. Therefore, in order to determine  $d$ , the Brechin group fit the low temperatures RM data to Equation 2-1, fixing  $J = -6.4$  K. The RM result provides a much tighter constraint on  $d$ , with the best-fit value of  $d = -4.65$  K. However, in their analysis, they clearly showed that the best-fit of  $d$  still relies on the initial guess used in the fit. In fact, it is possible to fit the RM data with an easy-plane type  $d$  ( $= +5.21$  K) if the initial guess value for  $d$  is chosen to be positive, though the quality of fit clearly favors an easy-axis type  $d$  ( $< 0$ ).

The preceding discussion indicates that the anisotropy parameters deduced from magnetic measurements are not always reliable, which also applies to the compound **2** discussed in the

second part of this chapter. Therefore, single-crystal EPR measurements were performed on complex **1**, primarily with a view to determining the magnetic anisotropy associated with its ground state. However, as shall be seen, it is also possible to estimate the exchange interaction strength within the molecule from EPR measurements. The capability of deducing the exchange interaction parameter from EPR is of great importance, as it paves the way for future studies regarding the influence of high pressures on the magnetic interactions in this molecular magnet.

### 2.2.1 EPR Spectroscopy

EPR Experiments were conducted in a spectrometer that enabled in-situ rotation of the sample about a fixed axis; details can be found elsewhere.<sup>71, 72</sup> Variable frequency (60 - 410 GHz) and variable temperature measurements were thus performed with the field aligned both in the hard-plane and at an orientation close to the easy axis.

Figure 2-2 shows representative spectra obtained at 171 GHz with the external field applied in the hard plane. The sharp transition seen at ~6 T at all temperatures is due to a paramagnetic impurity (with  $g = 2.00$ ) in the sample and is ignored in the ensuing data analysis. A cluster of transitions seen in the 12-13 T range increases in intensity with decreasing the temperature, indicating that it involves excitations from the ground state. Likewise, a broad, featureless dip centered at ~7.5 T (the red arrow in Figure 2-2) is also seen to strengthen with decreasing temperature. The observation of multiple excitations from the ground state can be attributed to weak disorder in the sample. Indeed, essentially identical behavior is seen in the hard-plane spectra of the  $\text{Mn}_{12}$ -acetate<sup>31, 73, 74</sup> and  $\text{Ni}_4$ <sup>75, 76</sup> SMMs. The cluster of fine structure peaks at the highest fields is likely caused by a discrete disorder associated with either the ligand or solvent molecules that gives rise to distinct species with slightly different transverse anisotropy parameters, hence the observation of several resolved peaks in the hard plane spectra (as denoted by the vertical arrows in Figure 2-2).<sup>31, 74</sup> The broad feature can be attributed to a

very slight tilting of the zero-field-splitting (ZFS) tensors associated with the different species such that the field is not perfectly aligned in the hard plane for all of the molecules (*vide infra*).<sup>31</sup>

Figure 2-3 shows several representative spectra collected with the field being close to the molecular easy-axis at 15 K. We note that the diminished sensitivity of the spectrometer at higher frequencies required data above 360 GHz to be recorded at 2 K, where only the A<sub>4</sub> transition (ground state transition) is observed. The spectra also reveal clear evidence for the same disorder, with the effect most pronounced for the ground state transition, as expected on the basis of *D*-strain.<sup>77, 78</sup>

Figure 2-4 shows the frequency dependence of EPR peak positions observed with the field applied (a) close to the molecular easy axis and (b) exactly in the hard plane; we include only peaks that can clearly be identified and assigned to known transitions. As can clearly be seen in (a), four branches of resonances are observed which are labeled A<sub>1</sub>, A<sub>2</sub>, A<sub>3</sub> and A<sub>4</sub>, where A<sub>*i*</sub> denotes the transition from  $m = -i$  to  $-(i - 1)$  states and  $m$  is the spin projection onto the easy-axis (A<sub>4</sub>' is the  $m = +4$  to  $+3$  transition and B<sub>4</sub> is a shoulder on A<sub>4</sub> attributed to disorder). The resonances in Figure 2-4(b) have been labeled according to the same scheme except that  $m$  now corresponds to the spin projection onto the high-field quantization axis, which necessarily corresponds to the applied field direction. The observation of four resonance branches with positive zero-field intercepts in Figure 2-4(a) confirms the  $S = 4$  ground state spin value, while the fact that the A<sub>4</sub> transition persists to the lowest temperatures suggests easy-axis anisotropy. It is noticeable in Figure 2-4(a) that the horizontal spacing between the four main branches is non-uniform. It is well documented that this is indicative of weak coupling, i.e.,  $J \sim |d|$ .<sup>35, 37</sup> In the strong coupling limit ( $|J| \gg |d|$ ), only 2<sup>nd</sup> order ZFS ( $D\hat{S}_z^2$ ) is expected within the  $S = 4$  ground state, which would result in equal spacing between the easy-axis peaks. In the GSS picture, this

uneven spacing is captured via  $B_4^0$  and higher order axial anisotropies, which is caused by spin mixing between different  $S$  multiplets in the weak coupling regime. Thus, the uneven spacing provides an additional handle on the exchange coupling parameter  $J$ .

The solid lines in Figure 2-4 represent the best simulations of the peak positions using Equation 2-1 with the following parameters:  $d = -5.52$  K,  $J = -6.71$  K and  $g = 2.00$ . Figure 2-4(a) required an  $18^\circ$  field misalignment due to the fact that one cannot guarantee exact coincidence with the easy axis when rotating about a single-axis. Furthermore, in order to obtain a good simulation for the hard plane data in Figure 2-4(b), a rhombic anisotropy term was included for each  $\text{Mn}^{\text{III}}$  ion with  $e = 0.26$  K; the data points represent the strongest central resonance within each cluster of peaks, with the error bars spanning the adjacent peaks/shoulders (see vertical arrows in Figure 2-2). It should be noted that the obtained  $e$  value represents a lower bound because the precise field orientation within the hard plane was not known. The broad feature around 7.5 T in Figure 2-2 is illustrated by the considering a small field misalignment as shown in Figure 2-4(b). When the applied field is in the molecular hard plane, the  $A_3$  resonance goes through a minimum ( $\sim 190$  GHz) and then tends to a sizable non-zero value as the field tends to zero; hence, this resonance should not be observed at 171 GHz, at which the spectra in Figure 2-2 were recorded. The thin curves in Figure 2-4(b) show that when the field is slightly out of the molecular hard plane, the minimum of the  $A_3$  resonance decreases below 171 GHz; thus, it is possible to explain this transition at 171 GHz by including a small field misalignment, which leads to the broad feature close to 7.5 T in Figure 2-2. The slope of the  $A_3$  resonance branch at 7.5T/171 GHz is extremely shallow, which is why the linewidth of the feature is so much broader than that of other EPR transitions. It should be clarified that this out-of-hard-plane feature is not simply an experimental error, as careful angle dependence studies were performed

to ensure that the applied field was within  $1^\circ$  of the molecular hard plane. The observation of  $A_3$  at 171 GHz requires a field misalignment for at least  $3^\circ$ . We attribute this to orientational disorder resulting in a fraction of molecules whose easy axes are slight tilted away from the others. As can be seen, the simulations provide a good overall agreement for all plotted EPR transitions observed in both orientations. We note the excellent agreement between these parameters and those obtained via analysis of magnetic data, thereby providing further confidence in the conclusions of this work.

We conclude the analysis for complex **1** by discussing the constraint of  $d$  and  $J$  based on EPR spectra. The ZFS associated with the easy axis ground state transition ( $A_4$ ),  $\Delta_0$ , is dominated by the single-ion anisotropy,  $d$ , while it is extremely insensitive to  $J$ , even in the weak coupling regime. With the aforementioned single-ion anisotropies ( $d = -5.52$  K and  $e = 0.26$  K),  $\Delta_0$  only changes by 0.7% (0.1 K) upon varying  $J$  from -1 K ( $\sim d/5$ ) to  $-\infty$ . Furthermore, if  $e = 0$ , as long as the interaction is ferromagnetic,  $\Delta_0$  is completely independent of  $J$ . This is essentially a classical result which indicates the fact that the in-phase precession of 2 identical spins about a fixed axis is insensitive to the interactions between them. A similar conclusion was obtained in other SMMs which can be generalized to any ferromagnetically coupled molecule with  $N$  identical spins.<sup>37</sup> Another semi-quantitative approach for understanding this result is based on considering the symmetry of the molecule. We first consider the scenario where  $e = 0$ ; in this case,  $m$  is a good quantum number. The molecule possesses inversion symmetry, which guarantees that parity is good quantum number for the system. The ground state,  $|S = 4, m = -4\rangle$ , and the first excited state,  $|S = 4, m = -3\rangle$ , are two symmetric states. Because  $|S = 4, m = -4\rangle$  is the only  $m = -4$  state, it cannot mix with any other states if  $e = 0$ . There are two  $m = -3$  states, namely  $|S = 4, m = -3\rangle$  and  $|S = 3, m = -3\rangle$ . However,  $|S = 3, m = -3\rangle$  state is an anti-symmetric state;

thus, there cannot be any mixing between the  $|S = 4, m = -3\rangle$  and  $|S = 3, m = -3\rangle$  states.

Therefore, the  $|S = 4, m = -4\rangle$  and  $|S = 4, m = -3\rangle$  cannot mix with any other states and the transition between these two state ( $A_4$ ) is independent of  $J$ . By contrast, the  $|S = 4, m = -2\rangle$  can mix with  $|S = 2, m = -2\rangle$ , which is a symmetric state. The mixing between these  $m = -2$  states is affected by  $J$ ; hence, the transition between the  $m = -3$  and  $m = -2$  states ( $A_3$ ) is  $J$ -dependent.

When  $e \neq 0$ ,  $m$  is no longer a good quantum number and the  $|S = 4, m = -4\rangle$  state can mix with  $m = -2$  states via the 2<sup>nd</sup>-order rhombic anisotropy. In this scenario, the ground state transition will be affected by  $J$  since the  $|S = 4, m = -4\rangle$  can mix with  $|S = 2, m = -2\rangle$  through  $|S = 4, m = -2\rangle$ . However, this mixing is a high-order perturbation because it involves both  $m$ -mixing introduced by  $e$  and  $S$ -mixing introduced by weak  $J$ . Therefore, the ground state transition shows very weak dependence on  $J$ , even in the extremely weak interaction regime.

According to the preceding discussions,  $d$  can be accurately determined by only considering the ground state transition. The spacing between the ground transition ( $A_4$ ) and the first excited transition ( $A_3$ ) provides a constraint on the exchange interaction  $J$ . In principle, the molecule can be characterized by these two transitions, which are the strongest transitions at low temperatures. This indicates that it is possible to study the influence of pressures on the magnetic properties of complex **1** by EPR, where the sensitivity of experiments is strongly decreased due to the limitations on the volume of the crystals that can be used in pressure studies.<sup>79</sup>

### 2.3 Antiferromagnetically Coupled Dinuclear $[\text{Mn}^{\text{III}}]_2$ Molecule

Complex **2** crystallizes in a triclinic space group  $P-1$  and lies about an inversion center. The structure of compound **2** is shown in Figure 2-5. **2** was originally proposed as a candidate for investigating the magnetic properties of molecular magnets under pressures. The  $\text{Mn}^{\text{III}}$  ions in the

molecule are six-coordinated in a JT elongated octahedral geometry with the JT axes defined by the Mn-N bonds, which is similar to complex **1**. However, the exchange paths in this compound are more complicated, since the shortest contacts connecting two Mn<sup>III</sup> ions are two -O-N-N-N-O- bonds. Nevertheless, the dc magnetic susceptibility measurement suggests a non-zero interaction between the Mn<sup>III</sup> ions within the molecule<sup>70</sup>, which is confirmed by EPR studies (*vide infra*).

The structure and magnetic studies of complex **2** was originally reported by Dr. Aromi's group in 2002.<sup>70</sup> However, its magnetic properties were not fully understood at the time since the anisotropies of the Mn<sup>III</sup> ions were unknown, in spite of the fact that a powder EPR study had been performed. A MS Hamiltonian including anisotropic exchange was proposed in Ref. [70] in order to interpret the magnetic measurements. However, the data analysis resulted in an unphysical, highly anisotropic interaction ( $J_z/J_{x,y} \approx 0.8$ ) which is unlikely to occur in Mn-based magnets.<sup>80</sup> To fully understand the magnetic properties of **2**, further single-crystal EPR measurements were performed to probe its magnetic parameters. Detailed analyses of the EPR spectra were performed, giving a comprehensive picture regarding the low temperature physics in weakly antiferromagnetically coupled Mn<sup>III</sup> based dinuclear molecules. The EPR experiments give an unambiguous determination of both the anisotropy and exchange parameters of **2**, which also explain the previous magnetic measurements.

### 2.3.1 EPR Spectroscopy

The previous EPR measurements were performed on powder samples of **2** by Dr. Krzystek at the NHMFL. However, the results were never understood. Therefore, we carried out EPR experiments on single crystals of **2**. In the mean time, we also redid some powder measurements and analyzed the old powder spectra collected by Dr. Krzystek. Single-crystal measurements

were performed in a 7 T superconducting magnet with temperature control achieved by a  $^4\text{He}$  flow cryostat. A Millimeter-Wave Network Analyzer served as a microwave source and detector, and a cavity perturbation technique was employed to measure a needle-shaped single crystal with approximate dimensions  $150 \times 150 \times 500 \mu\text{m}^3$ .<sup>71, 72</sup> Unfortunately, larger sample was unavailable due to difficulties in growing large single crystals. The volume of this crystal is of an order smaller comparing with most single-crystal samples used in our experiments. Powder EPR measurements were carried out in a transmission-type spectrometer based on a 15 T superconducting magnet, which differed from that described in<sup>81</sup> only by the use of a Virginia Diodes solid state source operating at  $13 \pm 1$  GHz, followed by a cascade of multipliers and amplifiers. The powder experiments were performed with both loose powders and finely ground powders restrained by *n*-eicosane.

We start by describing the experiments on a powdered sample of **2**; an example of EPR spectra is shown in Figure 2-6. The sample produced a very strong and well-defined EPR response over all the available frequency range. However, this rich spectrum was essentially uninterpretable. Qualitatively, it shows that the interactions between the  $\text{Mn}^{\text{III}}$  ions create new spin states that are unlike those of the individual  $\text{Mn}^{\text{III}}$  ions, as the spectrum does not resemble that of a spin  $S = 2$  system. At the same time, we did not succeed in interpreting the data in terms of a well-defined  $S$  state. We thus performed HF-EPR measurements on a single crystal. An example of a single-crystal spectrum is shown in the inset of Figure 2-6. Single axis rotation was carried out first to align the applied external field close to the molecular  $z$ -axis. Following that, extensive frequency and temperature dependence studies (380-510GHz, 2-20K) were performed at this fixed orientation. Figure 2-7(a) shows the peak positions of the observed EPR transitions in a crystal with the field applied close to the molecular  $z$ -axis at 2 K. Temperature-dependent

measurements (not shown) confirmed that the two transition branches observed at low field, which are denoted as  $\alpha_1$  and  $\alpha_2$  in Figure 2-6 and 2-7(a), originate from the ground spin state. As shown in Figure 2-6, due to the limitation that a large single crystal is not available for **2**, the signal-to-noise ratio in the single-crystal measurements is much lower than that of the powder experiments. However, as we will show, the single-crystal experiments still provide sufficient information to fully characterize complex **2**.

For an antiferromagnetically coupled dinuclear molecule, the ground state is expected to be a non-magnetic state if  $|J| \gg |d|$ . The fact that we observe well-defined EPR transitions at low temperatures indicates that the  $J$  is small and the system cannot be described by a GSA model. Therefore, we employed Equation 2-1 in analyzing our EPR results. In the data analysis, we reduced the number of unknown parameters by making the following two assumptions: a)  $g = 2.00$  and b)  $e = 0$ . The assumption of an isotropic Landé  $g$  factor,  $g = 2.00$ , is a reasonable approximation for most reported  $\text{Mn}^{\text{III}}$  ions in octahedral coordination.<sup>82</sup> The rhombic anisotropy for individual ions is ignored in our analysis due to the fact that, with the fields applied in the molecular  $xy$ -plane, the low temperature EPR transitions appear out of experimental field range (above 15 T). Fortunately, the experimental results indicate that such simplification is acceptable (see more details in powder data discussions). This is simplest Hamiltonian that one can adopt to describe complex **2**. However, the Hamiltonian can account for the two key experimental results: (a) the EPR spectra (Figure 2-6 to 2-8) and (b) the reduced magnetization data (Figure 2-9).

Before presenting the detailed analysis of the spectra, we should discuss the EPR selection rules that can be applied to **2**. Due to the fact that **2** does not have a well defined spin state, one can not apply the normal EPR selection rules,  $\Delta S = 0$  and  $\Delta m = \pm 1$  as we mentioned in Chapter 1. However, since only the axial anisotropy is included in the Hamiltonian,  $m$  remains a good

quantum number when the field is applied along the molecular z-axis. Thus, the selection rule  $\Delta m = \pm 1$  still holds. Furthermore, due to the inversion symmetry of the molecule, all of the eigenvectors must have definite parity upon exchanging two spins (symmetric or anti-symmetric). The probability of EPR transitions, which are magnetic dipole transitions, is non-zero only if the transition occurs between states with the same parity. Therefore, we conclude that the EPR selection rules of **1** are: (a)  $\Delta m = \pm 1$ ; and (b) the parity of the initial and final states is conserved.

Figure 2-7(b) shows the low energy part of the simulated Zeeman diagram of **2** with the applied field along the molecular z-axis. This simulation was performed employing Equation 2-1 with the following parameters:  $d = -5.76$  K,  $e = 0$  and  $J = +2.45$  K. These parameters give good agreements for both single-crystal and powder EPR experimental results (*vide infra*). In order to understand the origins of the observed EPR transitions, one needs to consider the symmetry of the eigenvectors corresponding to the energy levels in Figure 2-7(b). In order to do this, we treat the diagonal part of the zero-field Hamiltonian,  $d\hat{s}_{z1}^2 + d\hat{s}_{z2}^2 + J\hat{s}_{z1}\hat{s}_{z2}$ , as the unperturbed

Hamiltonian  $\hat{H}_0$  and the off-diagonal part of the Heisenberg interaction,  $\frac{J}{2}(\hat{s}_1^+\hat{s}_2^- + \hat{s}_1^-\hat{s}_2^+)$ , as the perturbation  $\hat{H}'$ , where  $\hat{s}_i^\pm$  are the raising and lowering operators and  $\hat{H} = \hat{H}_0 + \hat{H}'$ . As we will show, this perturbation treatment gives a quantitative agreement with the experimental results. If  $J = 0$ , the molecule is composed of two non-interacting spins; hence, the eigenvectors of the molecule can be written as direct products of the uncoupled single  $\text{Mn}^{\text{III}}$  eigenvectors,  $|m_1\rangle$  and  $|m_2\rangle$  (abbreviated as  $|m_1, m_2\rangle$ ), where  $m_1$  and  $m_2$  represent the spin projection of the two  $\text{Mn}^{\text{III}}$  ions and  $m = m_1 + m_2$ . At zero field, the ground state of the molecule is quadruply degenerate, where these four states are:  $|+2, +2\rangle$ ,  $|+2, -2\rangle$ ,  $|-2, +2\rangle$  and  $|-2, -2\rangle$ . These correspond to two uncoupled spins where the eigenvectors are not constrained by parity. When we include a small

antiferromagnetic interaction, the eigenvectors should be written as the symmetric/antisymmetric combinations of these states in order that they have definite parities. Thus, the eigenvectors for

the ground states are:  $|+2,+2\rangle$  ( $m = +4$ ),  $|-2,-2\rangle$  ( $m = -4$ ),  $\frac{1}{\sqrt{2}}(|+2,-2\rangle+|-2,+2\rangle)$  ( $m = 0$ ) and

$\frac{1}{\sqrt{2}}(|+2,-2\rangle-|-2,+2\rangle)$  ( $m = 0$ ). For the sake of simplicity, we abbreviate

$\frac{1}{\sqrt{2}}(|m_1,m_2\rangle+|m_2,m_1\rangle)$  as  $|m_1,m_2\rangle_S$  and  $\frac{1}{\sqrt{2}}(|m_1,m_2\rangle-|m_2,m_1\rangle)$  as  $|m_1,m_2\rangle_A$ . With these

eigenvectors, we consider the 1<sup>st</sup>-order correction to the zero-field energies. The inclusion of a small interaction lifts the degeneracy of these states, where

$$\begin{aligned} {}_A\langle +2,-2|\hat{H}|+2,-2\rangle_A &= {}_S\langle +2,-2|\hat{H}|+2,-2\rangle_S = 8d - 4J \\ \langle +2,+2|\hat{H}|+2,+2\rangle &= \langle -2,-2|\hat{H}|-2,-2\rangle = 8d + 4J \end{aligned} \quad (2-2)$$

Therefore, inclusion of  $J$  splits the  $m =$  states from the  $m = \pm 4$  states by  $8J$ . Because the interaction is antiferromagnetic ( $J > 0$ ), when considering the 1<sup>st</sup>-order perturbation, the zero-field ground states of the molecule are  $|+2,-2\rangle_A$  and  $|+2,-2\rangle_S$ , as shown in Figure 2-7(b). The small energy difference between these states originates from high-order corrections, which will be discussed later.

Now we consider the origin of the  $\alpha_1$  and  $\alpha_2$  transitions observed in single-crystal EPR measurements. According to the preceding discussions, the ground states are two  $m = 0$  states. Therefore, the final states associated with  $\alpha_1$  and  $\alpha_2$  transitions must be two  $m = \pm 1$  states. For reasons of simplicity, we only consider the  $m = -1$  states in our analysis. When  $J = 0$ , the eigenvectors for the  $m = -1$  states are  $|-2,1\rangle$ ,  $|1,-2\rangle$ ,  $|-1,0\rangle$  and  $|0,-1\rangle$ , where  $|-2,1\rangle$  and  $|1,-2\rangle$  are the states which are lower in energy. Upon including a small interaction, the eigenvectors of

these low energy  $m = -1$  states are  $|-2, +1\rangle_A$  and  $|-2, +1\rangle_S$ . The energies of these states given by the 1<sup>st</sup>-order perturbation are  ${}_A\langle -2, +1 | \hat{H} | -2, +1 \rangle_A = {}_S\langle -2, +1 | \hat{H} | -2, +1 \rangle_S = 5d - 2J$ . It is important to point out that, when only considering the 1<sup>st</sup>-order correction,  $|+2, -2\rangle_S$  and  $|+2, -2\rangle_A$  are degenerate, and the two excited states,  $|-2, +1\rangle_S$  and  $|-2, +1\rangle_A$  are also degenerate. Hence, the EPR transition associated with the symmetric states,  $|+2, -2\rangle_S$  to  $|-2, +1\rangle_S$ , should be exactly the same energy as the transition between the anti-symmetric states,  $|+2, -2\rangle_A$  to  $|-2, +1\rangle_A$ , which suggests only one ground EPR transition should be observed. The ZFS of these transitions predicted by the 1<sup>st</sup>-order correction equals  $-3d+2J$ , which is 22.2 K (462GHz) according to our parameters. The ZFSs correspond to the  $\alpha_1$  and  $\alpha_2$  branches are 451GHz and 438GHz, respectively, which are in close agreements with the prediction. In the higher order perturbation calculations,  $\hat{H}$  'causes mixing between the states with the same parity and  $m$  value, resulting high order corrections to the eigenvectors. For instance, the eigenvector of the symmetric  $m = 0$  state is composed of linear combinations of  $|2, -2\rangle_S$ ,  $|1, -1\rangle_S$  and  $|0, 0\rangle$  while the eigenvector of the anti-symmetric  $m = 0$  state is composed of linear combinations of  $|2, -2\rangle_A$  and  $|1, -1\rangle_A$ . These corrections lift the degeneracy of the states. Consequently, two distinct transitions,  $\alpha_1$  and  $\alpha_2$ , are observed corresponding to the with the symmetric states and anti-symmetric states, respectively. However, simulations shows that the energies of  $|+2, -2\rangle_S$  and  $|+2, -2\rangle_A$  only differ by 0.03 K, which means that both states have equal population in the experimental temperature range ( $\geq 2$  K). The high order corrections are dominated by  $\hat{H}$  ', which depend only on the coupling constant  $J$ . In our simulations, we noticed that difference between the ZFS of  $\alpha_1$

and  $\alpha_2$  is approximately proportional to  $|J|^3$ , which indicates that it is the result of a 4<sup>th</sup>-order correction in energy.

The simulations of the EPR transitions are shown in Figure 2-7(a). The simulation was performed employing Equation 2-1 with the following parameters:  $d = -5.76$  K,  $e = 0$  and  $J = +2.45$  K. These parameters are constrained by trying to simulate the peak positions of the  $\alpha_1$  and  $\alpha_2$  branches. We note that the single-ion axial anisotropy of the Mn<sup>III</sup> ions is similar to the reported anisotropy values of Mn<sup>III</sup> ions in other elongated octahedrally coordinated complexes<sup>37, 69, 82</sup> and the coupling constant  $J$  is consistent with the previous dc susceptibility study<sup>70</sup> ( $J_z = +3.14$  K,  $J_x = J_y = 4$  K). The preceding discussions show that it is possible to deduce all of the zero-field magnetic parameters from the two ground state transitions observed in single-crystal EPR measurements. The ZFSs of the  $\alpha_1$  and  $\alpha_2$  transitions approximately equal to  $-3d+2J$ , while the splitting between them provides a tight constraint on the interaction  $J$ .

After obtaining the ZFS parameters from single-crystal studies, we returned to the powder spectra to see whether these parameters can explain the many other EPR transitions. Figure 2-8(a) shows the peak positions of the observed EPR transitions collected from a powder sample at 10 K. The transitions are sorted into four different resonance branches:  $\alpha_1$ ,  $\alpha_2$ ,  $\beta$ ,  $\gamma$  and  $\delta$ , as labeled in Figure 2-8(a) on the basis of the peak positions of the high frequency data. As shown in the figure, all of the resonance branches have roughly the same slope, corresponding to the  $g = 2.00$ ,  $|\Delta m| = 1$  EPR transitions, which affirms the simplification of including the axial anisotropy term only. The solid lines in Figure 2-8(a) represent the simulations of EPR transitions while the Figure 2-7(b) is the simulation of the energy diagram. The simulations were performed with the field applied parallel to the molecular z-axis. We also performed simulations upon applying the

magnetic field in the molecular  $xy$ -plane, and the results indicate that the low-temperature EPR transitions in the  $xy$ -orientation will occur at fields above 15 T for the experimental frequencies; thus they are not observed in these experiments. The low field branches,  $\alpha_1$  and  $\alpha_2$ , have been observed and discussed in the single-crystal studies. We focus on the transitions occurring at high fields. The parities of the low energy states are labeled by color in Figure 2-8(b) and the arrows indicate the observed EPR transitions at approximately 650GHz. The final states of these transitions are determined by the EPR selection rules which we discussed previously. The  $\beta$  transition is the  $m = -4 \rightarrow -3$  transition between the symmetric states while the  $\gamma$  and  $\delta$  transitions are the two  $m = -3 \rightarrow -2$  transitions associated to the symmetric and anti-symmetric states, respectively. As shown in Figure 2-8(b), all of the transitions are reasonably explained with the aforementioned selection rules. We note that there are two symmetric  $m = -2$  states, as labeled in Figure 2-8(b). However, simulations reveal that the matrix element associated with transition involving the higher energy  $m = -2$  states (the thick red arrow) is more than 10 times stronger than that of the other transition (the thin red arrow). Therefore, only the stronger transition seems to be observed in the experiments. The powder spectra are consistent with the single crystal studies and confirm the parameters we deduced from single-crystal experiments.

We notice that, although the simulation successfully explains the high frequency results (above 550GHz), we still cannot fully reproduce all of the transitions observed in the lower frequency spectra (below 550GHz), such as the  $\beta_1$  and  $\beta_2$  resonance branches in single crystal studies, as well as several other high field transitions observed in powder spectra between 400GHz and 450GHz. We suspect that this may be due to the fact that we oversimplified the Hamiltonian and neglected transverse anisotropy terms. Including these transverse terms will lead to mixings between different  $m$  states leading to new EPR transitions. In our simulations, we

also noticed that the single-crystal EPR spectra are extremely sensitive to the field orientations. The  $\beta_1$  and  $\beta_2$  transitions may emerge in single-crystal spectra when a small field misalignment is included. However, at high fields and high frequencies, the peak positions are relatively insensitive to small variances of the experimental parameters, where only well defined resonance branches are observed, as shown by the data collected above 600 GHz in powder experiments (Figure 2-8(a)).

### 2.3.2 Magnetic Measurements

In order to validate the results obtained via EPR measurements, we attempted to simulate the reduced magnetization (RM) measurement results with the obtained parameters. The original RM measurements were performed by Dr. Aromi in 2002. However, the result was never published because it could not be interpreted via a simple GSA or MS model, even considering anisotropic interactions<sup>70</sup>. In magnetic measurements, if  $|J| \gg |d|$ , the high temperatures regime is mostly affected by the energy difference between different  $S$ -multiplets set by  $J$ , while the low temperature measurement is strongly influenced by the ZFS of a molecule. Therefore, as we discussed in the data analysis for complex **1**, the general strategy is to fit high temperature dc susceptibility ( $\chi_m T$  vs.  $T$ ) measurements with an isotropic MS Hamiltonian to obtain  $J$ , while the low temperature RM data are fit to a GSA model to deduce  $d$ . However, as shown in our EPR analysis,  $d$  is two times larger than  $J$  in complex **2**. If we consider an isotropic MS model, the energy scale set by  $J$  is about  $|8J|$ , which corresponds to the energy difference between two spins aligned parallel and anti-parallel to each other. On the other hand, the zero-field splitting between the  $|m_i = \pm 2\rangle$  and  $|m_i = 0\rangle$  states for a single  $\text{Mn}^{\text{III}}$  ion equals  $|4d|$ , which approximately equals to  $|8J|$  for **2**, i.e., the energy scales determined by  $d$  and  $J$  are virtually identical in **2**; therefore, both  $d$  and  $J$  have equal influence on the magnetic properties of **2** in all temperature

regimes, which indicates the necessity of including the ZFS anisotropy in analyzing both  $\chi_m T$  and RM data. However, as we discussed in the data analysis for **1**, deducing these parameters from a simple magnetometry measurement can be unreliable. For instance, as we discussed earlier in this chapter, the sign of  $d$  strongly depends on the initial guess value used in the fit.

Furthermore, in the case of **2**, the influence of  $d$  is so strong that it is not possible to determine  $J$  without accurate information about  $d$ .

The experimental and simulated RM results are shown in Figure 2-9. The squares are the experimental data while the solid lines are the simulations employing Equation 2-1 with the parameters obtained via EPR studies. The experimental results show that, at a constant field, the magnetic moment of the sample goes through a maximum and then decreases upon reducing the temperatures. The reduction of the magnetic moment at low temperatures can be understood with the Zeeman diagram shown in Figure 2-8(b), where the molecular ground states are non-magnetic ( $m = 0$ ) at fields below 3.7 T. Therefore, the magnetic moment decreases when lower temperatures. Even at 4 T, the  $m = 4$  state is very close in energy with the  $m = 0$  states, which leads to a reduction of the magnetic moment at low temperatures, as shown in both experiments and simulations. The simulations reproduce the main features of each isofield data curves and give quantitative agreements for the 0.5 T, 1 T and 2 T data. More importantly, the simulations exactly reproduce the maxima positions of the reduced magnetization on the abscissa scale which indicates that the simulations predict the temperatures at which the magnetization saturates with different applied fields. The simulations confirm that the estimations of the anisotropies and the coupling between the  $\text{Mn}^{\text{III}}$  ions are reliable, while the small deviations of the absolute value may come from the Landé  $g$  factor not equal to 2 and/or experimental errors such as the samples being partially aligned by the magnetic field. From simulations we also

noticed that, below 3.7 T, the ground state of the molecule is non-magnetic ( $m = 0$ ) while above 3.7 T the ground state is  $m = -4$ . At low temperatures, when the field is above 3.7 T, a powder sample of complex **2** will face a much stronger torque compared with the torque at lower field. The strong torque can easily cause the sample to be partially aligned. We suspect that this might be the reason why the simulation and experimental data show a larger deviation at 4 T compared to lower field results. In the EPR experiments, when loose constrained powders were used, strong hysteresis loops were also observed due to the mechanical movements of micro-crystals. Such hysteresis loops vanish when the powder samples are well constrained with *n*-eicosane.

## 2.4 Summary

In this chapter we presented EPR studies on two Mn<sup>III</sup> dinuclear molecules and compared the results with magnetic measurements. Complex **1** and **2** show two types of representative EPR spectra which one would expect from ferromagnetic and antiferromagnetic dinuclear molecules, respectively. Good agreements between the EPR measurements and magnetic measurements are obtained in both compounds. The effects of weak coupling are extensively discussed in both **1** and **2**, illustrating the importance of considering both exchange and anisotropy in the analysis of magnetic measurements. In addition, the studies presented in this chapter have paved the road for future pressure studies of these compounds by a recently developed high-frequency EPR technique.

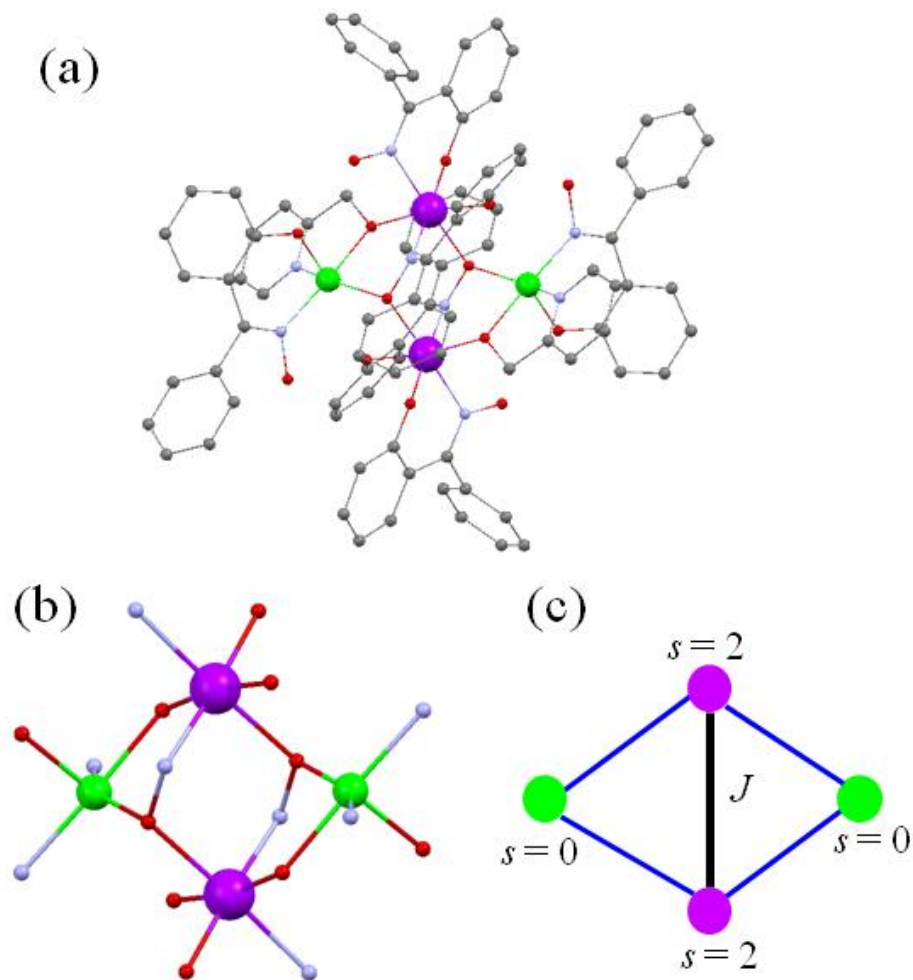


Figure 2-1. The molecular structure and magnetic core of complex **1**. (a) The molecular structure of complex **1**. Color code: Mn = purple, Zn = green, O = red, N = blue and C = black. H-atoms have been omitted for clarity. (b) The magnetic core of complex **1**. Only the metallic atom, their coordination atoms and the chemical bonds between them are shown in the figure. The Jahn-Teller axes (local easy-axes) of Mn<sup>III</sup> ions are defined by the elongated Mn-N bonds, as shown in figure. The two Mn<sup>III</sup> ions are connected by two identical –N-O- bonds. (c) Schematic representation for the magnetic core of **1**.

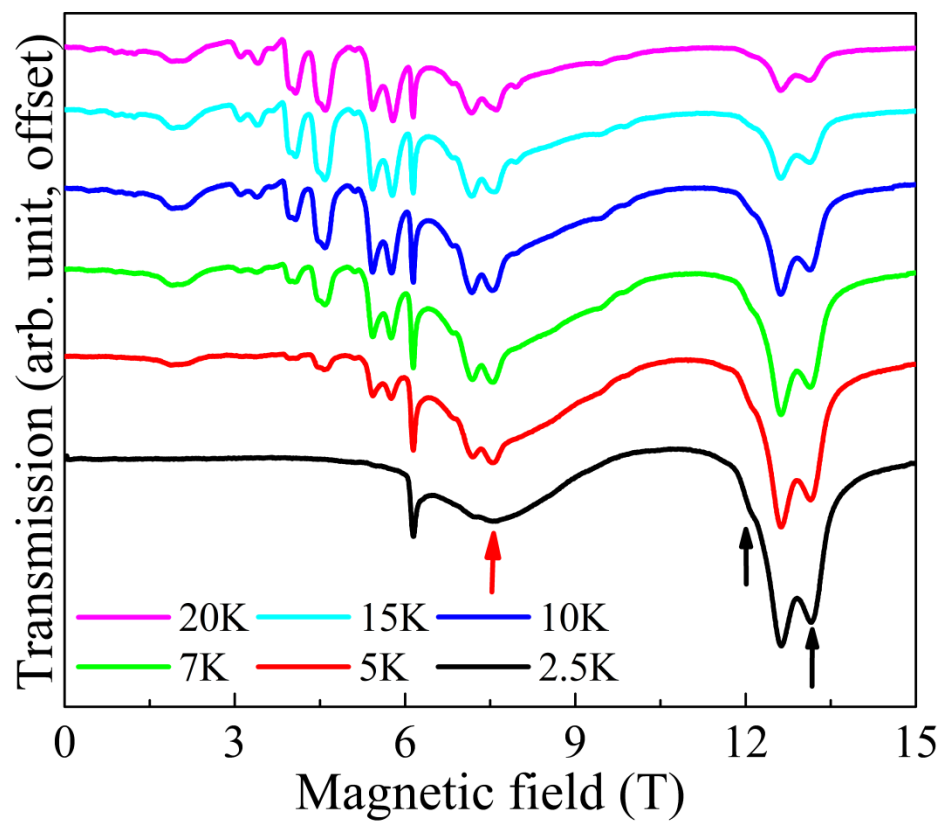


Figure 2-2. Hard plane EPR spectra of complex **1** obtained at 171 GHz as a function of temperature from 20 K (top) to 2.5 K (bottom).

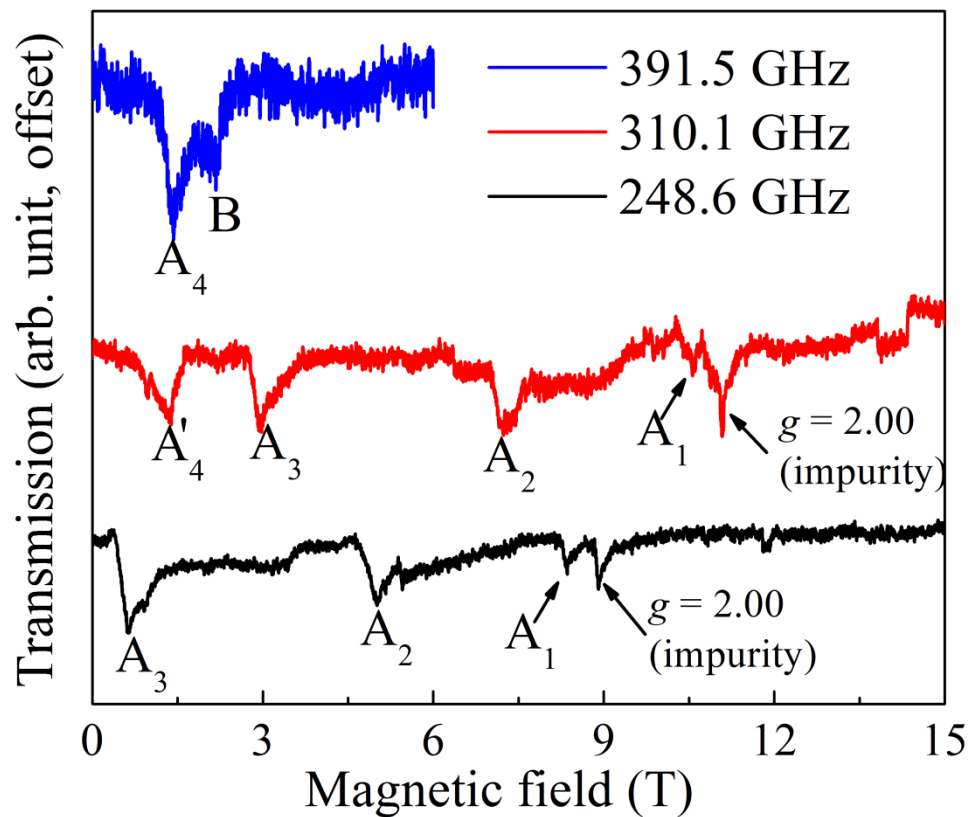


Figure 2-3. Representative easy axis EPR spectra of complex 1 obtained at 2 K (391.5 GHz) and 15 K (310.1GHz and 248.6 GHz). The observed EPR transitions are labeled according to the scheme described in the main text.

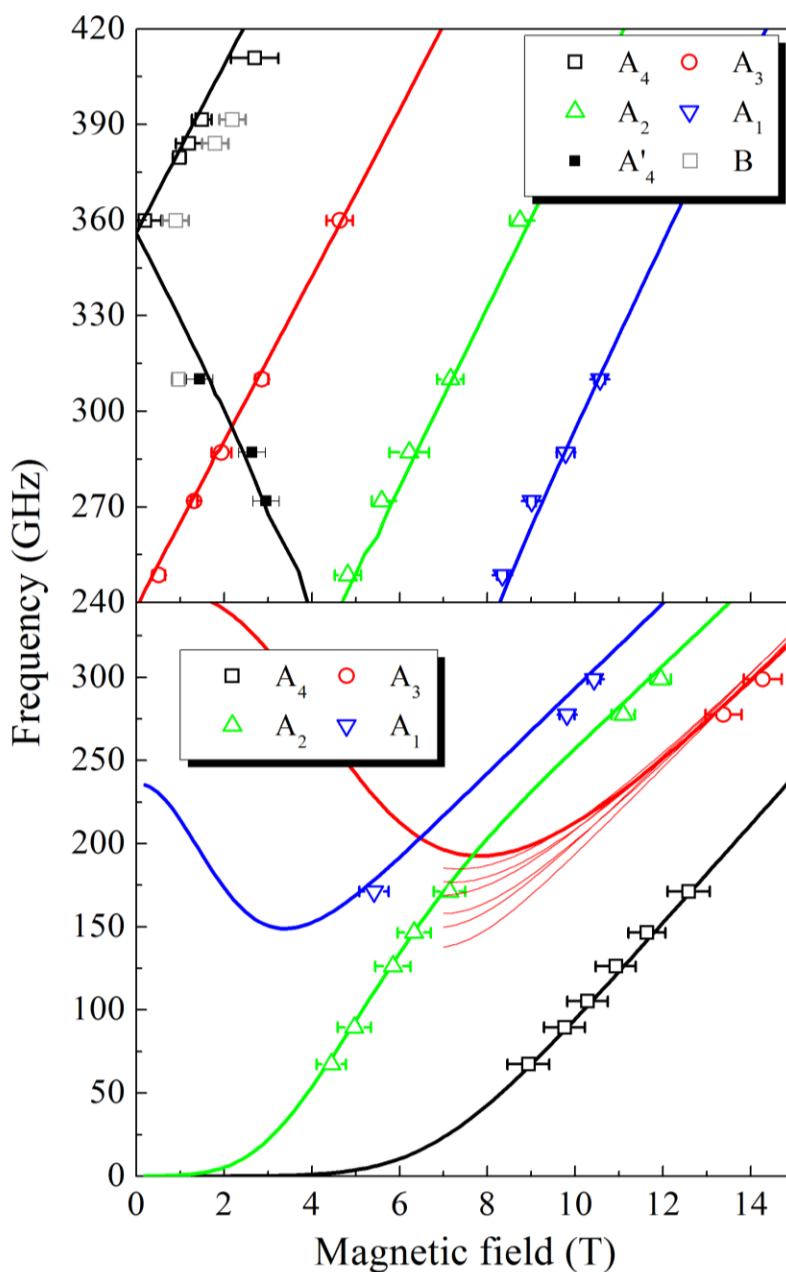


Figure 2-4. Frequency dependence of EPR peak positions of **1**. The data were collected with the field applied (a) close to the molecular easy axis and (b) exactly in the hard plane. The data were mainly collected at 15K; however, data above 360 GHz were collected at 2 K. The thick solid lines are the simulations of the peak positions employing the Hamiltonian and parameters provided in the main text. The thin solid curves in (b) illustrate the influence of applying the field slightly out of the molecular hard plane on the  $A_3$  transition. Each curve represents an increment of  $1^\circ$  of tilting of the field out of the hard plane.

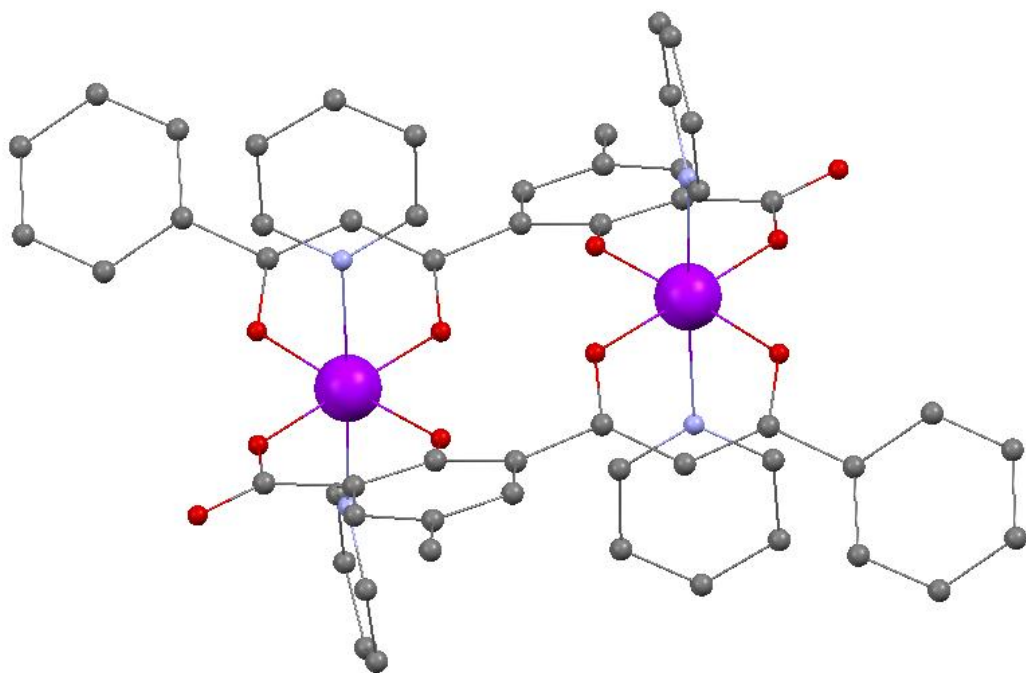


Figure 2-5. The molecular structure of complex **2**. Color code: Mn = purple, O = red, N = blue and C = black. H-atoms have been omitted for clarity.

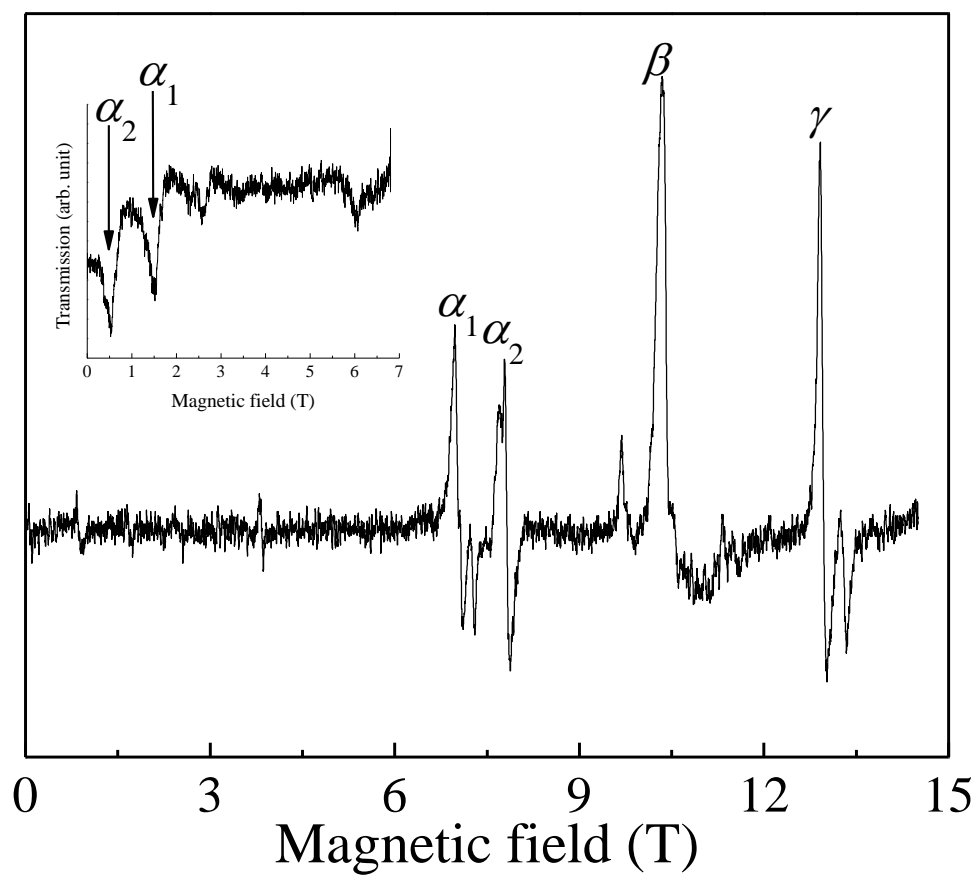


Figure 2-6. EPR spectrum of complex **2** as a powder at 652.8GHz and 10 K, recorded in the first-derivative mode. The EPR transitions have been labeled according to their behavior in the frequency dependence studies (see detailed discussion in the main text). The inset is the spectrum of complex **1** as a single crystal at 418 GHz and 2K recorded in absorption mode, with the orientation of the field being close to the molecular z-axis. Note that this single crystal spectrum was collected with a frequency below the ZFS which results in the order of  $\alpha_1$  and  $\alpha_2$  being reversed comparing with the high frequency spectrum.

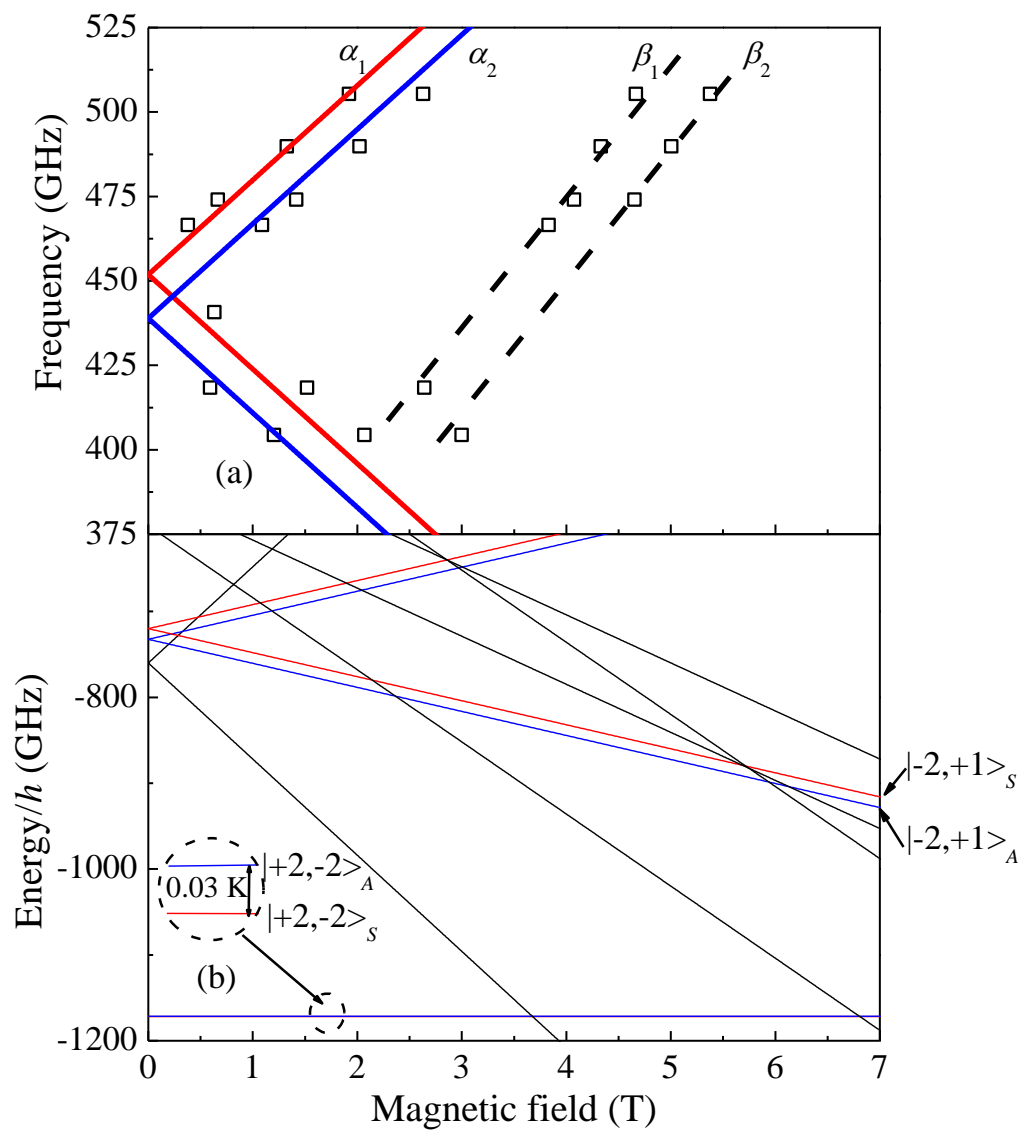


Figure 2-7. Single-crystal EPR studies for complex **2**. (a) Frequency versus field plot showing the EPR peak positions for a single crystal with the field applied close to the molecular z-axis at 2 K. The squares are the experimental data while the solid lines are the simulations of the EPR peak positions. The dash lines are guides to the eyes. Simulations are performed with the Hamiltonian and parameters discussed in the main text. (b) Simulated energy level diagram. The parities of the states are indicated by color where red is even and blue is odd. The 0<sup>th</sup>-order eigenvectors of the states associated with  $\alpha$  transitions are labeled in the figure.

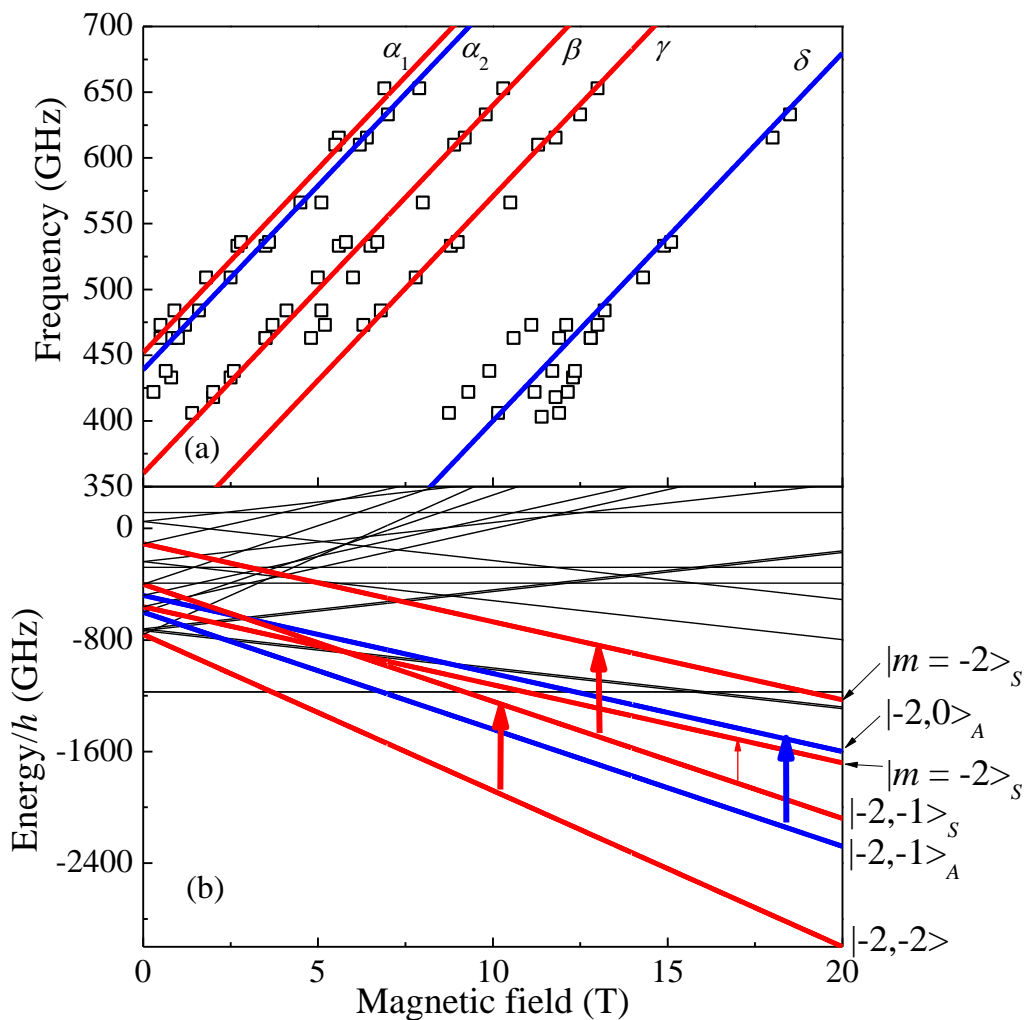


Figure 2-8. Powder EPR studies for complex **2**. (a) Frequency versus field plot showing the EPR peak positions in the powder-sample studies at 10 K. The squares are the experimental data while the solid lines are the simulated EPR peak positions with the field parallel to the molecular z-axis. (b) Simulation of the energy level diagram. The thick lines in (b) are the energy levels between which EPR transitions are observed. The states associated with  $\alpha$  transitions are ignored for clarity. The states are color coded to denote their parities where red stands for even and blue stands for odd. The thick arrows in (b) represent the observed EPR transitions at approximately 650 GHz.

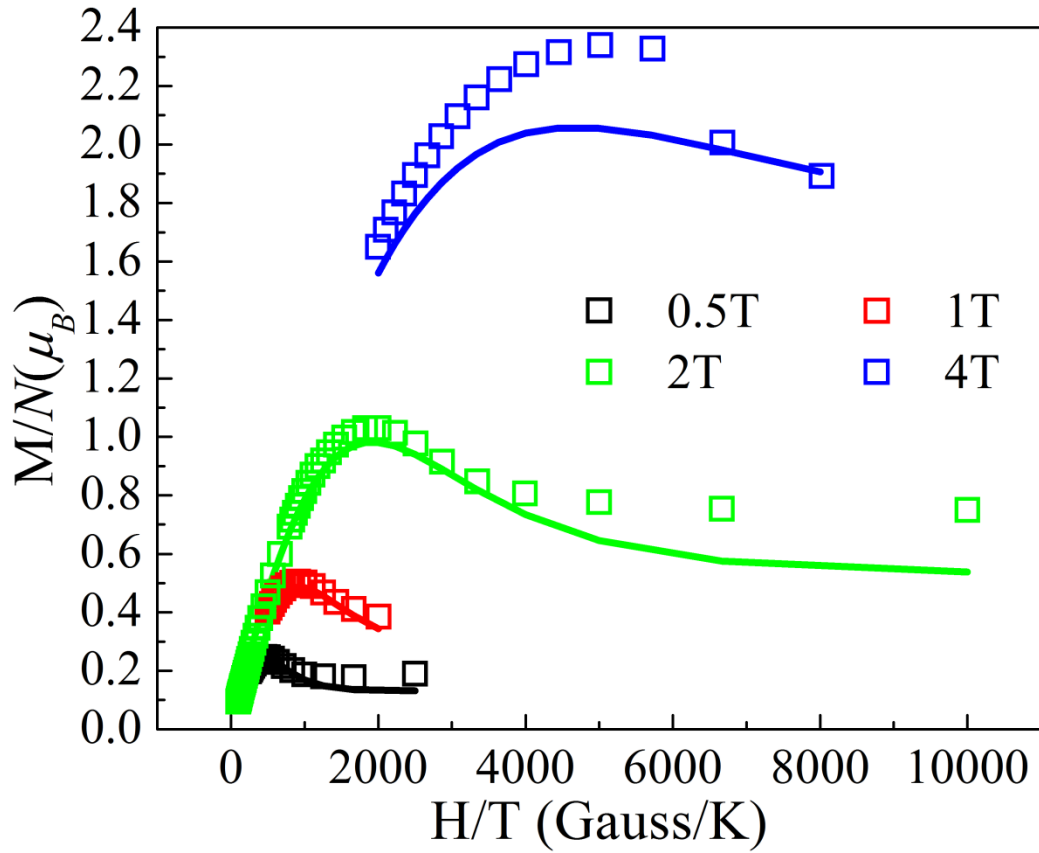


Figure 2-9. Plot of the isofield reduced magnetization measurements. The squares are the experimental results while the solid lines are simulations employing the spin Hamiltonian and parameters provided in the main text.

## CHAPTER 3 QUANTUM TUNNELING OF MAGNETIZATION IN TRIGONAL SINGLE-MOLECULE MAGNETS

Portions of the work presented in this chapter can be found from the following article: Liu, J.; del Barco, E.; Hill, S., Quantum tunneling of magnetization in trigonal single-molecule magnets. *Phys. Rev. B* 2012, 85 (1), 012406. (reused with permission from American Physical Society)

### 3.1 Introduction

Quantum Tunneling of magnetization (QTM) in single-molecule magnets (SMM) is important for both scientific reasons as well as applications in quantum information technologies. While QTM could be exploited for creating quantum superposition states necessary for quantum computation<sup>2</sup>, it also leads to demagnetization in SMMs which is a disadvantage for classical information storage. Thus it is important to both understand and control the origin of QTM in SMMs. Extensive theoretical and experimental works have been performed to understand QTM in biaxial<sup>39, 83, 84</sup> and tetragonal<sup>85</sup> SMMs. In addition, QTM in spin systems with both rhombic and four-fold transverse anisotropies has been discussed from various points-of-view.<sup>55, 86-88</sup> An outstanding example is the observation of Berry-phase interference (BPI) in SMMs<sup>39</sup>, which signifies the importance of molecular symmetry in QTM. However, so far only scarce works have been conducted to understand QTM in SMMs with trigonal topology.<sup>89</sup>

Crucially speaking, at zero transverse fields, the symmetry of a SMM should determine the spin selection rules in QTM. Without applying a transverse field, the selection rules of QTM should be entirely decided by the zero-field transverse part of a Hamiltonian,  $\hat{H}'$ . As we discussed in Chapter 1,  $\hat{H}'$  is constrained by the rotational symmetry of a molecule. Generally speaking, for a molecule with  $q$ -fold rotational symmetry, QTM can only occur between the

states with  $|\Delta m|$  equal to multiples of  $q$ . Surprisingly, in most QTM experiments performed on SMMs, non-zero tunneling steps are found for all level crossings regardless of the associated  $|\Delta m|$  values .

Recently, a new SMM,  $[\text{NE}_4]_3[\text{Mn}_3\text{Zn}_2(\text{salox})_3\text{O}(\text{N}_3)_6\text{Cl}_2]$  (hereafter  $\text{Mn}_3$ )<sup>16, 37, 90, 91</sup>, with exact  $C_3$  symmetry has been synthesized and studied. Clear evidences of quantum mechanical spin selection rules have been observed.<sup>91</sup> Motivated by the recent experimental studies of this  $\text{Mn}_3$  SMM, we carried out theoretical investigations on QTM in SMMs with trigonal symmetry.

We focus on studying the origin of the three-fold transverse anisotropy  $\hat{O}_4^3 (= \frac{1}{2}[\hat{S}_z, \hat{S}_+^3 + \hat{S}_-^3])$  as well as several fascinating phenomena generated by this interaction. For comparison, we also consider QTM in a  $[\text{Ni}(\text{hmp})(\text{dmb})\text{Cl}]_4$  SMM (hereafter  $\text{Ni}_4$ ) with  $S_4$  symmetry<sup>13, 33, 35, 92, 93</sup> to show the uniqueness of  $C_3$  symmetry.

## 3.2 Quantum Tunneling of Magnetization in the $\text{Mn}_3$ Single-Molecule Magnet

### 3.2.1 The $\text{Mn}_3$ Single-Molecule Magnet

The  $\text{Mn}_3$  SMMs crystallize in a trigonal space group  $R3c$  with a racemic mixture of  $C_3$  symmetric chiral molecules. The structure of the  $\text{Mn}_3$  molecule is shown in Figure 3-1(a). The magnetic core is constituted by three ferromagnetically coupled  $\text{Mn}^{\text{III}}$  ( $s = 2$ ) ions, which form the  $\text{Mn}_3$  plane, with two  $\text{Zn}^{\text{II}}$  ions located above and below the the  $\text{Mn}_3$  plane, forming a trigonal bipyramidal structure. The  $C_3$  axis of the molecule is perpendicular to  $\text{Mn}_3$  plane. Figure 3-1(b) shows the magnetic core of the molecule with the local easy-axes of the individual spins defined by the Jahn-Teller (JT) elongation axes of the  $\text{Mn}^{\text{III}}$  ions. The resultant spin  $S = 6$  ground state experiences a relatively high barrier to magnetization relaxation ( $U_{\text{eff}} \sim 50$  K). Importantly, clear evidences of quantum mechanical selection rules have been observed in QTM measurements.<sup>91</sup>

The Mn<sub>3</sub> SMM provides an ideal opportunity to explore the consequences of a trigonal spin topology in terms of the resultant QTM. We do so via numerical comparisons between the giant-spin approximation (GSA) and multi-spin (MS) formalism. The GSA treats the total spin  $S$  associated with the ground state of a molecule to be exact. For Mn<sub>3</sub>, this results in  $2S + 1$  ( $= 13$ ) multiplet states that can be described by the following effective spin Hamiltonian:

$$\hat{H} = D\hat{S}_z^2 + B_4^0\hat{O}_4^0 + B_4^3\hat{O}_4^3 + B_6^0\hat{O}_6^0 + \mu_B\vec{B}\cdot\vec{g}\cdot\hat{S} \quad (3-1)$$

The Stevens operators included in this Hamiltonian have been introduced in Chapter 1. Here, we consider only 2<sup>nd</sup> and 4<sup>th</sup> order axial ( $p = 2, 4; q = 0$ ) terms, and the leading trigonal ( $\hat{O}_4^3$ ) and hexagonal ( $\hat{O}_6^0$ ) operators. The first term in Equation 3-1 is the dominant 2<sup>nd</sup> order axial anisotropy (where  $D = 3B_2^0$ ) that gives rise to the energy barrier between “spin up” and “spin down” states.

The advantage of the GSA lies in the fact that one need only deal with a few parameters and a small Hamiltonian matrix. However, the GSA ignores the internal degrees of freedom within the molecule, thus completely failing to capture the underlying physics in cases where the total spin can fluctuate.<sup>11, 34, 36, 37</sup> Apart from that, one of the main objectives of our work is to investigate the origin of high order transverse anisotropies. Therefore, a more physical model, which takes into account the zero-field splitting (ZFS) tensors of individual ions and the coupling between them, is given by the MS Hamiltonian:

$$\hat{H} = \sum_i \hat{s}_i \cdot \vec{R}_i^T \cdot \vec{d}_i \cdot \vec{R}_i \cdot \hat{s}_i + \sum_{j>i} J_{ij} \hat{s}_i \cdot \hat{s}_j + \sum_i \mu_B \vec{B} \cdot \vec{g}_i \cdot \hat{s}_i \quad (3-2)$$

Here,  $\hat{s}_i$  are spin operators associated with the uncoupled  $s = 2$  Mn<sup>III</sup> ions. The diagonal matrices,  $\vec{d}_i$ , parameterize the 2<sup>nd</sup> order ZFS in the local coordinate frame of each Mn<sup>III</sup> ion, with  $d_{xx,i} = -d_{yy,i} = e_i$  and  $d_{zz,i} = d_i$ , where  $d_i$  and  $e_i$  are the respective axial and rhombic ZFS

parameters. The local coordinate frames are then transformed into the molecular frame by means of rotation matrices,  $\vec{R}_i$ , specified by Euler angles  $\theta_i$ ,  $\varphi_i$  and  $\psi_i$ , where  $\theta_i$  is the angle between the local z-axis (JT axis) and the molecular  $C_3$  axis. The second term represents the isotropic exchange between the  $i^{\text{th}}$  and  $j^{\text{th}}$  spins, with  $J_{ij}$  parameterizing the strength of this coupling on each bond, and the final term is the Zeeman interaction.

$\text{Mn}_3$  is particularly attractive in the context of the present investigation. The dimension of the MS Hamiltonian matrix for three  $s = 2$  spins is just  $[(2s + 1)^3]^2 = 125 \times 125$ . The high ( $C_3$ ) symmetry then reduces the number of interaction parameters to just a single exchange constant,  $J$ , and identical  $d$  and  $e$  values for each ion. Two of the Euler angles are known from x-ray studies<sup>16</sup>, and the remaining parameters have been determined from EPR and QTM measurements.<sup>16, 37, 90</sup>  
<sup>91</sup> Lastly, the structure contains no solvent molecules. This is rare among SMMs<sup>35</sup> and removes a major source of disorder.<sup>94</sup> Consequently, exceptional spectroscopic data (QTM and EPR) are available against which one can test theoretical models.

### 3.2.2 Quantum Tunneling of Magnetization in $\text{Mn}_3$

We focus on the transverse ZFS operators in the GSA ( $q > 0$ ), particularly  $\hat{O}_4^3$ , which we show to be responsible for several fascinating results. The effects of  $q > 0$  ZFS terms typically manifest themselves at energy scales that are orders of magnitude smaller than those of the axial ( $q = 0$ ) terms. We thus focus on the tunneling gaps at avoided level crossings, as these are dominated by the transverse terms in Equation 3-1. Due to symmetry restrictions ( $q = 3n$  for  $C_3$  symmetry, where  $n$  is an integer), non-zero tunneling gaps are limited to level crossings with  $|\Delta m| = 3n$ , where  $m$  is the projection of the total spin onto the  $C_3$  (z-) axis. All such gaps,  $\Delta_{\overline{mm}'}$ , have been labeled in Figure 3-2 for QTM resonances  $k \leq 3$ , where  $k$  ( $= m + m'$ ) denotes an avoided crossing between pairs of levels with spin projections  $m$  and  $m'$  (an overbar denotes

negative  $m$ ). Published ZFS parameters were employed for simulations involving Equation 3-2, i.e.,  $d = -4.2$  K and  $e = 0.9$  K.<sup>91</sup> Meanwhile, the exchange constant  $J$  ( $= -10$  K) was set to a larger absolute value to isolate the ground state from excited multiplets, thus simplifying analysis of higher-lying gaps, as shown in Figure 3-3. With  $J = -4.88$  K, which is the value determined by experiments<sup>91</sup>, the excited spin multiplets ( $S < 6$ ) overlap with the ground  $S = 6$  multiplet at low fields, which complicates analysis of excited QTM resonances, such as the  $\Delta_{\bar{1}2}$  resonance. The influences of  $J$  will be discussed later. The Euler angles were set to  $\varphi_1 = 0$ ,  $\varphi_2 = 120^\circ$  and  $\varphi_3 = 240^\circ$  (all  $\psi_i = 0$ ) to preserve  $C_3$  symmetry, while  $\theta_i$  ( $= \theta$ ) was allowed to vary in order to examine its influence on QTM selection rules.

We first consider the situation in which the Jahn-Teller (JT) axes of the three  $\text{Mn}^{\text{III}}$  ions are parallel to the  $C_3$  axis, i.e.,  $\theta = 0$ . In the top section of Table 3-1, we give the magnitudes of even- $n$  tunneling gaps involving pairs of levels with  $|\Delta m| = 3n$  deduced via diagonalization of Equation 3-2 in the absence of a transverse field,  $H_T$  ( $\perp z$ ). The odd- $n$ ,  $H_T = 0$  gaps are identically zero, as can be seen from their dependence on  $H_T$  (Figure 3-2 inset): the power-law behavior indicates no contribution from ZFS interactions (at  $H_T = 0$ ). Consequently, one expects only even- $n$  ZFS terms of the form  $B_p^{3n} \hat{O}_p^{3n}$  in the GSA: those satisfying this requirement have six-fold rotational symmetry about the  $C_3$  axis, i.e., a higher symmetry than the real molecule (further explanation is given below).

To compare models for the  $\theta = 0$  case we calculated the non-zero tunneling gaps, setting  $B_4^3 = 0$ ,  $D = 1.096$  K and  $B_4^0 = -2.18 \times 10^{-5}$  K in Equation 3-1. In the absence of a transverse field, the  $n = 2$  gaps  $\Delta_{\bar{3}3}$  and  $\Delta_{\bar{2}4}$  are proportional to  $B_6^6$ , while the  $n = 4$  gap,  $\Delta_{\bar{6}6}$ , is proportional to  $(B_6^6)^2$ . This can be traced to the order of perturbation at which the gaps appear, e.g., by treating

the  $m_s = \pm 3$  states as a two-level system, we find that  $\Delta_{\pm 3} = B_6^6 \langle -3 | \hat{O}_6^6 | +3 \rangle = 60480 B_6^6$  based on a first order perturbation calculation. The best overall agreement between the two models is obtained by setting  $B_6^6 = 4.3 \times 10^{-7}$  K (Table 3-1). Small differences may be due to our neglect of higher-order six-fold terms such as  $B_8^6 \hat{O}_8^6$ ,  $B_{10}^6 \hat{O}_{10}^6$ , *etc.*

Table 3-1. Comparison of tunneling gaps obtained from the MS and GS models for resonances  $k = 0, 1, 2$  and  $3$ , for the two cases  $\theta = 0$  (top) and  $\theta = 8.5^\circ$  (bottom).

$k$	$n$	$\Delta$	GS-gap (K)	MS-gap (K)	Ratio (GS/MS)
Jahn-Teller axes parallel to the molecular z-axis					
0	2	$\Delta_{(-3,3)}$	$2.60 \times 10^{-2}$	$2.66 \times 10^{-2}$	0.98
0	4	$\Delta_{(-6,6)}$	$1.10 \times 10^{-6}$	$1.05 \times 10^{-6}$	1.05
2	2	$\Delta_{(-2,4)}$	$2.37 \times 10^{-2}$	$2.35 \times 10^{-2}$	1.01
Jahn-Teller axes tilted $\theta = 8.5^\circ$ away from the molecular z-axis					
0	2	$\Delta_{(-3,3)}$	$2.76 \times 10^{-2}$	$2.91 \times 10^{-2}$	0.95
0	4	$\Delta_{(-6,6)}$	$1.26 \times 10^{-6}$	$1.25 \times 10^{-6}$	1.01
1	3	$\Delta_{(-4,5)}$	$4.68 \times 10^{-5}$	$4.19 \times 10^{-5}$	1.12
1	1	$\Delta_{(-1,2)}$	$6.33 \times 10^{-2}$	$6.31 \times 10^{-2}$	1.00
2	2	$\Delta_{(-2,4)}$	$2.45 \times 10^{-2}$	$2.61 \times 10^{-2}$	0.94
3	3	$\Delta_{(-3,6)}$	$8.66 \times 10^{-5}$	$7.53 \times 10^{-5}$	1.15
3	1	$\Delta_{(0,3)}$	$1.76 \times 10^{-1}$	$1.76 \times 10^{-1}$	1.00

Next we consider the situation in which the JT axes are tilted  $\theta = 8.5^\circ$  away from the  $C_3$  axis, as is the case for  $Mn_3$ .<sup>16</sup> Both even- and odd- $n$   $H_T = 0$  tunneling gaps are generated in this situation, i.e., odd QTM resonances become allowed. This may be understood within the framework of the GSA as being due to the emergence of ZFS interactions possessing three-fold rotational symmetry about the molecular  $C_3$  axis, i.e.,  $B_p^{3n} \hat{O}_p^{3n}$  with  $n = 1$  and  $p > 3$ ; the leading term is  $B_4^3 \hat{O}_4^3$ . We begin by considering  $\Delta_{\pm 2}$  ( $k = 1$ ) and  $\Delta_{03}$  ( $k = 3$ ), which depend only on  $B_4^3 \hat{O}_4^3$  to first order. A perturbation analysis gives  $\Delta_{\pm 2} = 132 B_4^3$  and  $\Delta_{03} = 368 B_4^3$ . By comparing with MS simulations (Equation 3-20, we obtained  $B_4^3 = 4.77 \times 10^{-4}$  K. The remaining gaps are then evaluated via diagonalization of Equation 3-1 using the optimum  $B_6^6$  and  $B_4^3$  parameters.

Excellent agreement is once again achieved (see Table 3-1). Minor deviations may, in principle, be corrected by introducing higher-order transverse terms such as  $B_6^3 \hat{O}_6^3$ .

The emergence of the  $B_4^3 \hat{O}_4^3$  interaction clearly signifies a lowering of the symmetry of the ZFS Hamiltonian upon tilting the JT axes. To understand this one needs to consider both the symmetry of the molecule and the intrinsic symmetry of the ZFS tensors of the individual ions. Considering only 2<sup>nd</sup> order ZFS, the Hamiltonian of a single Mn<sup>III</sup> ion possesses  $D_{2h}$  symmetry, with three mutually orthogonal  $C_2$  axes. When the JT axes are parallel ( $\theta = 0$ ), the local  $z$ -axis of each Mn<sup>III</sup> coincides with the molecular  $C_3$  axis. The resultant ZFS Hamiltonian then possesses  $C_3 \times C_2 \times C_i = C_{6h}$  symmetry (see Figure 3-4(a)), requiring  $B_4^3 = 0$ ; the additional  $C_i$  symmetry arises from the time-reversal invariance that guarantees an identical spectrum upon inversion of the total field (or, in the classical limit, inversion of the total spin). In contrast, when the JT axes are tilted, the  $C_2$  and  $C_3$  axes do not coincide. The rotational symmetry then reduces to three-fold and, hence,  $B_4^3 \hat{O}_4^3$  is allowed; the symmetry in this case is  $C_3 \times C_i = S_6$  (see Figure 3-4(b)).

The preceding arguments may be reinforced via group theoretic considerations without involving an exact expression of the Hamiltonian. When the external magnetic field is applied along the molecular  $z$ -axis, the  $C_{6h}$  symmetry reduces to  $C_6$ , and the 13 basis functions of the  $S = 6$  Hilbert space fall into six distinct one-dimensional irreducible representations.<sup>95</sup> By investigating how these basis functions behave under a  $C_6$  rotation, we can sort them as follows:  $| -6 \rangle, | 0 \rangle, | +6 \rangle \in \Gamma_1$ ;  $| -2 \rangle, | +4 \rangle \in \Gamma_2$ ;  $| +2 \rangle, | -4 \rangle \in \Gamma_3$ ;  $| +3 \rangle, | -3 \rangle \in \Gamma_4$ ;  $| +1 \rangle, | -5 \rangle \in \Gamma_5$ ;  $| +5 \rangle, | -1 \rangle \in \Gamma_6$ , where  $\Gamma_{1..6}$  are the six irreducible representations following the Bethe notation.<sup>95</sup> Because the Hamiltonian operator belongs to the totally symmetric representation,  $\langle m | \hat{H} | m' \rangle$  is non-zero only when  $| m \rangle$  and  $| m' \rangle$  belong to the same representation.<sup>96</sup> As can be

seen, such states have  $|\Delta m| = 3n$ , with  $n$  even, which is the criterion for state mixing in  $C_6$  symmetry. When the symmetry of the ZFS Hamiltonian is reduced to  $S_6$  ( $C_3$  upon application of  $B//z$ ) the basis functions fall into three different irreducible representations:  $|0\rangle, |\pm 3\rangle, |\pm 6\rangle \in \Gamma_1$ ;  $|+4\rangle, |+1\rangle, |-2\rangle, |-5\rangle \in \Gamma_2$  and  $|-4\rangle, |-1\rangle, |+2\rangle, |+5\rangle \in \Gamma_3$ . Here, the selection rule for mixing is  $|\Delta m| = 3n$ , again in agreement with the above calculations.

An important consequence of the preceding analysis is the demonstration of the existence of odd  $k$  QTM resonances, i.e., a quite realistic parameterization of Equation 3-2 generates ZFS terms in the GSA containing odd powers of  $\hat{S}_+$  and  $\hat{S}_-$ . This dispels the notion that odd QTM resonances *cannot* be generated via ZFS interactions.<sup>97</sup> These ideas ought to apply quite generally, e.g., the disorder potential associated with the distortion of a symmetric molecule likely contains ZFS terms (e.g.  $\hat{O}_4^3$ ) that unfreeze odd QTM resonances. It remains to be seen whether this can account for the absence of selection rules in SMMs such as  $Mn_{12}$ .<sup>97</sup> We note also that these arguments do not apply to zero-field ( $k = 0$ ) QTM in half-integer spin systems, which is strictly forbidden according to Kramers' theorem.<sup>89</sup>

The  $J$  dependence of higher-order ( $p \geq 4$ ) coefficients in the GSA has been discussed in the context of other high symmetry SMMs.<sup>35, 37, 98-100</sup> In these situations, the 2<sup>nd</sup> order contributions to the transverse anisotropy ( $q > 0$ ) cancel exactly, emerging at higher orders as a consequence of the mixing of spin states. This is illustrated for  $Mn_3$  in Figure 3-5, which plots the power law dependence of several tunneling gaps as a function of the ratio of  $J/d$ ; the parameter values given above were employed in these calculations. It is found that the gaps are proportional to  $|J|^{-n}$ , i.e.,  $B_4^3 \propto |J|^{-1}$  and  $B_6^6 \propto |J|^{-2}$ .<sup>37</sup> Note that this implies a complete suppression of QTM in the strong coupling limit ( $|J| \gg |d|$ ).

### 3.2.3 Berry-Phase Interference in Mn<sub>3</sub>

We conclude the studies on Mn<sub>3</sub> by focusing on the transverse field ( $H_T$ ) dependence of the tunneling gaps generated by  $\hat{O}_4^3$  and  $\hat{O}_6^6$ . The influence of the former is rather straightforward: the  $C_{6h}$  symmetry (see Figure 3-4(a)) guarantees six-fold modulations of the tunneling gaps in all allowed resonances, regardless of whether a longitudinal field,  $H_L$  ( $//z$ ), is present;  $\hat{O}_6^6$  also generates hexagonal Berry-phase interference (BPI) patterns (due to quenching of the tunneling<sup>39, 85, 91</sup>) upon rotation of  $H_T$  within the  $xy$ -plane, as shown in Figure 3-6. Figure 3-6 shows the  $k = 0$  BPI pattern generated when only including  $B_6^6$  ( $B_4^3 = 0$ ). This BPI pattern for the  $k = 0$  resonance exhibits hexagonal symmetry, with the resonance field located at  $H_L = 0$ , exactly.

By contrast, the influence of  $\hat{O}_4^3$  is quite fascinating. In order to simplify the discussion, Figure 3-4(c) was generated with  $B_6^6 = 0$ . We first examine the dependence of  $\Delta_{\bar{66}}^6$  ( $k = 0$ ) and  $\Delta_{\bar{36}}^3$  ( $k = 3$ ) for a fixed value of  $H_T$  (see Figure 3-4(c)). As anticipated,  $\Delta_{\bar{36}}^3$  exhibits a three-fold modulation which rotates  $60^\circ$  upon inversion of  $H_L$  (dashed curves), as required on the basis of the time-reversal invariance of Equation 3-1, i.e.,  $\Delta_{\bar{36}}^3$  is invariant to inversion of the total field. The figure does not convey the fact that it was also necessary to vary  $H_L$  in order to exactly locate the gap minima, i.e.,  $H_T$  influences the exact  $H_L$  locations of the resonances, a behavior that is well documented for  $k > 0$  resonances observed for other SMMs. The corresponding modulation of  $H_L$  also exhibits a three-fold pattern for either polarity.

The behavior of  $\Delta_{\bar{66}}^6$  is yet more intriguing. One might expect a six-fold behavior given the requirement that the spectrum be invariant under inversion of  $H_T$ . However, this assumes that  $H_L = 0$ . In fact, application of a transverse field causes a shift of the  $k = 0$  resonance away from  $H_L = 0$ , as illustrated in Figure 3-4(d). Only a very weak modulation of  $\Delta_{\bar{66}}^6$  is observed upon

rotation of a 0.2 T transverse field; the modulation pattern is indeed six-fold (solid curve in Figure 3-4(c)). However, the corresponding modulation of  $H_L$  exhibits a three-fold pattern (dotted and dash-dotted curves in Figure 3-4(c)). One way to interpret this result is to view the  $\hat{O}_4^3$  operator as generating an effective internal longitudinal field,  $H_L^*$ , under the action of an applied transverse field;  $H_L^*$  is then responsible for the shift of the  $k = 0$  resonance from  $H_L = 0$ .

Indeed, one can see this from inspection of the form of the  $\hat{O}_4^3 = \frac{1}{2}[\hat{S}_z, \hat{S}_+^3 + \hat{S}_-^3]$  operator, which, unlike even- $q$  interactions, contains an odd power of  $\hat{S}_z$ , akin to the Zeeman interaction with  $H//z$ . An alternative view may be derived from the  $S_6$  surface depicted in Figure 3-4(b), where one sees that the hard/medium directions do not lie within the  $xy$ -plane, contrary to the case for the  $C_{6h}$  surface in Figure 3-4(a) (or quite generally for any even- $q$  operator<sup>84</sup>). In other words, the classical hard plane is not flat, but corrugated with a  $120^\circ$  periodicity. Consequently, application of a longitudinal field is required in order to insure that the total field is within the hard plane when rotating  $H_T$ .

Figure 3-7 illustrates the shift of  $H_L$  for  $\Delta_{\bar{6}6}$  upon applying  $H_T$  at several representative orientations in the molecular  $xy$ -plane. Upon the application of  $H_T$ ,  $H_L$  is shifted to  $+z$  at  $0^\circ$  and  $-z$  at  $60^\circ$ , which is consistent with the classical energy potential shown in Figure 3-4(b). However, we note that this classical potential surface cannot explain the shifts of  $H_L$  quantitatively. It is notable that  $H_L$  is not a linear function of  $H_T$ , which indicates that the exact location of the molecular hard plane depends on the magnitude of the applied transverse field. The quantum molecular hard plane is not flat and also exhibits a  $120^\circ$  periodicity, which is similar to the classical energy potential analog. However, the hard plane is also field-dependent: its exact

shape varies as a function of the magnitude of  $H_T$ , which is different to the classical zero-field energy potential surface.

Finally, Figure 3-8 shows the patterns of BPI minima for  $k = 0$  (a) and  $k = 3$  (b), generated purely from the  $B_4^3 \hat{O}_4^3$  interaction. The  $k = 0$  pattern in (a) is hexagonal. However, the coloring indicates the polarity of the compensating longitudinal field,  $H_L$ . Thus, on the basis of the sign of  $H_L$ , one sees that the BPI minima exhibit a three-fold rotational symmetry. In contrast, the  $k = 3$  BPI minima exhibit obvious trigonal patterns, regardless of the behavior of the compensating  $H_L$  field. Observation of these BPI patterns in  $Mn_3$  is complicated by several factors, including strong avalanches<sup>91</sup> and the existence of two molecular orientations with opposite chiralities, where the two species are rotated  $\sim 27^\circ$  respect to each other (with parallel  $C_3$  axes);<sup>16, 90</sup> we note that it may be possible to select and study one species via hole-burning.<sup>87</sup> This technique involves sweeping  $H_L$  in the presence of  $H_T$  during initially polarizing the sample. With application of  $H_T$  at a certain orientation, e.g., along the intermediate axis of one molecule species, these molecules will have a larger tunnel splitting; therefore, the magnetic moments of these molecules are more likely to relax when  $H_L$  is swept through a QTM resonance. These molecules can then be studied on the negative side of the hysteresis loop ( $-H_L$ ); therefore, by manipulating  $H_T$ , it is possible to selectively polarize a portion of the sample for BPI studies. The primary motivation for the present theoretical study is to stimulate future measurements on  $Mn_3$  or one of several other SMMs known to possess  $C_3$  symmetry.<sup>89</sup>

### **3.3. Quantum Tunnel of Magnetization in the $Ni_4$ Single-Molecule Magnet**

#### **3.3.1 The $Ni_4$ Single-Molecule Magnet**

We conclude this chapter by comparing the preceding results with QTM in the  $Ni_4$  SMM which possesses even-fold rotational symmetry. The structure of the  $Ni_4$  SMM is shown in

Figure 3-9(a). The molecule possesses  $S_4$  symmetry with the  $S_4$ -axis shown in Figure 3-9(a). This complex crystallizes in an  $I4_1/a$  space group without any lattice solvent molecule.<sup>33, 35, 92</sup> The magnetic core of the molecule is a slightly distorted cube with four  $\text{Ni}^{\text{II}}$  ions ( $s = 1$ ) located on opposite corners, as sketched in Figure 3-9(b). The four  $\text{Ni}^{\text{II}}$  ions are ferromagnetically coupled which leads to a spin  $S = 4$  molecular ground state. The complex exhibits extremely fast quantum tunneling which significantly decreases the effective relaxation barrier which was unable to be directly measured by low temperature ac susceptibility measurements ( $|DS^2| \approx 13 \text{ K}$ ).<sup>93</sup> The molecule can be described with the following spin Hamiltonian:

$$\hat{H} = \sum_i \hat{s}_i \cdot \vec{n}_i^T \cdot \vec{d}_i \cdot \vec{n}_i \cdot \hat{s}_i + \sum_{j>i} J_{ij} \hat{s}_i \cdot \hat{s}_j + \sum_i \mu_B \vec{B} \cdot \vec{g}_i \cdot \hat{s}_i \quad (3-3)$$

This Hamiltonian differs from Equation 3-2 only in that the rotational matrices,  $\vec{R}_i$ , are replaced by  $\vec{n}_i$ , which take improper rotations into account. The reason for this substitution is due to the different natures of rotations and improper rotations. An improper rotation can be achieved in two steps: i) a rotation about a given axis and a reflection about ii) a plane which is perpendicular to the rotation axis. It should be noted that a reflection operation cannot be described by a rotation matrix. The simplest way to view this is that the determinant of a rotation matrix is 1, while the determinant of a reflection matrix is -1. Therefore, if the local coordination frame of the  $i^{\text{th}}$  ion is related to the molecular frame by a rotation (identity or  $C_2$ ),  $\vec{n}_i = \vec{R}_i$ ; if the local coordination frame of the  $i^{\text{th}}$  ion is transformed into the molecular coordination frame via an improper rotation ( $S_4$  or  $S_4^3$ ),  $\vec{n}_i = \sigma \vec{R}_i$  ( $\sigma$  is reflection).

The  $\text{Ni}_4$  SMM is a particularly ideal platform for this comparison with  $\text{Mn}_3$ . The molecule possesses a well separated  $S = 4$  ground state with the  $S = 3$  excited spin multiplets located roughly 30 K above in energy. The  $3 \times 3$  Hamiltonian matrix associated with a single  $\text{Ni}^{\text{II}}$  ion

contains only two 2<sup>nd</sup>-order ZFS parameters,  $d$  and  $e$ ; i.e., any high order anisotropies ( $p \geq 4$ ) are strictly forbidden. The ZFS of the individual Ni<sup>II</sup> ions, as well as their orientations, are directly measured through EPR studies on an isostructural Zn<sub>3</sub>Ni compound.<sup>13</sup> Due to the restriction of  $S_4$  symmetry, only two independent Heisenberg interaction parameters,  $J_1$  and  $J_2$ , are allowed; these interactions can be determined by dc susceptibility measurements<sup>93</sup>. Therefore, all of the parameters in Equation 3-3 can be determined separately. On the other hand, the molecule possesses  $S_4$  symmetry which prohibits the rhombic anisotropy term in the GSA Hamiltonian. The high symmetry of the molecule is confirmed by single-crystal EPR measurements where exceptionally sharp EPR transitions are observed with a four-fold modulation pattern upon rotating  $H_T$ .<sup>33</sup> This clearly illustrates the presence of high order transverse anisotropy which is responsible for the fast quantum tunneling in the Ni<sub>4</sub> SMM.

### 3.3.2 Quantum Tunneling of Magnetization in Ni<sub>4</sub>

We again discuss the transverse anisotropy in Ni<sub>4</sub> by calculating the QTM gaps. In the studies of Ni<sub>4</sub>, we focus on the  $k = 0, 1 \dots 4$  ground state QTM tunnel splitting, as shown in Figure 3-10 where the  $|\Delta m|$  values associated with these gaps equal to 8, 7... 4, respectively. The simulations were performed with published ZFS parameters  $d = -7.6$  K,  $e = 1.73$  K and  $J_1 = J_2 = -10$  K.<sup>13, 33, 35</sup> Previous EPR studies on Zn<sub>3</sub>Ni reveal that the easy-axis of the local Ni<sup>II</sup> ion is tilted away from the molecule z-axis with  $\theta = 15^\circ$ . In our studies, we let  $\theta$  vary ( $\theta = 15^\circ$  and 0) to illustrate the influence of  $\theta$  on the symmetry of the molecular Hamiltonian.

Figure 3-11 shows the QTM gaps as function of transverse field ( $H_T$ ) via exact diagonalization of Equation 3-3. As shown in the figure,  $\Delta_{k=0}$  and  $\Delta_{k=4}$  retain non-zero values in the absence of a transverse field, while all other tunnel splittings vanish at  $H_T = 0$ . Such a result is of no surprises based on the  $S_4$  molecular symmetry where only QTM between states with

$|\Delta m| = 4n$  ( $n$  is an integer) are allowed. However, unlike the  $\text{Mn}_3$  SMM, the QTM selection rules corresponding to the  $\theta = 15^\circ$  and  $0$  situations are exactly the same. In both scenarios only the  $\Delta_{k=0}$  ( $|\Delta m| = 8$ ) and  $\Delta_{k=4}$  ( $|\Delta m| = 4$ ) are non-zero, while the other  $k$ -even QTM gap, e.g.,  $\Delta_{k=2}$  ( $|\Delta m| = 6$ ), always vanishes when  $H_T = 0$ . These simulation results imply that  $\theta$  does not affect the symmetry of the Hamiltonian, which is different from the results we obtained for the  $\text{Mn}_3$  SMM. This can be explained by the difference between the symmetry operations associated with even- and odd-fold symmetries. In an even-fold system, the molecular  $z$ -axis must be a  $C_2$  axis of the molecule; thus, the parallelism between the local  $C_2$  axes of the individual ions and the molecular  $z$ -axis does not introduce an extra  $C_2$  operation to the Hamiltonian. By contrast, the molecular  $z$ -axis is not a  $C_2$  axis in an odd-fold molecule; therefore, the symmetry of the Hamiltonian can be changed if the local  $z$ -axes are coincident with the molecular  $z$ -axis.

In the preceding discussions of  $\text{Mn}_3$ , the spin selection rules can be simply understood in terms of the rotational symmetry of a molecule ( $C_6$  or  $C_3$ ). For the  $\text{Ni}_4$  SMM, due to the fast tunneling at  $k = 0$ , only the  $k = 0$  QTM step was observed in experiments. Nevertheless, it is useful to examine the selection rules for  $\text{Ni}_4$  since they should be generally applicable to SMMs with the same symmetry. However, the QTM spin selection rules in the  $\text{Ni}_4$  SMM cannot be fully accounted by the  $S_4$  molecular symmetry; one must additionally consider the intrinsic  $C_i$  symmetry of the spin Hamiltonian must be considered. Upon application of a magnetic field parallel to the molecular  $z$ -axis, the  $S_4$  symmetry group reduces to  $C_2$ , in which the  $\Delta_{k=2}$  tunnel splitting is allowed. This clearly contradicts to our simulation which shows that the spin Hamiltonian possesses a higher symmetry. When considering the  $C_i$  symmetry, the consequential zero-field spin Hamiltonian possesses  $S_4 \times C_i = C_{4h}$  symmetry, which corresponds to the symmetry of the  $B_4^4 \hat{O}_4^4$  interaction, as shown by Figure 1-4(d) in Chapter 1. In the presence of a

longitudinal field, the  $C_{4h}$  group reduces to the  $C_4$  group in which the QTM selection rule is that  $|\Delta m|$  equals to multiples of 4. We would like to remind that the  $C_i$  symmetry is guaranteed by the nature of the spin-orbit interaction which is not limited to spin Hamiltonians, i.e., for any Hamiltonian determined by crystal field and/or spin-orbital coupling, the  $C_i$  symmetry should be applied regardless of whether the orbital angular momentum is quenched or not. Thus, it is always necessary to consider  $C_i$  symmetry in addition to the structural symmetry, especially when improper rotations are involved. Observation of  $k > 0$  QTM steps in  $Ni_4$  is not practical due to the extremely fast tunneling at  $k = 0$ . We note that the  $k = 0$  tunneling could be greatly suppressed if the ground spin state of the molecule was increased, e.g., if the molecule is constituted by four  $s = 2$  ions. Then it would be possible to study the  $k > 0$  QTM steps.

The BPI pattern of the  $\Delta_{k=0}$  tunnel splitting is shown in Figure 3-12 which is simulated employing Equation 3-3. The simulation was performed with the inclusion of a  $15^\circ$  angle between the local easy-axes of  $Ni^{II}$  ions and the molecular  $z$ -axis. As shown in the figure, the  $\Delta_{k=0}$  tunnel splitting exhibits four-fold modulation pattern, with  $H_L = 0$  (exactly). Such a result can be reinforced based on considering the symmetry of the Hamiltonian: with the inclusion of  $C_i$  symmetry, the resultant zero-field Hamiltonian has  $C_{4h}$  symmetry with the  $xy$ -plane being a mirror plane; thus, the molecular hard-plane must lie exactly in the  $xy$ -plane and the  $k = 0$  QTM gap should locate at  $H_L = 0$ .

Finally, we discuss the influences of disorder on the QTM steps in  $Ni_4$ . In the presence of random crystallography defects, the symmetry of the molecules is expected to be lowered, leading to the absence of spin QTM selection rules. Figure 3-13 was generated by considering the orientation of the ZFS tensor of one of the  $Ni^{II}$  ions in the molecule to be slightly different, i.e., the ZFS tensors of three  $Ni$  ions are tilted  $15^\circ$  from the molecular  $z$ -axis, while one is tilted

10° from the molecular  $z$ -axis. As shown in the figure, all resonances possess a non-zero tunneling gap at zero  $H_T$ . The inset of the figure plots the  $k = 1, 2$  and  $3$  gaps in the log-log scale, which clearly indicates that these tunneling gaps, which are forbidden in the  $S_4$  symmetry, also saturate at a non-zero value when  $H_T$  tends to zero. These results show that a small disorder can effectively unfreeze all QTM steps without the assistance of a transverse field. This argument can be reinforced by group theoretic considerations. With random disorder, the symmetry of a molecule is lowered to  $C_1$ , where the spin Hamiltonian only possesses  $C_i$  symmetry. Upon applying a longitudinal field, the  $C_i$  group reduces to the  $C_1$  group, where all the states necessarily belong to the same one-dimensional irreducible representation.<sup>95</sup> Therefore, mixing between any states is allowed. We note that this kind of disorder can be introduced by small crystallographic defects, which always exist in real samples. The preceding discussion shows that disorder may be responsible for the observations of  $k$ -odd QTM steps in SMMs with even-fold symmetries.

### 3.4 Summary

In this chapter, we discussed QTM in a  $Mn_3$  SMM with exact  $C_3$  symmetry. We discovered the origin of the  $\hat{O}_4^3$  operator in the GSA Hamiltonian by mapping the spectrum obtained via the MS Hamiltonian onto the GSA model. By investigating the tunnel splittings generated by the  $\hat{O}_4^3$  operator, we found that it unfreezes the  $k$ -odd QTM resonances and shifts the  $k = 0$  resonance away from  $H_L = 0$ . In addition, we discussed QTM in a  $Ni_4$  SMM with  $S_4$  symmetry. We found that the BPI patterns of the  $k = 0$  QTM splittings in the  $Mn_3$  and  $Ni_4$  SMMs behave remarkably different. This comparison shows the uniqueness of  $C_3$  symmetry.

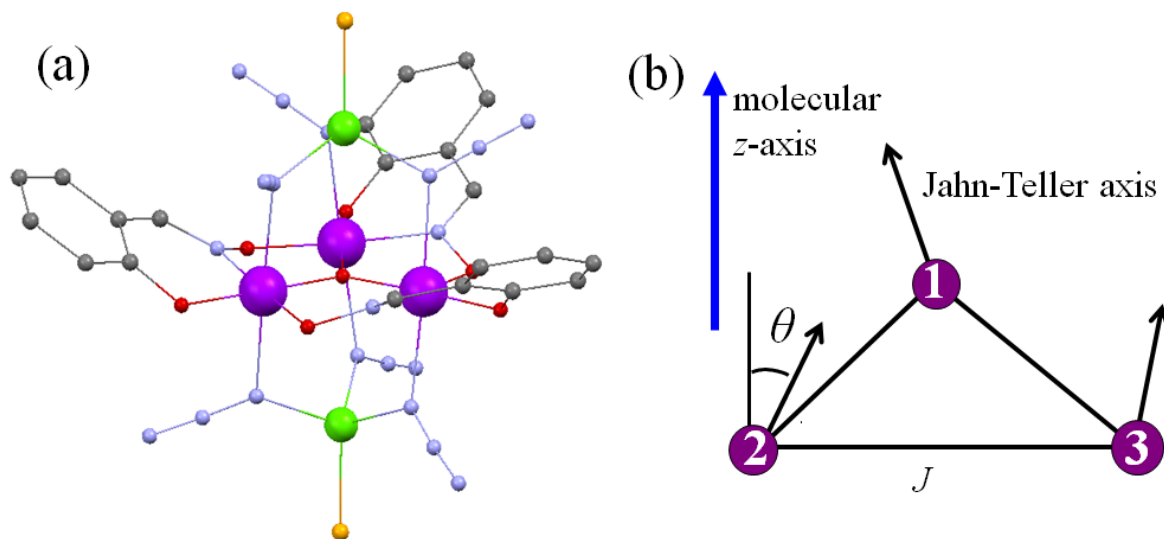


Figure 3-1. The molecular structure and the magnetic core of the Mn<sub>3</sub> SMM. (a) The molecular structure of the Mn<sub>3</sub> SMM. Color code: Mn = purple, Zn = green, O = red, N = blue, C = black and Cl = dark gold. H-atoms have been omitted for clarity. (b) Schematic representation of the magnetic core of the Mn<sub>3</sub> SMM.

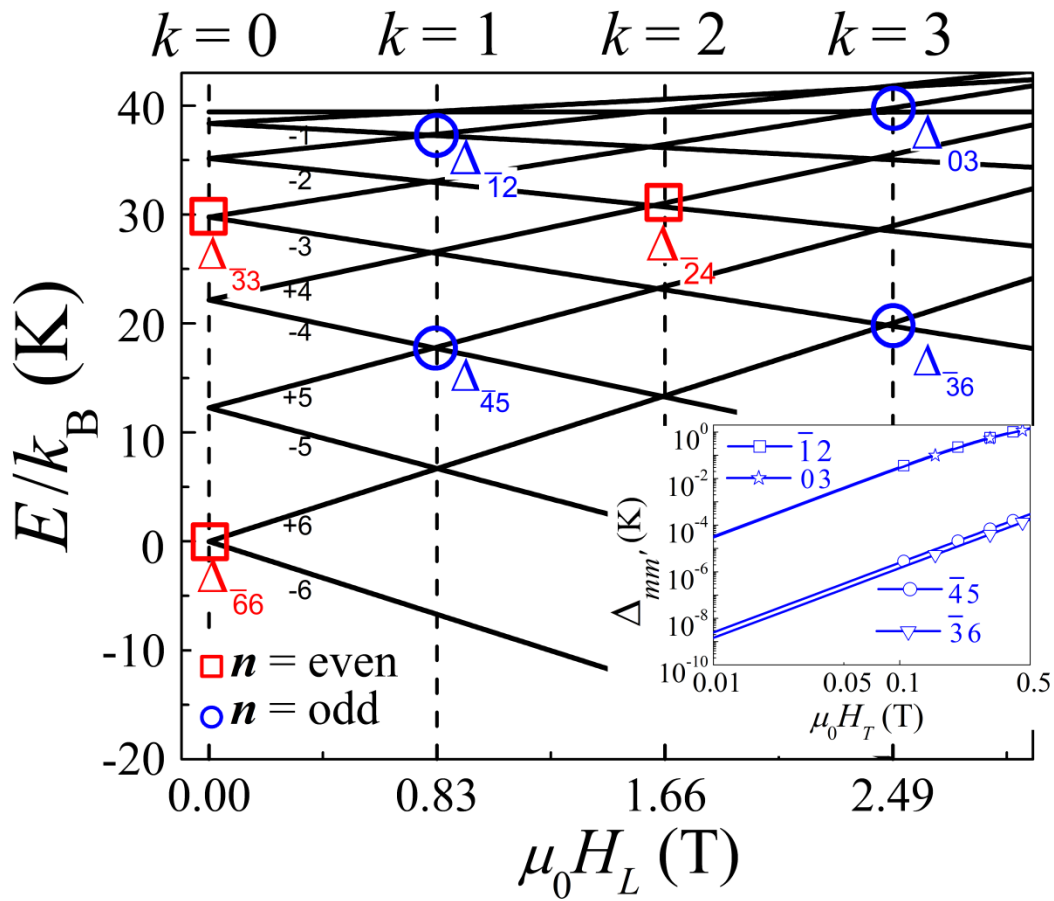


Figure 3-2. Zeeman diagram for a spin  $S = 6$  multiplet with easy-axis anisotropy ( $D < 0$  in Equation 3-1) and  $H//z$ . All possible non-zero tunneling gaps for  $C_3$  symmetry are labeled according to the scheme discussed in the main text. The inset shows the  $H_T$  dependence of the odd- $n$  tunneling gaps.

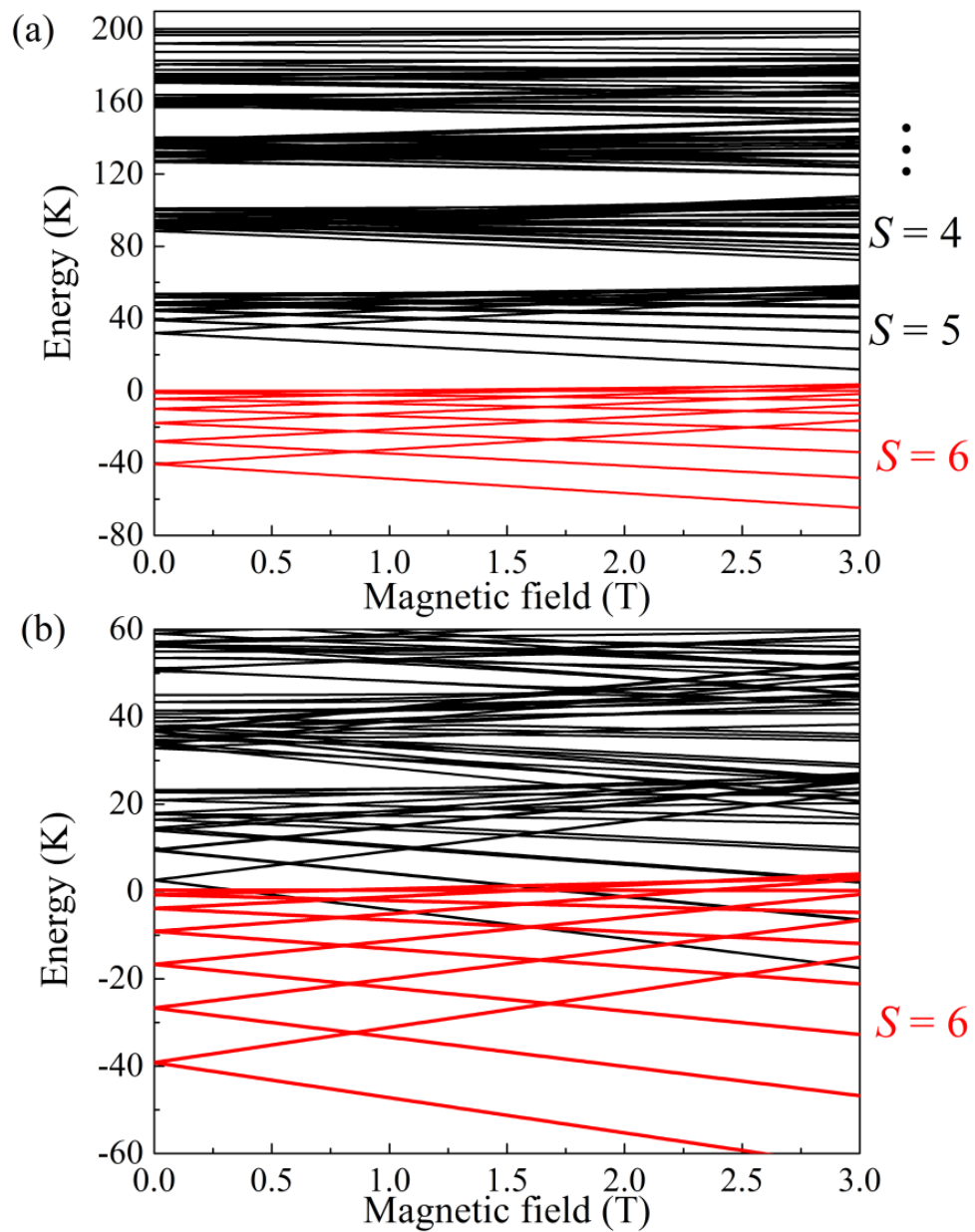


Figure 3-3. Zeeman diagram of  $Mn_3$  generated by Equation 3-2 with different magnitudes of  $J$ . The diagrams are generated with (a)  $J = -10$  K and (b)  $J = -4.88$  K. As shown in (b), when  $J = -4.88$  K, the excited spin multiplets overlap with the ground state at low fields.

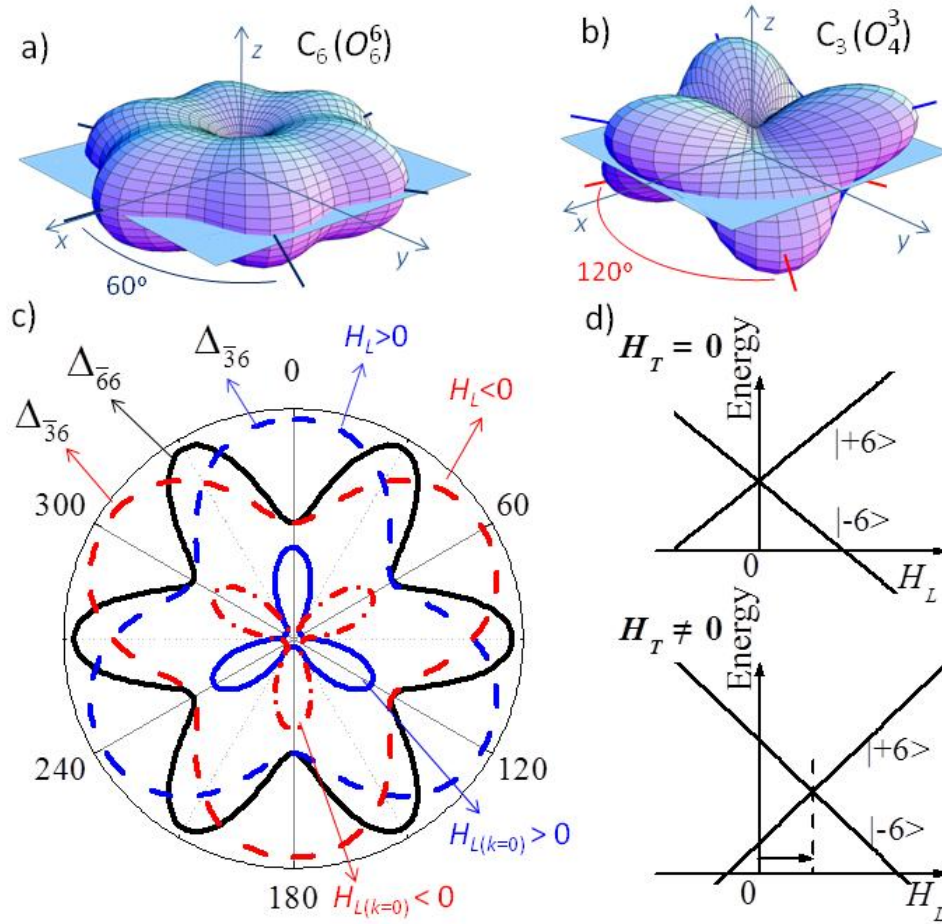


Figure 3-4. The symmetries of the ZFS interactions and the tunnel splittings. (a) and (b) illustrate the potential energy surfaces corresponding to the  $\hat{O}_6^6$  and  $\hat{O}_4^3$  GSA operator equivalents with the presence of a negative axial anisotropy ( $DS_z^2, (D < 0)$ ), respectively. (c)  $k = 0$  (solid curve) and  $k = 3$  (dashed curves) ground state tunneling gaps as a function of the orientation of  $H_T (= 0.2 \text{ T})$  within the  $xy$ -plane, calculated using Eqn. (1) with  $B_6^6 = 0$ . The data have been normalized and offset to aid viewing:  $\Delta_{\bar{3}6}$  oscillates from  $3.65$  to  $3.90 \times 10^{-6} \text{ K}$  ( $\sim 6\%$ ) and  $\Delta_{\bar{6}6}$  from  $4.065$  to  $4.074 \times 10^{-9} \text{ K}$  ( $\sim 0.2\%$ ). The inner curves correspond to the  $H_L$  field (dotted  $\Rightarrow H_L > 0$ , dash-dotted  $\Rightarrow H_L < 0$ ) needed to compensate for the shift of the  $k = 0$  resonance upon application of  $H_T$  as illustrated in (d): for  $H_T = 0.2 \text{ T}$ ,  $H_L$  oscillates about zero with an amplitude of  $6.3 \times 10^{-7} \text{ T}$  and a three-fold ( $S_6$ ) periodicity.

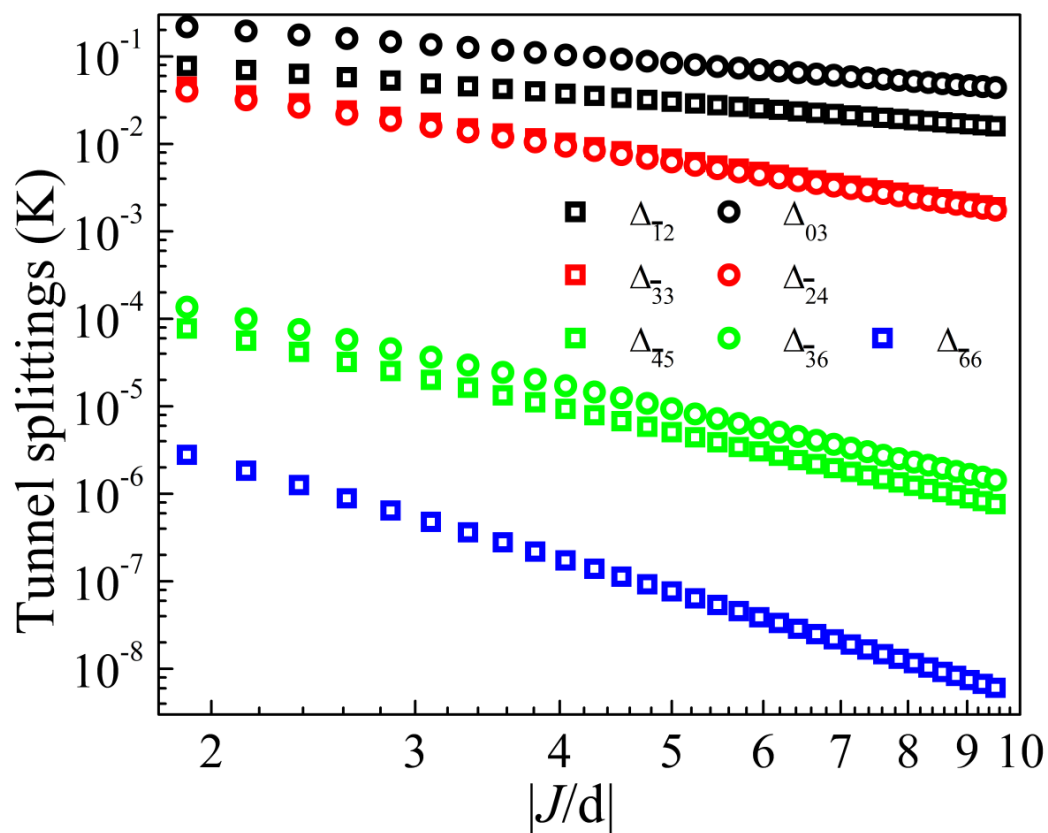


Figure 3-5. Tunnel splittings of the  $\text{Mn}_3$  SMM as a function of the coupling constant  $J$ . Simulations are performed with the JT-axes tilted  $8.5^\circ$  away from the molecule z-axis. The splittings associated with same  $|\Delta m_s|$  value are rendered in the same color. Note the results are plotted on a logarithmic scale.

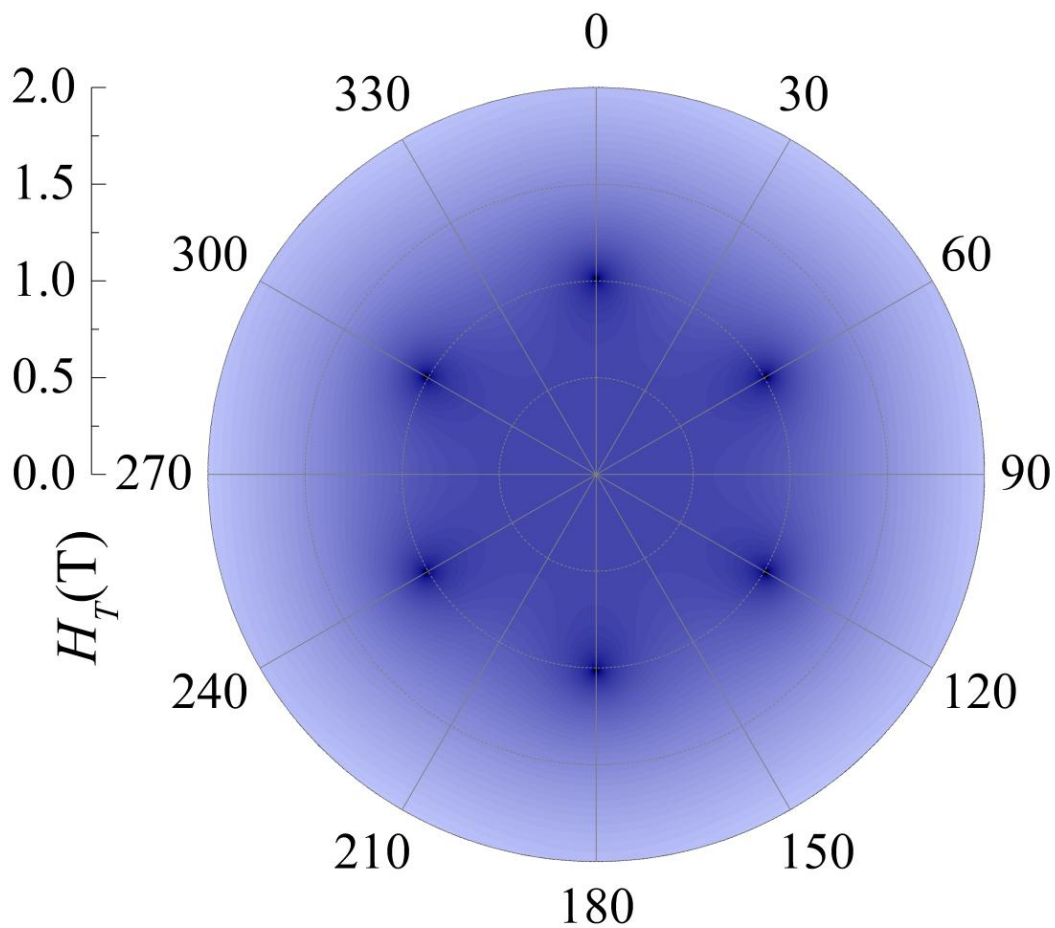


Figure 3-6. Color contour polar plot of the ground state  $\Delta_{\bar{6}_6}$  gap as a function of  $H_T$ , calculated using Equation 3-1 with  $B_4^3 = 0$ . The BPI exhibits a six-fold modulation pattern with the gap located exactly in the molecular  $xy$ -plane ( $H_L = 0$ ).

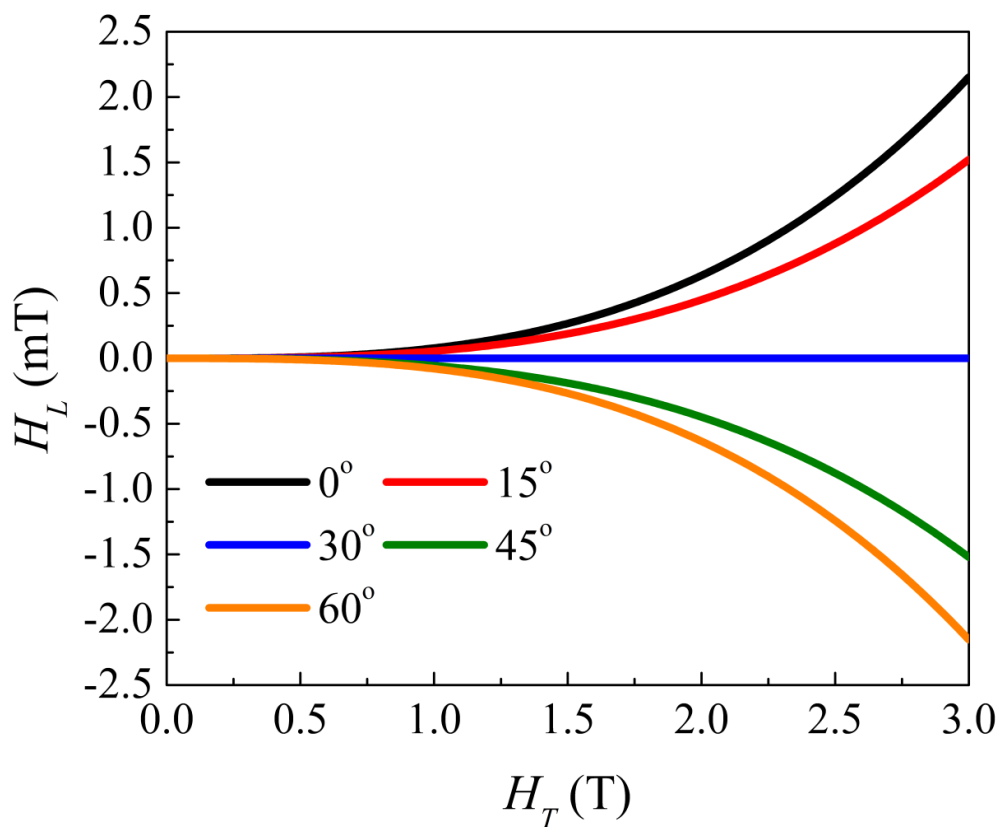


Figure 3-7. Shift of  $H_L$  for  $\Delta_{\bar{6}6}$  as a function of the magnitudes of the applied  $H_T$ . Note that the slopes of each curve is not a constant (except  $30^\circ$ , where  $H_L = 0$ ), which indicates that the orientation of the molecular hard plane, which corresponds to  $H_L/H_T$ , depends on the magnitude of  $H_T$ .

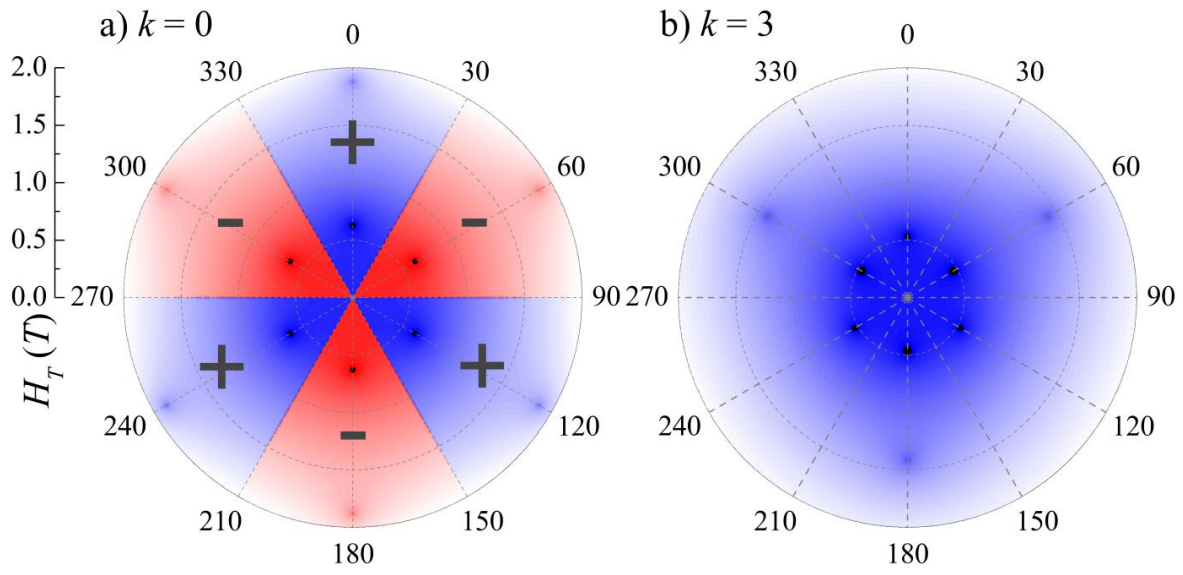


Figure 3-8. The BPI patterns for the ground QTM resonances of the  $\text{Mn}_3$  SMM. The Color contour plots show  $\Delta_{\bar{6}6}$  (a) and  $\Delta_{\bar{3}6}$  (b) as a function of  $H_T$ , calculated using Equation 3-1 with  $B_6^6 = 0$ . A compensating  $H_L$  field was required in (a) that alternates between positive (red) and negative (blue) values. Both figures display BPI minima (dark spots) that exhibit three-fold symmetry when the variation of  $H_L$  is also taken into account.

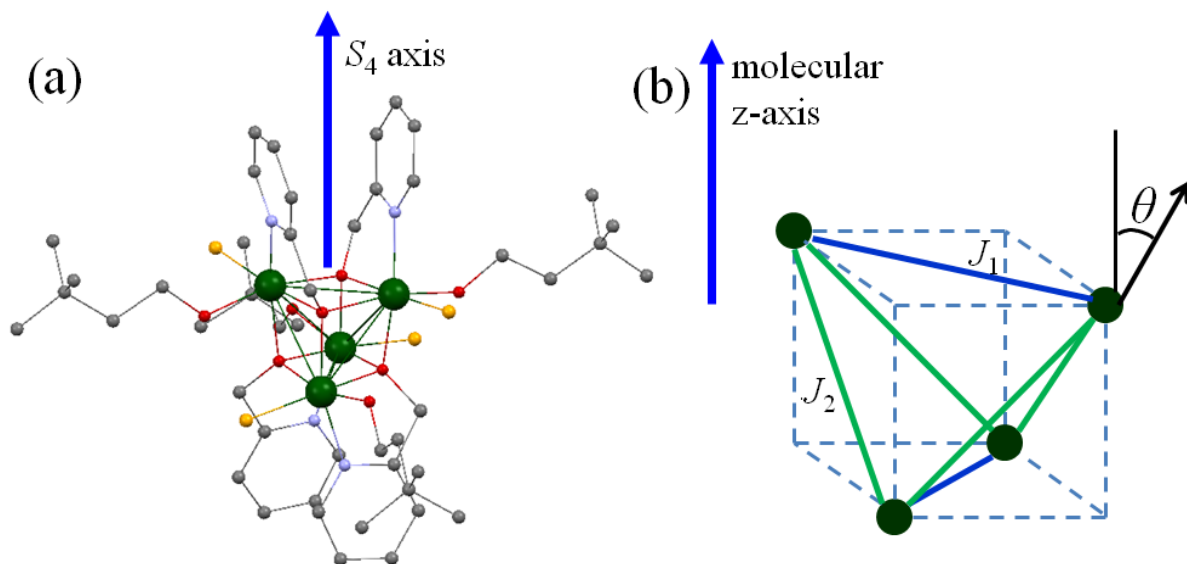


Figure 3-9. The structure and the magnetic core of the Ni<sub>4</sub> SMM. (a) The molecular structure of the Ni<sub>4</sub> SMM. Color code: Ni = olive, O = red, N = blue, C = black and Cl = dark gold. H-atoms have been omitted for clarity. (b) Schematic representation of the magnetic core of the Ni<sub>4</sub> SMM.

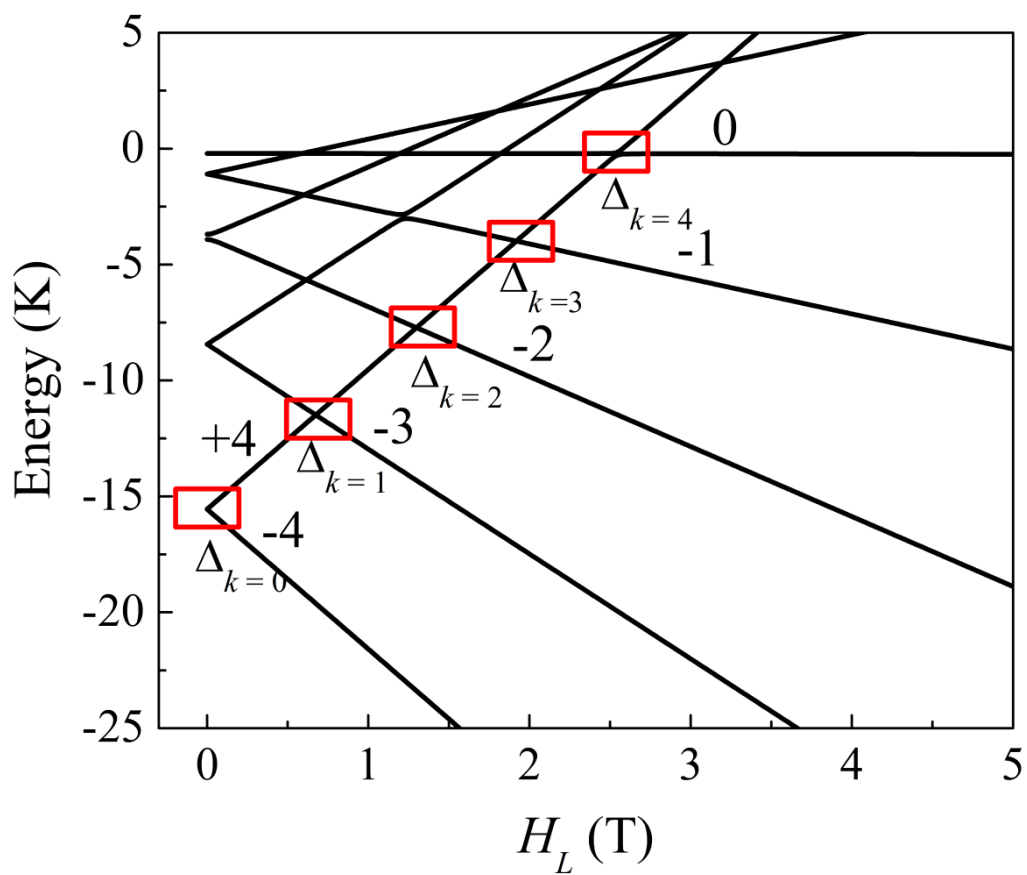


Figure 3-10. Zeeman diagram for the Ni<sub>4</sub> SMM simulated employing Equation 3-3. Only the ground state  $S = 4$  multiplet is shown in the figure. The  $k = 0$  to 4 ground state QTM splittings are labeled in the figure.

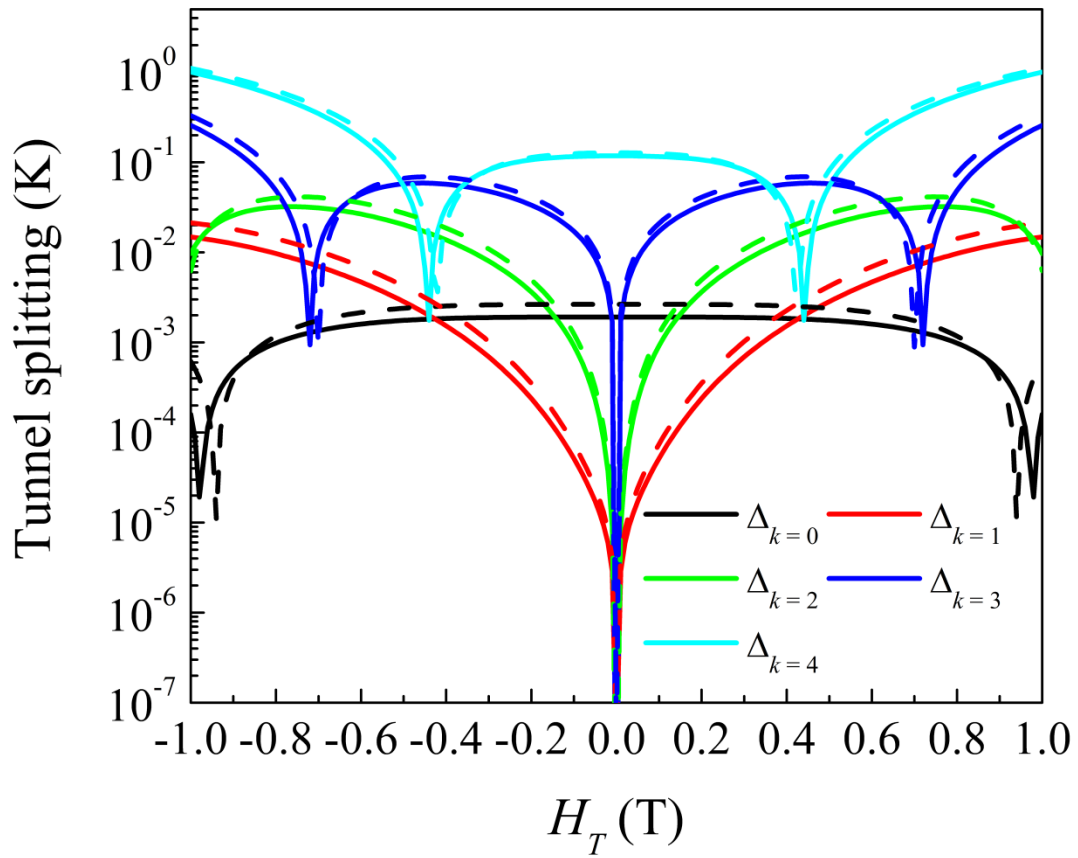


Figure 3-11. The ground state QTM gaps for the  $\text{Ni}_4$  SMM as a function of  $H_T$ . The simulations were performed employing Equation 3-3 with the parameters given in the main text. The solid lines were generated with  $\theta = 0$  and the dash lines were generated with  $\theta = 15^\circ$ .

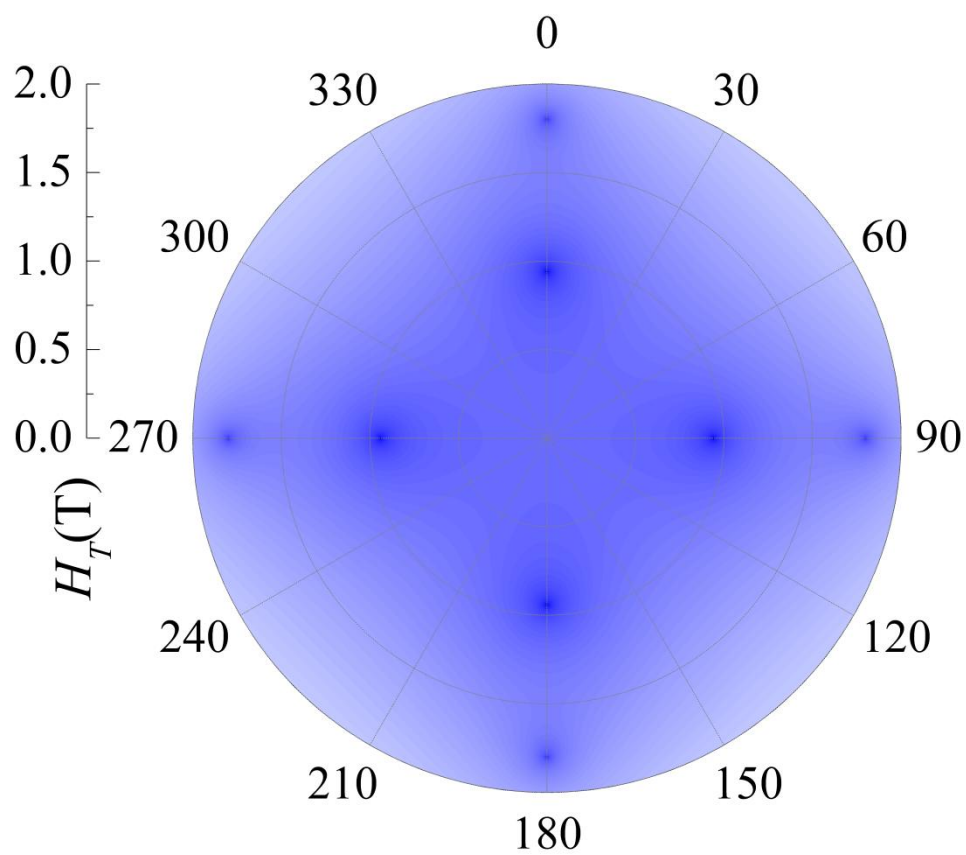


Figure 3-12. Color contour polar plot of the ground  $\Delta_{k=0}$  gap as a function of  $H_T$ , calculated using Equation 3-3 with the parameters given in the main text. The BPI exhibits four-fold modulation pattern with the  $\Delta_{k=0}$  gap located exactly in the molecular  $xy$ -plane ( $H_L = 0$ ).

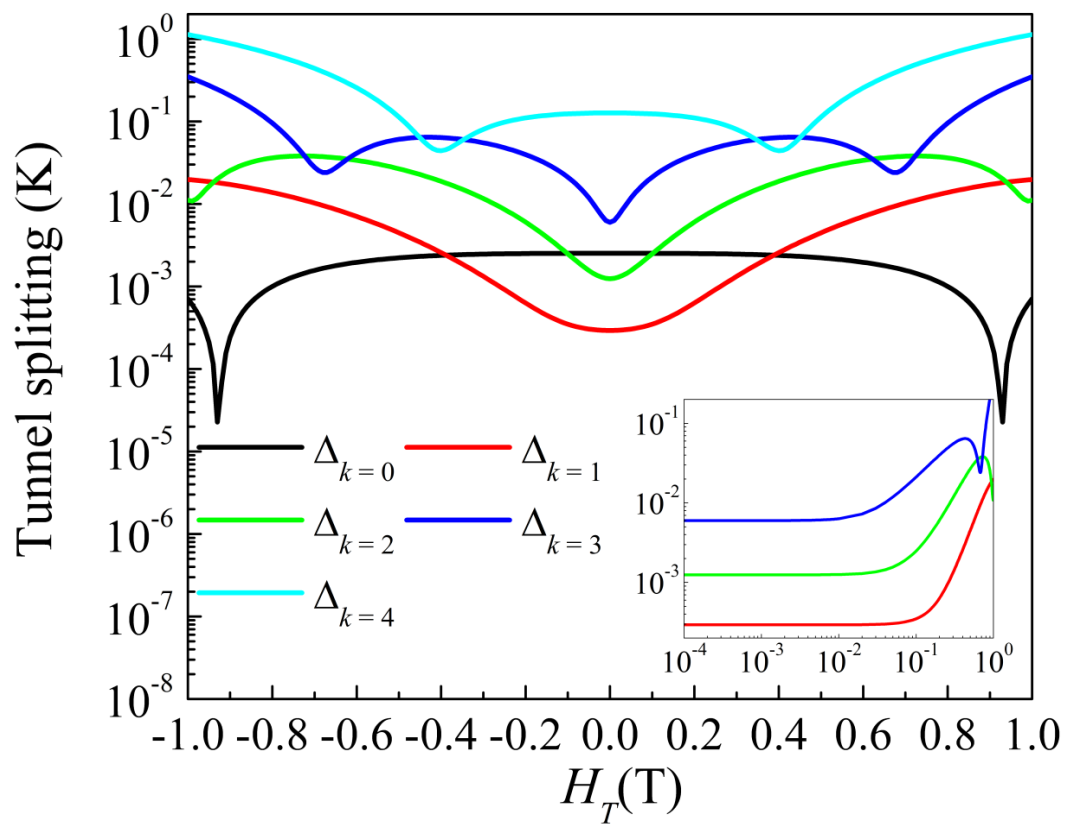


Figure 3-13. The effect of disorder on the ground state QTM gaps for the Ni<sub>4</sub> SMM. The simulations were performed employing Equation 3-3 by considering the orientation of the ZFS tensor of one of the Ni<sup>II</sup> ions in the molecule to be slight different from the others (see details in the main text).

CHAPTER 4  
ELECTRON PARAMAGNETIC RESONANCE AND QUANTUM TUNNELING OF  
MAGNETIZATION STUDIES OF  $Mn_4$  SINGLE-MOLECULE MAGNETS: REVEALING  
COMPETING ZERO-FIELD INTERACTIONS

The work presented in this chapter can be found in the following articles: Liu J.; Beedle C. C.; Quddusi H. M.; del Barco E.; Hendrickson D. N.; Hill S., EPR and magnetic quantum tunneling studies of the mixed valent  $[Mn_4(anca)_4(Hedea)_2(edea)_2] \cdot 2CHCl_3$ , EtOH single-molecule magnet. *Polyhedron* 2011, 30(18), 2965. (reused with permission from Elsevier); Heroux, K. J.; Quddusi, H. M.; Liu, J.; O'Brien, J. R.; Nakano, M.; del Barco, E.; Hill, S.; Hendrickson, D. N., Cationic  $Mn_4$  Single-Molecule Magnet with a Sterically Isolated Core. *Inorg. Chem.* 2011, 50 (16), 7367. (reused with permission from American Chemical Society); Quddusi, H. M.; Liu, J.; Singh, S.; Heroux, K. J.; del Barco, E.; Hill, S.; Hendrickson, D. N., Asymmetric Berry-Phase Interference Patterns in a Single-Molecule Magnet. *Phys. Rev. Lett.* 2011, 106 (22), 227201. (reused with permission from American Physical Society)

### 4.1 Introduction

In the previous chapter we compared the giant-spin approximation (GSA) with the multi-spin (MS) model in a high symmetry ( $C_3$ )  $Mn_3$  single-molecule magnet (SMM) where excellent agreement is achieved. In those studies, we showed that the GSA reproduces all of the important low temperature features of the molecule, including the quantum tunneling of magnetization (QTM) results, which are extremely sensitive to the symmetry of a molecule. However, as we have mentioned in Chapter 1, the GSA model fails when the total spin of the molecule fluctuates.<sup>34, 36</sup> In addition, there are several other scenarios in which the GSA model fails. One of these situations is the case of antiferromagnetically (AF) coupled low symmetry SMMs. Several works on AF coupled low symmetry  $Mn_3$  molecules<sup>101</sup>, as well as studies for the AF coupled dinuclear Mn molecule presented in Chapter 2, suggest that, in those systems, it is

meaningless to analyze experimental results with the GSA model since the ground spin state cannot be rigorously attributed to any  $S$  state. On the other hand, the GSA model seems to be a reasonable approximation in most ferromagnetically (FM) coupled SMMs, even when a molecule possesses very low structural symmetry and/or when the interactions within its magnetic core are weak. In FM coupled compounds, the ground spin state can be estimated by optimizing the total spin of the molecule. Low temperature magnetic measurements, such as reduced magnetization and ac susceptibility, can be understood by considering the second order anisotropies within the GSA. Even more precise spectroscopic measurement results, for instance, single-crystal EPR, can also be interpreted by using the GSA model including consideration of a few high-order anisotropy operators. Still, there are some important properties of FM coupled SMMs which are hard to explain with a GSA. One of them is the low symmetry zero-field magneto anisotropy energy potential of a molecule. For instance, when a SMM possesses only  $C_1$  (or  $C_i$ ) structural symmetry, all possible Stevens operators (up to  $p \leq 2S$ ) should be included if the GSA Hamiltonian is applied. In such situations, it is still possible to interpret experimental results with the GSA model since no spin fluctuations are involved; however, the obtained parameters provide little insight into the physics of the molecule. The magnetic symmetry of a molecule can be probed with QTM measurement, where the Berry-phase interference (BPI) pattern is directly related to the molecular symmetry. Observations of low symmetry BPI patterns are more likely to occur in weakly coupled systems for the following reasons: In the strong interaction limit, where  $|J| \rightarrow \infty$ , high order ( $p \geq 4$ ) anisotropy terms vanish and the resultant GSA Hamiltonian, which includes only the second order anisotropies, possesses  $D_{2h}$  symmetry<sup>35,37</sup>; by contrast, when the interactions are weak, high order anisotropy terms start to emerge so that different BPI patterns can be observed.

In the past several years, our group has studied a family of mixed-valent  $[\text{Mn}_2^{\text{II}}\text{Mn}_2^{\text{III}}]$  SMMs which have similar magnetic cores with various types of ligand.<sup>102-104</sup> Those studies provide important insights into the physics of SMMs having relatively weakly coupled magnetic cores. In this chapter we will discuss electron paramagnetic resonance (EPR) and QTM studies on two similar  $\text{Mn}_4$  SMMs, a)  $[\text{Mn}_4(\text{Bet})_4(\text{mdea})_2(\text{mdeaH})_2](\text{BPh}_4)_4$  SMM<sup>103</sup>, henceforth  $\text{Mn}_4\text{-Bet}$ , where Bet is glycine betaine and mdeaH is N-methyldiethanolamine and b)  $[\text{Mn}_4(\text{anca})_4(\text{Hedea})_2(\text{edea})_2] \cdot 2\text{CHCl}_3 \cdot 2\text{EtOH}$ ,<sup>105</sup> henceforth  $\text{Mn}_4\text{-anca}$ , where anca is the anion of 9-anthracenecarboxylic acid, and Hedea and edea are the mono- and di-anions of N-ethyldiethanolamine, respectively. Extensive EPR and QTM measurements were carried out to determine the magneto anisotropies of these molecules. In this chapter, we will focus on the data collected on  $\text{Mn}_4\text{-Bet}$  where an intriguing motion of the  $k = 1$  BPI minima in the magnitude-direction phase space of the transverse field, as well as an asymmetric BPI pattern with respect to the polarity of the applied transverse field, were observed in QTM studies. We found that these features result from the competition between the zero-field splitting (ZFS) tensors of the inequivalent Mn ions within the magnetic core of the molecule. Both the EPR and QTM experimental results are simulated with a MS Hamiltonian which includes non-collinear ZFS tensors for the different Mn ions. We will also show EPR spectra collected on  $\text{Mn}_4\text{-anca}$ , where very similar magneto anisotropies were observed.

The work presented in this chapter was performed in collaborations with Dr. del Barco's group at the University of Central Florida (UCF) and Dr. Hendrickson's group at the University of California, San Diego (UCSD). The samples were synthesized at UCSD and the high-temperature magnetometry measurements were also performed at UCSD. Low-temperature QTM measurements were performed at UCF. The EPR measurements, as well as the simulations

of both the EPR and QTM results were performed at the NHMFL and form the subject of this chapter.

## 4.2 The Mn<sub>4</sub>-Bet SMM

### 4.2.1 The Structure of the Mn<sub>4</sub>-Bet SMM

The Mn<sub>4</sub>-Bet SMM crystallizes in a triclinic *P*-1 space group with half of the molecule in the asymmetric unit; the other half of the molecule is generated via inversion. The structure of the molecule is shown in Figure 4-1(a). The [Mn<sub>2</sub><sup>II</sup>Mn<sub>2</sub><sup>III</sup>O<sub>6</sub>]<sup>4+</sup> core resembles two face-sharing cubanes missing opposite vertices with two hepta-coordinated Mn<sup>II</sup> ions in the “wing” positions and two hexa-coordinated Mn<sup>III</sup> ions in the “body” positions. Due to the inversion symmetry of the molecule, all four Mn ions lie in the same plane, with the JT-axes of the Mn<sup>III</sup> ions oriented along the Mn<sup>III</sup>-N bonds, which lie about 55 degrees out of the plane. Figure 4-1(c) shows the schematic representation of the molecule illustrating the magnetic interactions within the core. The magnetic ions are labeled in the figure with the 1<sup>st</sup> and 4<sup>th</sup> ions being Mn<sup>II</sup> and the 2<sup>nd</sup> and 3<sup>rd</sup> ions being Mn<sup>III</sup>. As shown in Figure 4-1(c), three independent Heisenberg interaction parameters are included based on the symmetry of the molecule. Fits to dc susceptibility give a ground spin *S* = 9 state for the molecule. Ac susceptibility measurements were carried out at frequencies from 0.1-10 kHz where both temperature- and frequency-dependent out-of-phase signals are observed below 5.2 K with a relaxation barrier of 20.5 K, confirming the complex to be a SMM.<sup>103</sup> The structure of Mn<sub>4</sub>-anca is shown in Figure 4-1(b). The Mn<sub>4</sub>-anca and Mn<sub>4</sub>-Bet molecules possess very similar [Mn<sub>2</sub><sup>II</sup>Mn<sub>2</sub><sup>III</sup>O<sub>6</sub>]<sup>4+</sup> magnetic cores with different structural ligands. The magnetic cores of these two molecules possess the exactly same topology; therefore, they can be characterized with the same spin Hamiltonian with different parameters. However, we note that the Mn<sub>4</sub>-Bet SMM crystallizes without any lattice solvent molecule, while the Mn<sub>4</sub>-anca SMM co-crystallizes with EtOH as a solvent molecule. As will be shown by the EPR

spectra, the presence of solvent molecules introduces significant disorder which leads to a considerable difference in the linewidths of the EPR transitions observed in these two compounds.

The Mn<sub>4</sub>-Bet molecule possesses  $C_i$  symmetry with two types of magnetic ions: two Mn<sup>III</sup> ( $s = 2$ ) and two Mn<sup>II</sup> ( $s = 5/2$ ). The Mn<sup>III</sup> and Mn<sup>II</sup> ions are not related by any symmetry operation since they belong to the same asymmetric unit of the molecule; this implies that the anisotropy tensors of the Mn<sup>III</sup> and Mn<sup>II</sup> ions can be non-collinear. In addition, dc susceptibility measurements suggest relatively weak interactions within the magnetic core which lead to considerable high order anisotropy terms in the GSA.<sup>103</sup> Such high order anisotropies are confirmed by EPR measurements where non-even peak spacing is observed (see more details in data discussion). Therefore, in order to gain suitable insights into the underlying physics, we introduced the following MS Hamiltonian to explain the experimental results:

$$\hat{H} = \sum_{i=1}^4 (\hat{s}_i \cdot \vec{R}_i^T \cdot \vec{d}_i \cdot \vec{R}_i \cdot \hat{s}_i - g\mu_B \vec{B} \cdot \hat{s}_i) + \sum_{i,j(i>j)} (J_{ij} \hat{s}_i \cdot \hat{s}_j + \frac{\mu_0 (g\mu_B)^2}{4\pi r_{i,j}^3} \hat{s}_i \cdot \vec{\Delta}_{i,j} \cdot \hat{s}_j) \quad (4-1)$$

The first term represents the local anisotropy of the  $i^{\text{th}}$  ion, where  $\vec{d}_i$  is the diagonal 2<sup>nd</sup> order ZFS tensors associated with the  $i^{\text{th}}$  ion, with components  $d_{i,xx} = e_i$ ,  $d_{i,yy} = -e_i$  and  $d_{i,zz} = d_i$ ; and the  $\vec{R}_i$  represent Euler rotation matrices defined by the Euler angles  $\theta_i$ ,  $\varphi_i$  and  $\psi_i$ . Due to the inversion symmetry of the molecule, the parameters are related as follows:  $\vec{d}_1 = \vec{d}_4$ ,  $\vec{d}_2 = \vec{d}_3$ ,  $\vec{R}_1 = \vec{R}_4$  and  $\vec{R}_2 = \vec{R}_3$ . For the sake of simplicity, we choose the molecular coordinate frame to coincide with the local coordinate frames of the Mn<sup>III</sup> ions, i.e.,  $\theta_{2,3} = \varphi_{2,3} = \psi_{2,3} = 0$ . The second term in Equation 4-1 is the Zeeman coupling to the applied field, where we assume an isotropic Landé factor,  $g = 2.00$ . The third term is the Heisenberg interaction term with  $J_{1,2} = J_{3,4} = J_a$ ,  $J_{1,3}$

$= J_{2,4} = J_b$ ,  $J_{2,3} = J_c$  and  $J_{1,4} = 0$ , as shown in Figure 4-1(c). The last term is the dipolar interaction term, where the dipolar interaction matrices,  $\vec{\Delta}_{i,j}$ , have been chosen to exactly reproduce the dipolar interaction within the magnetic core based on structural information; the  $r_{i,j}$  represent the distances between the  $i^{\text{th}}$  and  $j^{\text{th}}$  ions obtained via x-ray crystallography studies where  $r_{1,2} = r_{3,4} = 3.259 \text{ \AA}$ ,  $r_{1,3} = r_{2,4} = 3.341 \text{ \AA}$ ,  $r_{1,4} = 5.793 \text{ \AA}$  and  $r_{2,3} = 3.161 \text{ \AA}$  for the  $\text{Mn}_4\text{-Bet}$  SMM. We ignored dipolar interactions in the preceding chapters. However, as we shall see, we cannot them in  $\text{Mn}_4\text{-Bet}$ . The strength of the dipolar interaction is of the order of 0.1 K in the  $\text{Mn}_4\text{-Bet}$  molecule, which is small compared with the isotropic exchange (Heisenberg) interactions within the molecule. However, the dipolar interactions are anisotropic, which means that they can directly affect the magneto anisotropy of the molecule. In our discussions of the BPI pattern of  $\text{Mn}_4\text{-Bet}$ , we find that the motion of the BPI minima is due to the competition between the ZFS tensors of the  $\text{Mn}^{\text{III}}$  and  $\text{Mn}^{\text{II}}$  ions (*vide infra*). The  $\text{Mn}^{\text{II}}$  ion possesses a half-filled shell ( $3d^5$ ,  $s = 5/2$ ), where the ground-state electron configuration has spherical symmetry; therefore, the ZFS of the  $\text{Mn}^{\text{II}}$  ion only arises from higher-order mixing of excited spin states, which is generally very weak.<sup>106</sup> In fact, the largest  $d(\text{Mn}^{\text{II}})$  value for  $\text{Mn}^{\text{II}}$  we have found in literatures is  $1.4 \text{ K}^{82, 107}$ , with values of order 0.1 K more typical, the effect of the dipolar interactions is likely non-negligible compared to that of the ZFS of the  $\text{Mn}^{\text{II}}$  ions. In Chapter 2 and 3, we focused on molecules composed of  $\text{Mn}^{\text{III}}$  ions or  $\text{Ni}^{\text{II}}$  ions, where each ion possesses a much stronger anisotropy itself; thus, dipolar interactions were justifiably ignored.

The  $\text{Mn}_4\text{-Bet}$  SMM is an ideal candidate for single-crystal EPR and QTM studies: the crystal contains no lattice solvent molecules, which removes a major source of disorder.<sup>94</sup> Furthermore, there is no apparent disorder associated with the ligands and only one molecule per unit cell, i.e., only one molecular orientation, which greatly simplifies single-crystal data analysis.

## 4.2.2 Discussion of Electron Paramagnetic Resonance Results

Single-crystal EPR measurements were conducted in a transmission type spectrometer that enabled in-situ rotation of the sample about a fixed axis. Variable frequency (50 - 360 GHz) and variable temperature measurements were thus performed with the field aligned both in the hard-plane and at an orientation close to the easy axis.

Figure 4-2 shows the temperature dependence of EPR spectra obtained at 139.5 GHz with the applied field close to the molecular easy axis. Extremely sharp EPR transitions are observed which confirm the high quality of the crystal. Peak assignments can be made on the basis of the temperature dependence of the resonances and their relative spacings. Those resonances belonging to the  $S = 9$  ground state have been labeled in the figure (A resonances, with the subscript denoting the absolute value of the spin projection associated with the level from which the transition was excited). Careful examination of the 20 K spectrum reveals nine successive peaks belonging to the A series, distributed from 1.15 T to ~4.75 T, which is just below the  $g = 2.00$  position for 139.5 GHz. This confirms that the molecule possesses an  $S = 9$  spin ground state. However, it is notable that the spacings between the A series peaks are non-uniform. In particular, the peaks become very closely spaced at low fields, i.e., the spacing between  $A_9$  and  $A_8$  is 0.21 T which is about 1/3 of the spacing between  $A_1$  and  $A_2$  (0.64 T). Additional resonances are observed at elevated temperatures, confirming the existence of many low-lying excited spin ( $S < 9$ ) multiplets. Simulations reveal the presence of many overlapping excited spin states not far above the lowest lying levels associated with the  $S = 9$  ground state ( $m = 9$  and 8), making assignment of the excited state resonances essentially impossible. The existence of the low-lying excited states is consistent with the relatively weak exchange coupling within the magnetic core of the molecule. We note that almost identical spectra have been obtained for a related  $Mn_4$  complex, albeit with slightly enhanced coupling, resulting in a reduced density of

low-lying excited spin states<sup>104</sup>. Thus, comparisons between the spectra obtained for the two complexes provide additional support to the assignments made in Figure 4-2.

Figure 4-3 shows the temperature dependence of EPR spectra obtained at 67.3 GHz, with the field applied in the hard-plane. These spectra further support the assertions made above on the basis of the easy axis measurements. Again, both the transitions from the  $S = 9$  ground state and excited spin state are observed, with the  $A_9$  transition persisting at the lowest temperature. The resonances from the  $S = 9$  state have been labeled according to the same scheme except that now the subscript corresponds to the spin projection onto the high-field quantization axis, which corresponds to the applied field direction. Non-uniform spacings between peaks are also observed in the hard plane spectra, which is likely due to the presence of high-order transverse anisotropy terms and/or the fact that the spectra were not recorded in the true high fields limit. Note that the spectra in Figure 4-3 were collected at a relative low frequency (67.3 GHz); thus, only the  $A_9, A_7...$  transitions are observed while the  $A_8, A_6 ...$  transitions are missing at this frequency. At frequencies above 100 GHz, a complete series of A transitions,  $A_9, A_8, A_7...$ , are observed (see Figure 4-4(b)). The spectra can be understood with the aid of the hard-plane Zeeman diagram for the ground  $S = 9$  multiplet, as shown in Figure 4-4. The observed high-field EPR transitions are those between adjacent levels, i.e.,  $|\Delta m| = 1$ , where  $m$  is the spin projection onto the direction of the applied field. However, if one follows these levels to low fields, one finds that the transitions from the  $m$ -odd to  $m$ -even states, which correspond to  $A_9, A_7...$  (indicated by the red arrows), decrease to zero as the field tends to zero. By contrast, the transitions from the  $m$ -even to  $m$ -odd states, which correspond to  $A_8, A_6...$  (indicated by the blue arrows), go through a minimum and then tend to a non-zero value as the field tends to zero. Thus,

the  $A_8, A_6...$  transitions cannot be observed below certain frequencies, which is the reason for their absence in the spectra shown in Figure 4-3.

High frequency EPR measurements were also performed on the  $Mn_4$ -anca molecule to determine its spin state and magneto anisotropy. Figure 4-5(a) shows temperature dependence spectra obtained at 165 GHz with the field aligned close to the easy axis. The peaks have been sorted into two series (labeled A and B), based upon their temperature dependence and the relative spacings between peaks within each series. The stronger peaks, which persist to the lowest temperatures, are labeled  $A_9, A_8$ , etc., while the weaker peaks that emerge between the A peaks at higher temperatures are labeled  $B_8, B_7$ , etc. At the lowest temperature, only one strong transition is observed ( $A_9$ ), indicating a reasonably well separated ground state. Looking more closely to the high temperature spectrum at 15 K, one can clearly see nine successive peaks belonging to the A series, distributed from  $\sim 1.8$  T all the way to just below 5.9 T, which is the  $g = 2.00$  position for 165 GHz. These nine peaks are labeled according to the exact same scheme which is used to label the transitions observed in Figure 4-2. These spectra confirm that the approximate ground state spin value is  $S = 9$ . It is also notable that the spacings between the A series peaks are non-uniform. In particular, the peaks become very closely bunched at low fields, i.e., the spacing between  $A_9$  and  $A_8$  is 0.16 T which is less than 1/4 of the spacing between  $A_1$  and  $A_2$  (0.75T). Figure 4-5(b) shows the temperature dependence of EPR spectra obtained at 50.5 GHz, with the field applied in the hard-plane. These spectra further support the assertions made above on the basis of the easy axis measurements. Again, both the A and B series of peaks are observed, with the A series persisting to lower temperatures. In addition, all but one of the peaks ( $A_9$ , with the subscript referring to the  $m$  projection onto the applied field axis) vanish at

the lowest temperature. The B series of resonances behave exactly like another set of hard plane peaks with  $S = 8$  and different ZFS parameters.

We can compare the spectra collected on the Mn<sub>4</sub>-Bet molecule with the spectra collected on the Mn<sub>4</sub>-anca molecule. These spectra support that both compounds possess an  $S = 9$  ground states. Actually, the ZFS associated with the ground state easy-axis transitions ( $A_9$ ) for the both compounds is approximately equal to 110 GHz, which indicates that the Mn<sub>4</sub>-Bet and Mn<sub>4</sub>-anca SMMs have similar axial anisotropy. However, one can find a significant difference between the linewidths of the observed EPR transitions of these two compounds. The linewidth of the easy-axis ground transition ( $\sim 0.02$  T) observed in the Mn<sub>4</sub>-Bet SMM less than 1/5 of that of Mn<sub>4</sub>-anca ( $\sim 0.1$  T). The difference is most likely due to the fact that that Mn<sub>4</sub>-Bet does not have any lattice solvent molecules; therefore, this removes a major source of disorder.

We focus the rest of this chapter on analyzing the EPR and QTM data collected on the Mn<sub>4</sub>-Bet SMM, where extensive QTM measurements were performed to probe its BPI properties. Figure 4-6 shows the frequency dependence of the A resonance peak positions obtained with the field (a) approximately parallel (within a few degrees of misalignment) to the molecular easy axis at 3 K, and (b) in the hard-plane at 5 K. The solid lines in the figure represent simulations of the EPR transitions within the  $S = 9$  ground state; they have been color coded to denote the associated transitions. For some frequencies in the easy-axis data, many resonances are observed because the measurements were performed at an elevated temperature (20 K). The simulations were performed employing Equation 4-1 with the following parameters:  $d_2 = d_3 = -4.99$  K and  $e_2 = e_3 = 0.82$  K;  $d_1 = d_4 = -0.67$  K and  $e_1 = e_4 = 0$ , with the axes of the Mn<sup>II</sup> ions rotated with respect to the central spin by identical Euler angles  $\theta_1 = \theta_4 = 45^\circ$ ,  $\varphi_1 = \varphi_4 = 0$  and  $\psi_1 = \psi_4 = 0$ , as required by the inversion symmetry of the molecule; finally, the Heisenberg interaction

parameters  $J_a = -3.84$  K,  $J_b = -1.20$  K and  $J_c = -3.36$  K were used. It should be emphasized that these parameters were constrained by simulating both the EPR and QTM results simultaneously, which is the reason why non-zero  $d_1$ ,  $d_4$ ,  $\theta_1$  and  $\theta_4$  were obtained (*vide infra*). The parameters are constrained by the best simulations of the A series of EPR peaks in both easy-axis and hard-plane orientations simultaneously. As shown in Figure 4-6, the simulations are in excellent agreement with all of the ground state EPR transitions. The obtained anisotropy values for the  $\text{Mn}^{\text{III}}$  ions are very similar to related  $\text{Mn}^{\text{III}}$  complexes<sup>16, 37, 91, 101, 104</sup>, while the  $d_{1,3}$  value lies within the bounds reported for other  $\text{Mn}^{\text{II}}$  systems<sup>82, 107</sup>.

There are several important features about these parameters that should be pointed at this stage. First, the inclusion of a small non-collinear ZFS parameter for the  $\text{Mn}^{\text{II}}$  ions ( $d_1 = d_4 = -0.67$  K and  $\theta_1 = \theta_4 = 45^\circ$ ) is necessary for the subsequent discussions about the motion of the BPI minima observed in QTM studies. This motion is caused by the competition between the ZFS anisotropies of the  $\text{Mn}^{\text{III}}$  ions and  $\text{Mn}^{\text{II}}$  ions. Due to the inversion symmetry of the molecule, the ZFS tensors of the two  $\text{Mn}^{\text{III}}$  ions must be collinear. If the  $\text{Mn}^{\text{II}}$  ions are isotropic,  $d_1 = d_4 = 0$ , in this case, there cannot be any competition between the magneto anisotropies of the ions within the molecule; hence, no motion of the BPI minima should be observed. For the same reason, the ZFS tensors of the  $\text{Mn}^{\text{II}}$  ions must be non-collinear with those of the  $\text{Mn}^{\text{III}}$  ions ( $\theta_1 = \theta_4 = 45^\circ$ ). Otherwise, the anisotropies of the individual ions would simply add together, and the resultant Hamiltonian would possess a high symmetry such as  $D_{2h}$ . Second, we note that the anisotropy of the  $\text{Mn}^{\text{II}}$  ions is weak (-0.67 K), which indicates that the effect of dipolar interactions is not negligible. The dipolar interactions cause a non-trivial effect and contribute 10% to the motion of the BPI minima, as will be shown later in this chapter. Finally, we need to point out that the obtained parameters are not necessarily unique; it may be possible to model the molecule with

another set of parameters. Nevertheless, these parameters have caught all of the important physics in this Mn<sub>4</sub>-Bet SMM and give excellent quantitative agreement between the experimental results and simulations.

#### 4.2.3 Discussion of Quantum Tunneling of Magnetization Results

QTM experiments were carried out by Dr. del Barco's group at UCF. A high-sensitivity micro-Hall effect magnetometer, a <sup>3</sup>He/<sup>4</sup>He dilution fridge and a 3D vector superconducting magnet were employed to record magnetization hysteresis curves as a function of a longitudinal magnetic field ( $H_L$ ) applied parallel to the easy axis of the molecules, in the temperature range 35-1200 mK. The results are shown in Figure 4-7, where extremely sharp QTM resonances ( $k = 0, 1, \text{ and } 2$ ), spaced by  $\Delta H_L \approx 0.21 \text{ T}$ , confirm the high quality of the crystal. Within the GSA, this spacing corresponds to an axial ZFS parameter,  $D = -0.28 \text{ K}$  ( $g = 2.00$ ). The observed blocking temperature, below which open hysteresis loops are observed, and crossover temperature, below which the QTM becomes temperature independent, are  $\sim 1.2$  and  $\sim 0.2 \text{ K}$ , respectively. A transverse field ( $H_T$ ) was subsequently employed in order to study the symmetry of the QTM in resonances  $k = 0$  and  $k = 1$ . Figure 4-8(a) shows the modulation of the QTM probability for resonance  $k = 0$  as a function of  $H_T$  applied along the magnetic hard axis ( $\Phi = 0$ ). The angle  $\Phi$  is defined as the azimuthal angle between the molecular hard axis and the applied transverse field. The QTM probability is defined as  $P_k = (M_f - M_i)/(M_{\text{sat}} - M_i)$  where  $M_i$  and  $M_f$  are the magnetizations before and after the resonance, respectively, and  $M_{\text{sat}}$  is the saturation value. The orientation of the molecular hard-axis, which lies  $\sim 30^\circ$  away from one of the crystal faces, was deduced from the two-fold modulation of  $P_0$  as a function of the orientation of a 0.2 T transverse field within the hard plane<sup>87</sup>, as shown in the inset of Figure 4-8(a). We note that there was a small ( $\sim 3^\circ$ ) misalignment of the field rotation plane during the measurements. The

influence of this slight misalignment is evaluated further below. The results show that the misalignment is not the primary cause of the observed phenomena (*vide infra*).

The  $P_0$  oscillations in Figure 4-8(a) correspond to BPI for the  $k = 0$  resonance, with minima at regularly spaced field values ( $\Delta H_T \approx 0.3$  T). A maximum in  $P_0$  is found at  $H_T = 0$ , as expected for an integer spin value. Within the framework of the GSA, where

$\Delta H_T = 2k_B (2E[E + D])^{1/2} / g\mu_B$ <sup>52</sup>, one would expect the 2<sup>nd</sup> order rhombic anisotropy parameter to be  $|E| = 0.06$  K. Note that the regularly spaced  $k = 0$  BPI minima are invariant under inversion of  $H_T$ ; i.e., they are symmetric with respect to  $H_T = 0$ . Interestingly, this is not the case in resonance  $k = 1$ , for which the behavior of the QTM probability is very different. This can be seen in Figure 4-8(b), which illustrates the dependence of  $P_1$  on  $H_T$  with  $\Phi = 13.5^\circ$  (the angle for which the first BPI minimum at  $H_T = 0.30$  T is the sharpest). In fact, for resonance  $k = 1$ , different BPI minima appear at different field orientations,  $\Phi$ , of the transverse field within the xy (hard) plane of the molecule (see Figure 4-9); i.e., the first minimum ( $H_T = 0.3$  T) appears at  $\Phi = 13.5^\circ$ , while the second ( $H_T = 0.6$  T) occurs at  $\Phi = 6^\circ$ , contrary to what is found for the  $k = 0$  resonance where all  $P_0$  minima are seen most clearly at  $\Phi = 0$ . Such behavior has been predicted theoretically<sup>87, 108</sup>, though never observed experimentally.

Before considering this aspect in detail, we first discuss the asymmetric nature of the BPI oscillation pattern in resonance  $k = 1$ . As seen clearly in Figure 4-8(b), reversal of the longitudinal field,  $H_L$ , results in a reflection of the  $P_1$  BPI pattern about  $H_T = 0$ . In other words, the BPI minima are in fact invariant under a full magnetic field inversion, as required on the basis of the time-reversal invariance of the spin-orbit Hamiltonian responsible for this physics. As noted above, the symmetries of BPI patterns must respect the symmetry of the zero-field spin Hamiltonian. If one considers only 2<sup>nd</sup>-order ZFS within the GSA, as we discussed in Chapter 1,

then the resulting Hamiltonian necessarily possesses the following symmetry elements: (i) three mutually orthogonal  $C_2$  rotation axes ( $x$ ,  $y$  and  $z$ ); (ii) three mutually orthogonal mirror planes ( $xy$ ,  $xz$  and  $yz$ ); and (iii) an inversion center. The presence the  $C_2$  axis ( $z$ -axis) guarantees invariance with respect to reversal of  $H_T$ ; i.e., it enforces symmetric BPI patterns, irrespective of whether a longitudinal field is applied ( $k > 0$ ) or not ( $k = 0$ ). On the other hand, the horizontal mirror plane guarantees invariance with respect to reversal of  $H_L$ . As we show below, one must break the  $xy$  mirror symmetry in order to obtain asymmetric BPI patterns with respect to inversion of  $H_L$ . In this case, reversal of  $H_L$  results in different patterns; the time-reversal symmetry then guarantees that these two patterns are mirror images. Nevertheless, no matter how many spatial symmetries are broken, the time-reversal invariance of the spin-orbit interaction guarantees that the BPI minima should be invariant under a full reversal of the applied field, i.e., simultaneous reversal of  $H_L$  and  $H_T$ , as we have confirmed experimentally for the first time.

It is possible to reproduce the essential features of the experiments by introducing 4<sup>th</sup>-order terms into the GSA; the  $xy$  mirror symmetry and  $C_2$  rotational symmetry can then be broken by rotating the coordinate frames of the 2<sup>nd</sup> and 4<sup>th</sup>-order tensors. Interestingly, this approach also reproduces the complex motion of the  $P_1$  minima within the  $H_T$ - $\Phi$  phase-space shown in Figure 4-9. However, a complete GSA analysis for Mn<sub>4</sub>-Bet requires many parameters. The difficulty of using the GSA model lies in the fact that all of the 4<sup>th</sup>-order tensors originate from the same order of perturbation in the MS model<sup>35, 37, 109</sup>; therefore, in a system with no symmetry restrictions, all  $B_4^q \hat{O}_4^q$  ( $q = 0$  to 4) terms need to be equally considered. These parameters, obtained via the GSA approach, provide little insight, while the same physics can be naturally understood within a MS Hamiltonian such as Equation 4-1. Note that the emergence of significant higher-order anisotropy terms within the GSA is a manifestation of mixing of the

ground spin state with excited states, which can only be captured within the MS model. In this context, the  $xy$  mirror symmetry may be trivially broken by rotating (tilting) the ZFS tensors at the two inequivalent magnetic sites in the molecule so that their local  $z$ -axes no longer coincide. This is similar to the case of the  $Mn_3$  SMM discussed in Chapter 3 where the molecular hard-plane is a three-fold corrugated plane.<sup>109</sup> However, in  $Mn_4$ -Bet, due to the low magneto symmetry of the molecule, the exact hard-plane of the molecule is an irregular corrugated plane with inversion symmetry only. This is corroborated by the BPI results, where only  $C_i$  symmetry is observed in QTM measurements.

We simulated the BPI patterns for the  $k = 0$  and  $k = 1$  QTM resonances employing Equation 4-1 with the parameters obtained via EPR studies. As discussed in the previous paragraph, the molecular hard-plane is corrugated, and literally impossible to map out computationally. In addition, similar to what we discussed in Chapter 3, this hard plane is field dependent; therefore, we first found the molecular easy-axis and defined the perpendicular plane as the nominal hard-plane. This exactly reproduces the experimental procedures for the QTM measurements. The orientation of the molecular easy-axis is determined by searching for the direction corresponding to the minimum  $H_L$  associated with the  $k = 1$  step. Figure 4-10(b) plots the locations of BPI minima obtained via diagonalization of Equation 4-1 (solid red symbols). The small misalignment of the experimental field rotation plane has been taken into account in our simulations. The quantitative agreement with experiment is also excellent. The motion of the  $P_1$  minima can be understood as a result of the competition between different anisotropic interactions within the molecule, without a need to invoke unphysical 4<sup>th</sup> and higher-order GSA anisotropies. Importantly, the angular positions ( $\Phi$ ) of the  $k = 1$  minima move with  $H_T$ , while the  $k = 0$  minima remain stationary, as found experimentally (Figure 4-9).

Finally, the MS model perfectly reproduces the  $H_T$  asymmetry of the  $k = 1$  BPI pattern. As seen in Figure 4-10(c), the asymmetry is reversed upon inversion of  $H_L$ , as required by the time-reversal invariance of the anisotropic interactions in Equation 4-1, and observed experimentally (Figure 4-8(b)). As we have shown in the preceding data analysis, the complex behavior of the BPI patterns are interpreted by employing Equation 4-1 with a set of standard parameters. The crucial ingredient is the tilting of the ZFS tensors of the external spins,  $s_1$  and  $s_3$ , relative to the central spins  $s_2$  and  $s_4$ , so that the  $xy$  mirror symmetry is broken. This is illustrated in Figure 4-8(a), where one observes that the classical energy landscape is invariant under full field inversion (blue versus black arrows), while this is not the case when only  $H_T$  is reversed (red versus black arrows). The Euler angle  $\theta_{1,3} = 45^\circ$  results in a significant projection of the relatively weak anisotropy associated with the  $\text{Mn}^{\text{II}}$  ions into the hard ( $xy$ ) plane. This, together with the finite  $e_{2,4}$  parameters and the dipolar interactions, results in competing transverse interactions and to the complexity of the BPI patterns observed in Figure 4-9. We also performed simulations without including any field misalignment. The results show that the misalignment has little influence on the  $k = 0$  BPI; the first and second  $k = 1$  BPI minima are found at  $\Phi = 7.5^\circ$  and  $3^\circ$ , respectively without field misalignment; hence, the misalignment cannot be the major source for the motion of the BPI minima, especially the first  $k = 1$  minimum. We note that the dipolar interaction has a very significant effect on the energy levels of the molecule: the ZFS within the  $S = 9$  multiplet varies by as much as 10% when dipolar interactions are omitted, and the location of the  $k = 1$  QTM step is shifted by  $\sim 0.02$  T.

We conclude by noting that asymmetric BPI patterns have been seen in other centrosymmetric SMMs for which a clear explanation has been lacking.<sup>36, 80, 110, 111</sup> In these previous studies, the asymmetric BPI pattern has been attributed to the anti-symmetric Dzyaloshinski-

Moriya (DM) interaction. However, in the Mn based molecules, DM interactions are expected to be weak; therefore, the effects of DM interactions are always expected to be much smaller than those of the single-ion anisotropies.<sup>80</sup> In our work, we showed that the asymmetric pattern can originate simply from competition between ZFS tensors. The present results may help shed light on the effect that symmetric anisotropic interactions can have in magnetic systems with inversion symmetry, where a net DM interaction is strictly forbidden. The present work clearly demonstrates how studies of simple low nuclearity systems can address fundamental symmetry considerations related to QTM in molecular nanomagnetism.

### 4.3 Summary

In this chapter we presented EPR and QTM studies on a low symmetry Mn<sub>4</sub>-Bet SMM showing asymmetric BPI in QTM measurements. A complex motion of BPI minima within the magnitude-orientation phase space of the transverse field has been observed, which stands as the first experimental evidence for such motion in a SMM. These behaviors are attributed to the competition between the ZFS tensors of inequivalent magnetic ions within the molecule. We explained all experimental results based on the parameters obtained via EPR and QTM measurements. An excellent quantitative agreement between simulations and experiments is achieved.

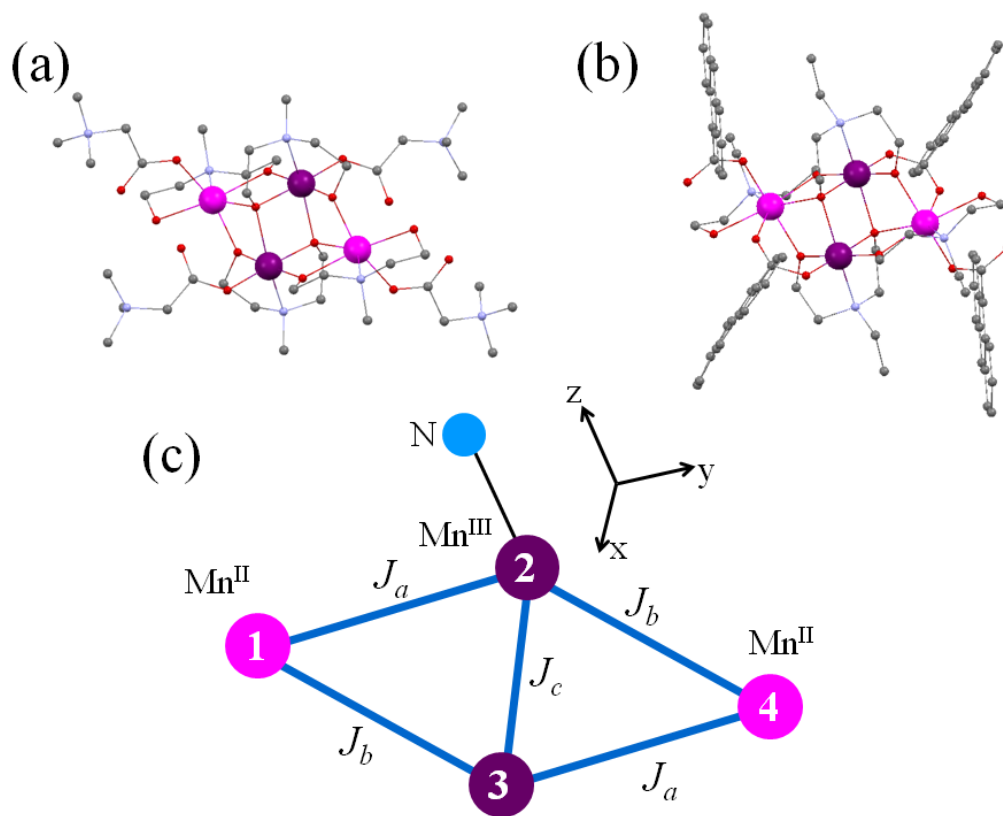


Figure 4-1. The molecular structures and the magnetic cores of the Mn<sub>4</sub> SMMs. (a) The molecular structures of the Mn<sub>4</sub>-Bet SMM. (b) The molecular structures of the Mn<sub>4</sub>-anca SMM. Color code: Mn<sup>III</sup> = purple, Mn<sup>II</sup> = magenta, O = red, N = blue and C = black. H-atoms have been omitted for clarity. (c) Schematic representation of the magnetic core of these Mn<sub>4</sub> SMMs. The z-axis of the molecule is defined by the Mn<sup>III</sup>-N bond, as shown in the figure.

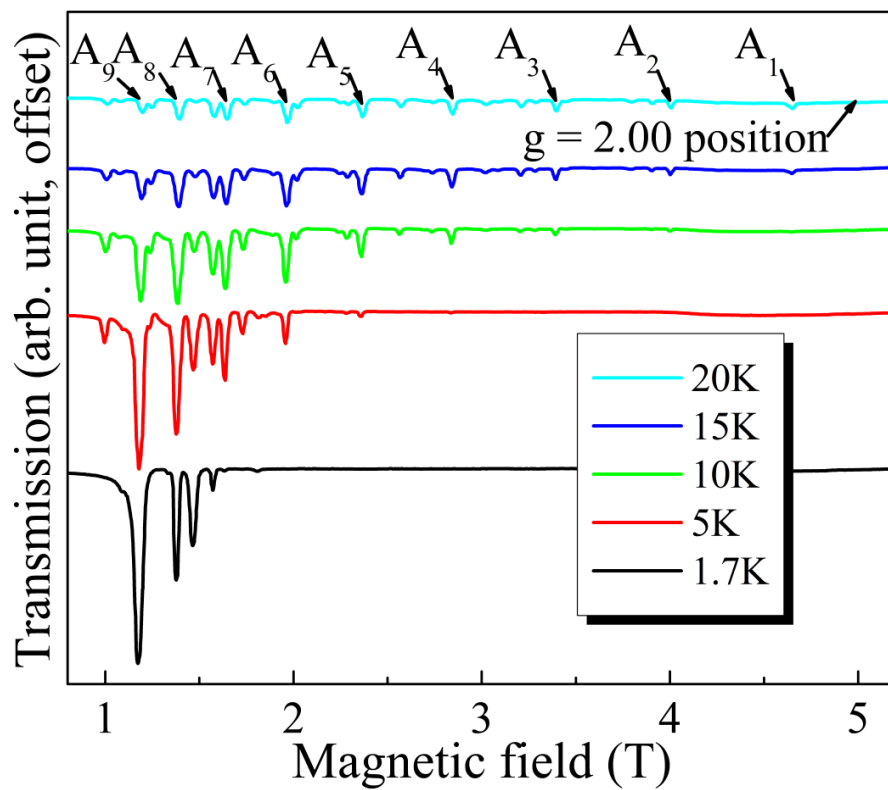


Figure 4-2. Temperature dependent EPR spectra for Mn<sub>4</sub>-Bet obtained at 139.5 GHz with the applied field close to the molecular easy-axis. The peaks A<sub>1</sub>, A<sub>2</sub>...A<sub>9</sub> represent transitions within the S = 9 ground state multiplet.

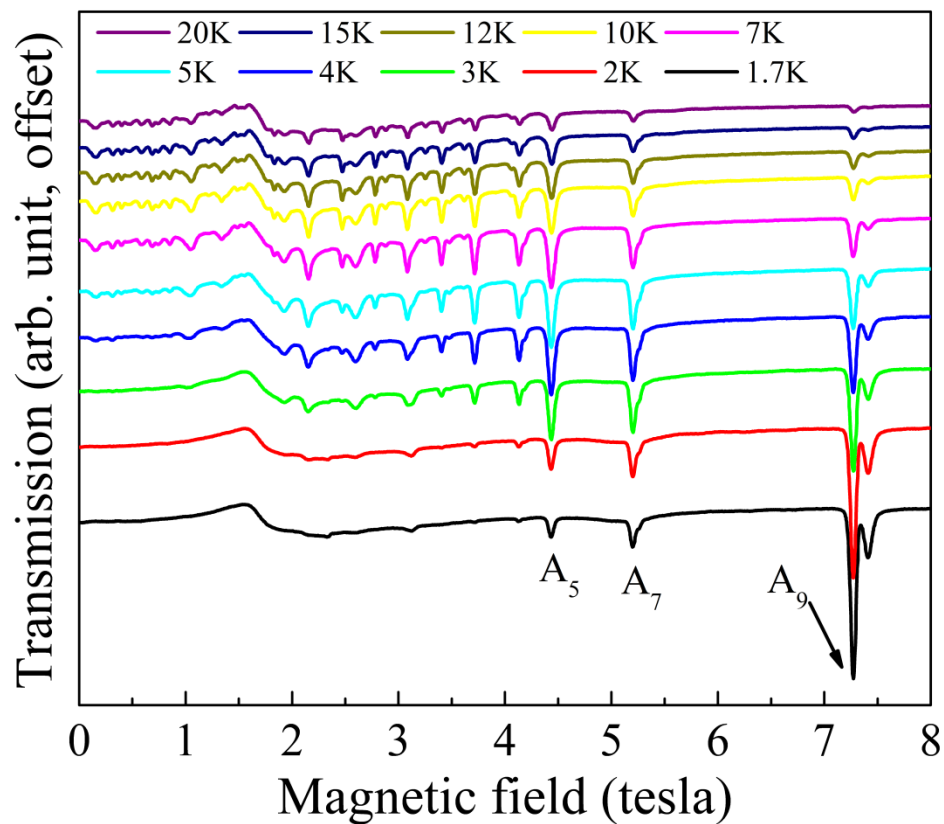


Figure 4-3. Temperature dependent EPR spectra for Mn<sub>4</sub>-Bet obtained at 67.3 GHz with the applied field in the molecular hard-plane. The peaks A<sub>9</sub>, A<sub>7</sub>...A<sub>5</sub> represent transitions within the  $S = 9$  ground state multiplet. Note that the A<sub>8</sub>, A<sub>6</sub>... transitions are not observed at this frequency.

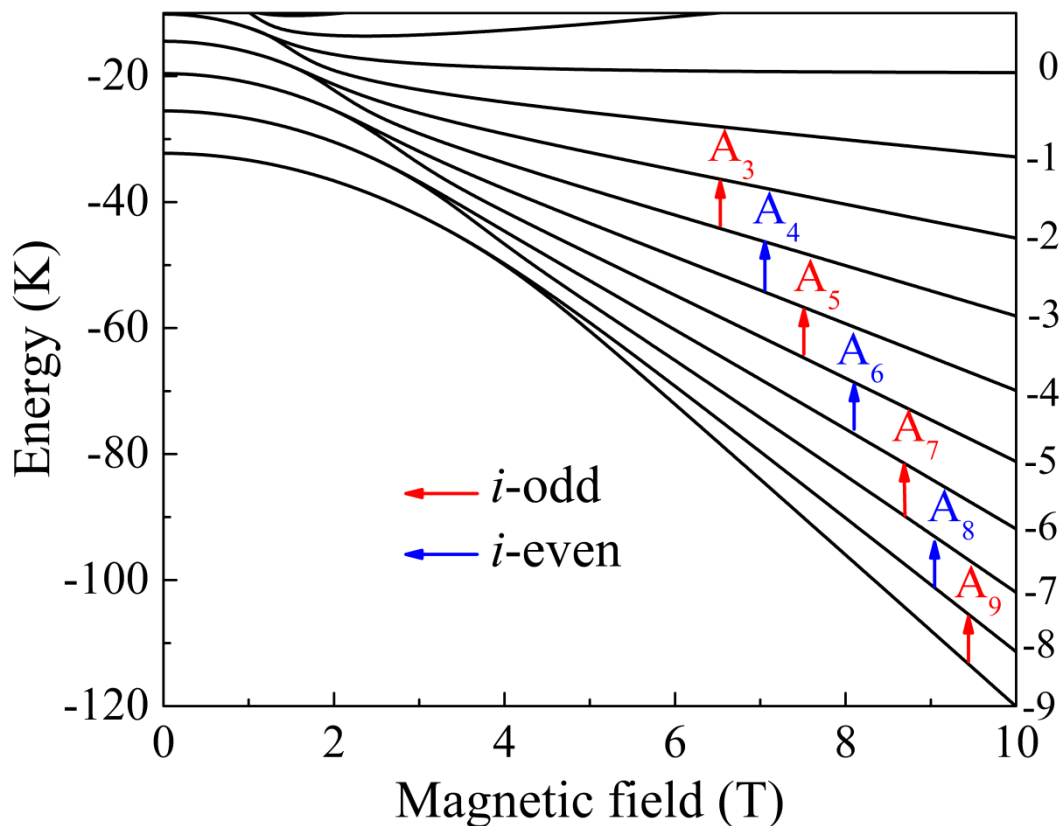


Figure 4-4. Zeeman diagram for the ground multiplet ( $S = 9$ ) of  $\text{Mn}_4\text{-Bet}$  with the field applied in the molecular  $xy$ -plane. For the reason of clarity, only a few of the lowest energy states are shown. The high-field spin projections onto the quantization axis ( $m$ ), which corresponds to the direction of the applied field, are labeled on the right hand side of the figure. The arrows correspond to EPR transitions from the  $m = -i$  to  $-i+1$  ( $A_i$ ) where the red and blue arrows indicate that  $i$  is even and odd, respectively.

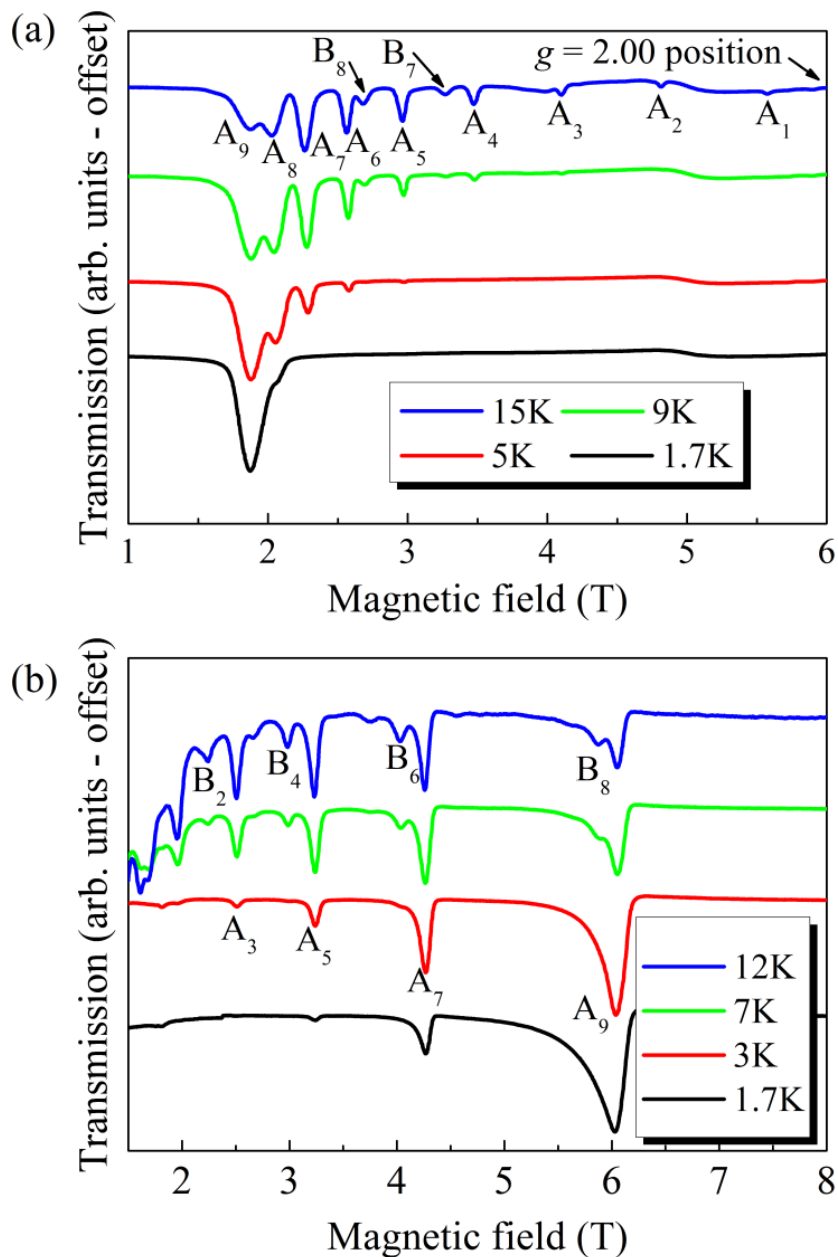


Figure 4-5. Temperature dependence of the EPR spectra for Mn<sub>4</sub>-anca. The spectra were obtained with the field (a) close to the easy axis at a frequency of 165 GHz and (b) in the hard plane at a frequency of 50.5 GHz. The peaks observed in the 15 K (a) and 12 K (b) spectra have been labeled according to the scheme described in the main text.

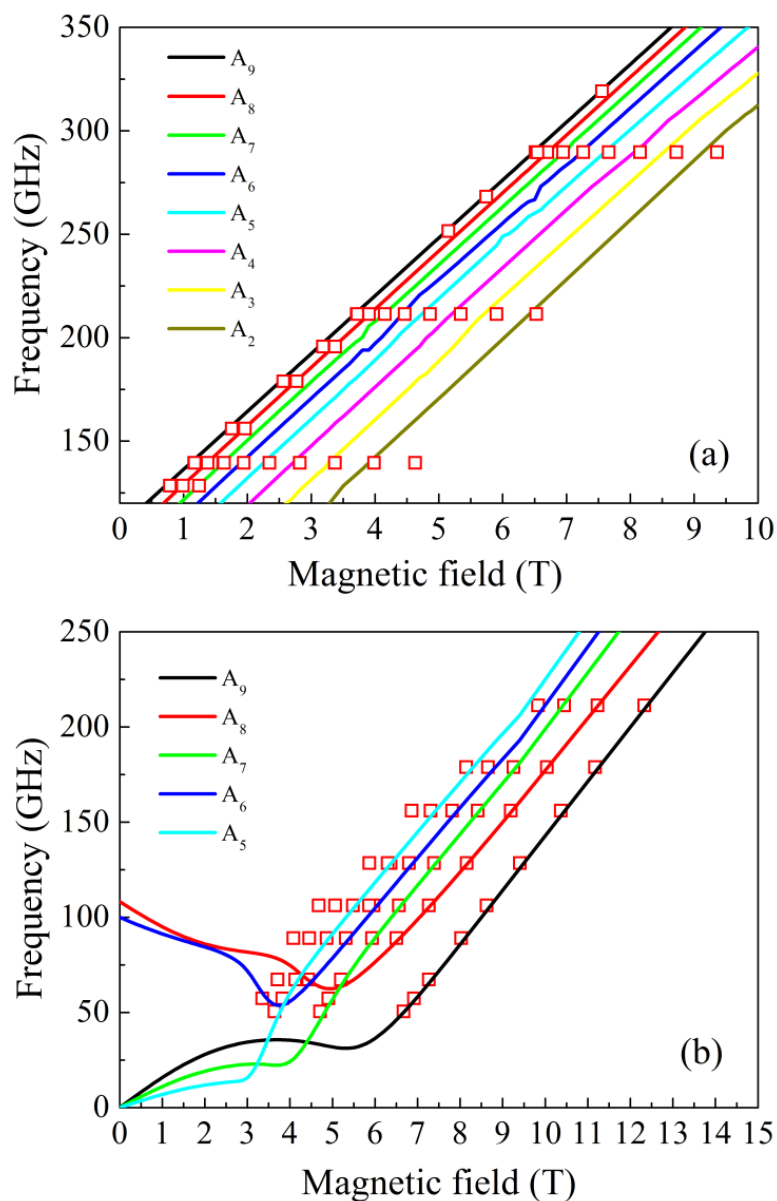


Figure 4-6. Plots of frequency versus field for Mn<sub>4</sub>-Bet showing the observed ground state EPR peak positions. The data were collected with the applied field (a) close to the molecular easy-axis at 3 K and (b) in the molecular hard plane at 5 K. Additional temperature dependence studies were performed at 139.5 GHz, 211.4 GHz and 289.6 GHz for the easy-axis orientation. The solid lines are the simulations of A series peak positions (red squares) using the Hamiltonian and parameters provided in the main text.

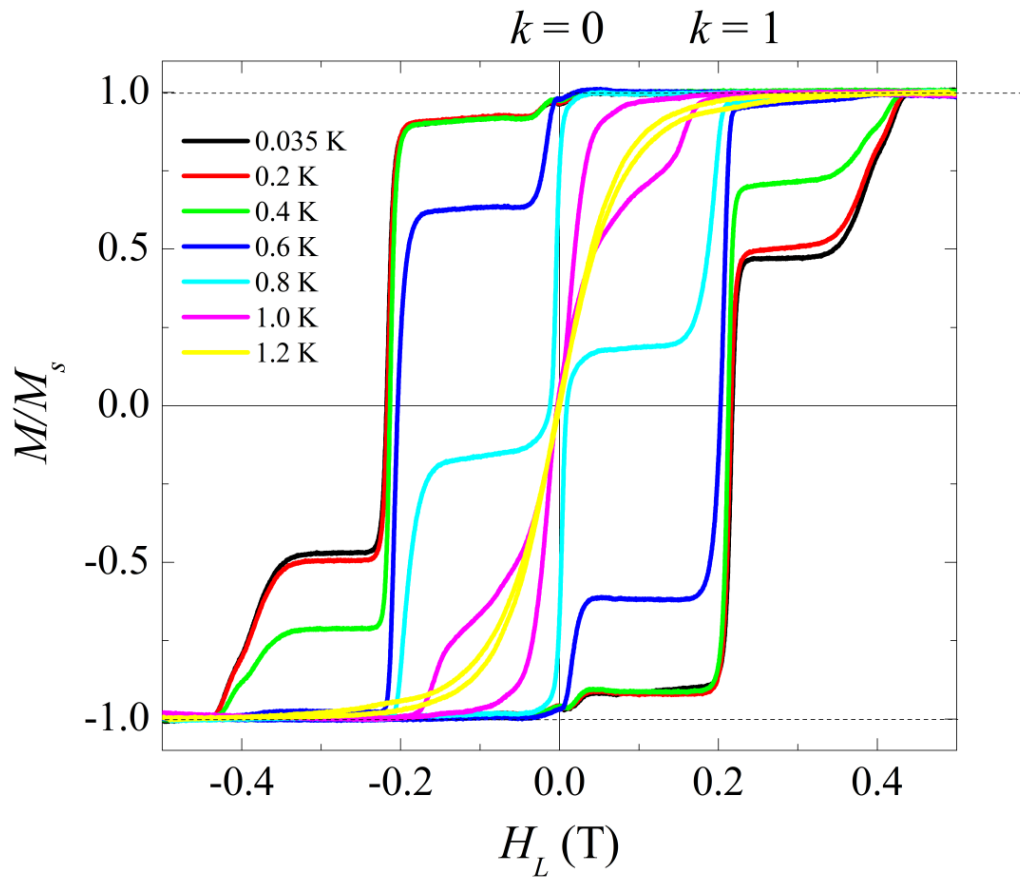


Figure 4-7. Hysteresis loops for Mn<sub>4</sub>-Bet recorded as a function of  $H_L$  at different temperatures. The QTM resonances are spaced by a step of  $\Delta H_L \approx 0.2$  T.

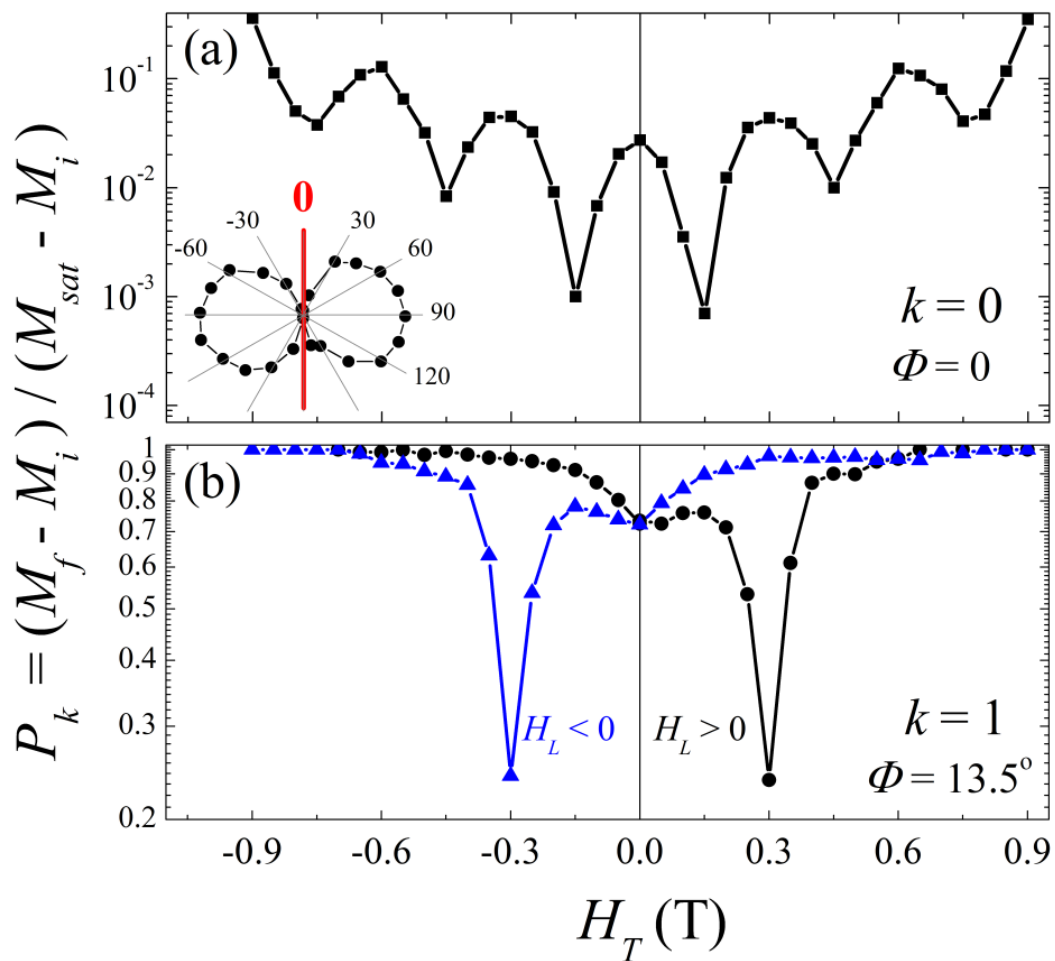


Figure 4-8. Modulation of the QTM probabilities for resonances of Mn<sub>4</sub>-Bet. (a)  $k = 0$  and (b)  $k = 1$  as a function of  $H_T$  applied at different angles,  $\Phi$ , within the hard plane of the Mn<sub>4</sub>-Bet SMM. The inset to (a) illustrates the two-fold angular modulation of  $P_0$  for  $H_T = 0.2$  T, providing clear evidence for a significant 2<sup>nd</sup>-order rhombic anisotropy. The asymmetry of the BPI pattern of oscillations in resonance  $k = 1$  is inverted upon reversal of  $H_L$ .

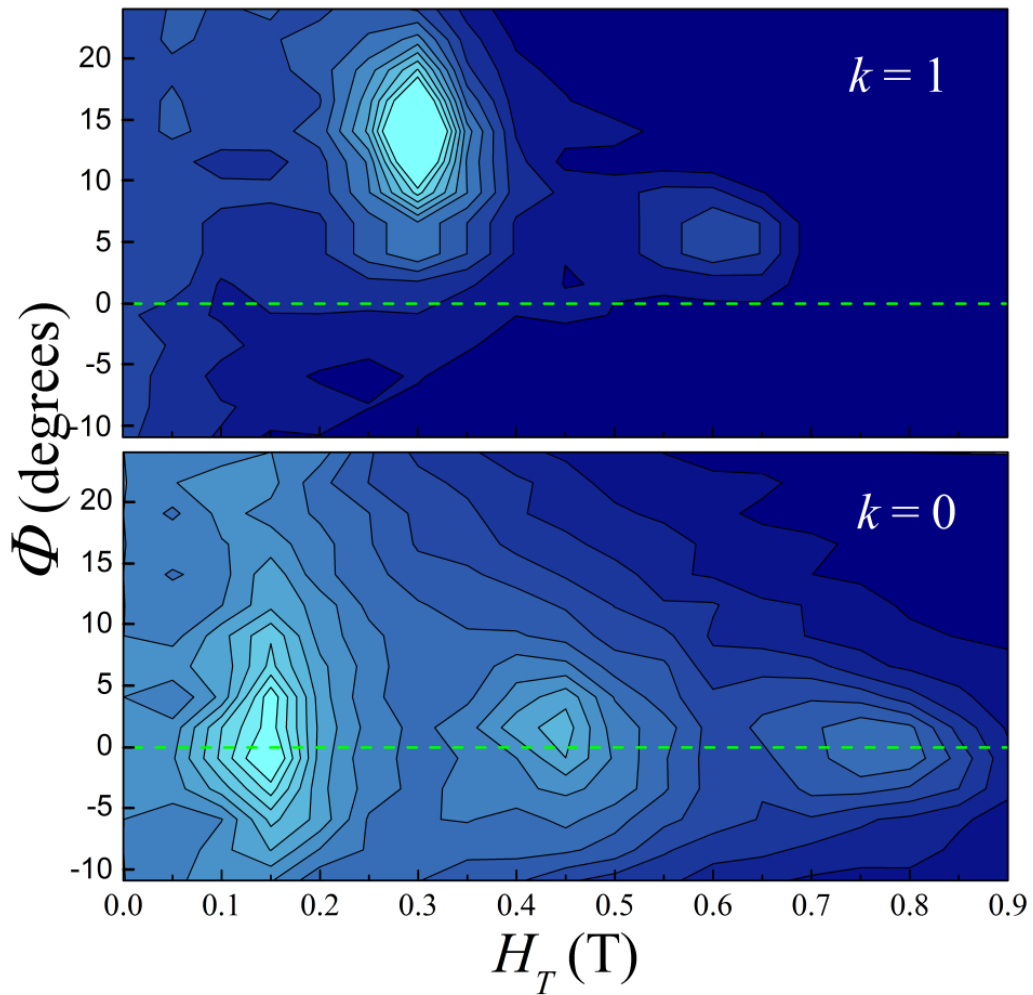


Figure 4-9. Contour plots of the QTM probabilities for resonances  $k = 0$  and  $k = 1$  of  $\text{Mn}_4\text{-Bet}$  as a function of  $H_T$  and  $\Phi$ . All of the  $k = 0$  minima lie approximately along the  $\Phi = 0$  axis, whereas the  $k = 1$  minima appear at different orientations for different  $H_T$  values.

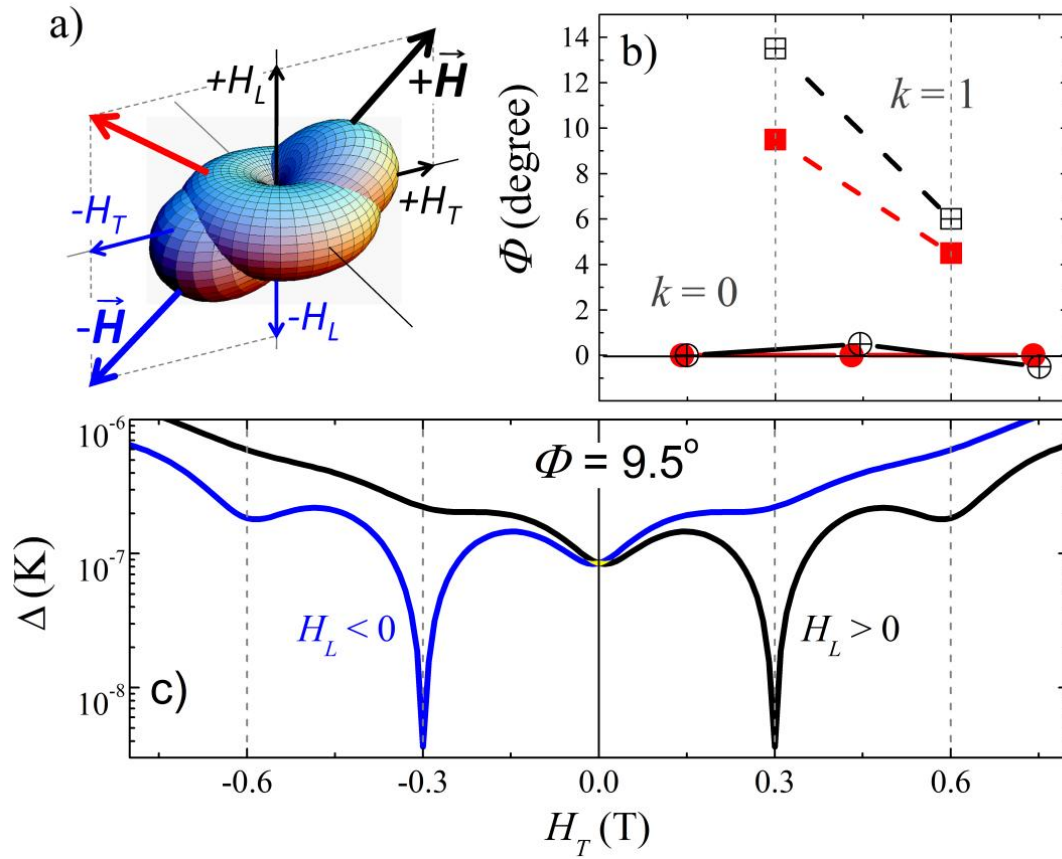


Figure 4-10. Simulations of the magneto-anisotropy and QTM probabilities of  $\text{Mn}_4\text{-Bet}$ . (a) The classical anisotropy barrier generated by the noncollinear ZFS tensors (see main text for explanation) and the different perspectives resulting from permutations of  $\pm H_T$  and  $\pm H_L$ . (b) Experimental (open black symbols) and calculated (solid red symbols)  $H_T$ - $\Phi$  dependence of the BPI minima for resonances  $k = 0$  (circles) and  $1$  (squares) obtained from Equation 4-1. (c) Calculated tunnel splittings for resonance  $k = 1$ , for  $\Phi = 9.5^\circ$ , as a function of  $H_T$  for  $H_L > 0$  (solid black line) and  $H_L < 0$  (solid blue line).

CHAPTER 5  
SLOW MAGNETIC RELAXATION INDUCED BY A LARGE TRANSVERSE ZERO-FIELD  
SPLITTING IN A  $\text{Mn}^{\text{II}}\text{Re}^{\text{IV}}(\text{CN})_2$  SINGLE-CHAIN MAGNET

The work presented in the chapter can be found from in the following article: Feng, X.; Liu, J.; Harris, T.D.; Hill, S.; Long, J.R., Slow Magnetic Relaxation Induced by a Large Transverse Zero-Field Splitting in a  $\text{Mn}^{\text{II}}\text{Re}^{\text{IV}}(\text{CN})_2$  Single-Chain Magnet. (In revision for submission to J. Am. Chem. Soc.)

### 5.1 Introduction

In this chapter, a different type of molecule-based magnet will be discussed, namely a single-chain magnet (SCM), which is a one-dimensional chain showing slow relaxation of magnetization at low temperatures. As discussed in Chapter 1, a SCM is a one-dimensional isolated chain constituted of anisotropic spin units connected in series. Compared to single-molecule magnets (SMMs), the advantage of pursuing high magnetic relaxation barriers in SCMs stems from the exchange coupling ( $J$ ) between the magnetic ions, which adds an additional energy term, known as the correlation energy,  $\Delta_\xi$ , to the expression for the relaxation barrier. The total magnetic relaxation barrier with respect to spin reversal can then be expressed as  $\Delta = \Delta_A + 2\Delta_\xi$  for an infinite chain, or  $\Delta = \Delta_A + 2\Delta_\xi$  for a finite chain. At low temperatures, a SCM typically falls into the second category due to the fact that the correlation length grows exponentially, thereby exceeding the finite chain length caused by small crystalline defects.

In designing a SCM, it is commonly believed that the individual spin units should possess easy-axis type anisotropy ( $D < 0$ ). A negative  $D$  value assures that states with maximum spin projection ( $m = \pm S$ ) onto the  $z$ -axis lie lowest in energy with a  $\sim |DS^2|$  barrier between the  $m = \pm S$  states, which leads to magnetic bistability at low temperatures. In an easy-axis type system, the presence of a rhombic transverse anisotropy ( $E$ ) is considered to be antagonistic to magnetic bistability since it causes quantum tunneling<sup>39, 87</sup> and reduces the effective relaxation barrier<sup>31, 32</sup>.

<sup>74, 94</sup>. Meanwhile, a positive  $D$  value results in ground states with minimal  $m$  ( $\pm 1/2$  for half-integer  $S$  and 0 for integer  $S$ ). In the pure axial case ( $E = 0$ ), the spin is completely delocalized within the  $xy$ -plane, i.e.,  $\langle S_x \rangle = \langle S_y \rangle = 0$ . Even in the presence of a sizable  $E$  term, which leads to an anisotropy in the  $xy$ -plane, strong quantum fluctuations prevent localization of the spin along any preferred direction in the  $xy$ -plane. So far, apart from a few exceptions<sup>112-114</sup> (where slow relaxation is attributed to a phonon-bottleneck effect or dipolar interactions), slow relaxation of magnetization has not been observed in  $D > 0$  type molecule. Therefore, it is commonly believed that negative  $D$  values are essential in the design of single-chain magnets.<sup>115, 116</sup>

The situation is quite different in the classical limit, i.e., a macroscopic spin, where quantum fluctuations are “switched off”. In the classical limit, with  $D > 0$ , the presence of a transverse interactions,  $E(\hat{S}_x^2 - \hat{S}_y^2)$ , causes an anisotropy in the  $xy$ -plane, where the energy of system equals to  $+ES^2$  and  $-ES^2$  when the spin is parallel to the  $x$ - and  $y$ -axes, respectively. In this scenario, the easy-axis would lie along either  $x$  or  $y$ , depending on the sign of  $E$ , and an anisotropic energy barrier would prevent rotation of the magnetic moment from  $+x$  to  $-x$  (or  $+y$  to  $-y$ ); the maximum barrier height, corresponding to rotation of the moment through  $z$ , would be dictated by  $D$ , while the activation energy for the spin reversal, which is determined by the minimum of the barrier, corresponding to the rotation within the  $xy$ -plane, would be dictated instead by  $E$ . However, such a scenario has, so far, not been considered as a possible source of slow magnetic relaxation behavior in either a SMM or SCM. The difficulties for achieving this in SMMs lie in the strong quantum fluctuations associated with the relative small spins of SMMs. In SCMs, where the magnetic moment of the chain can be much larger, it is possible to achieve slow magnetic relaxation through a barrier generated by a transverse anisotropy.

Recently, a series of cyano-bridged SCMs of the type  $(\text{DMF})_4\text{MReCl}_4(\text{CN})_2$  ( $\text{M} = \text{Mn}, \text{Fe}, \text{Co}, \text{Ni}$ ) have been synthesized with barriers to relaxation of  $\Delta = 44.6, 80.6, 24.5,$  and  $28.8$  K, respectively.<sup>63</sup> Hexa-coordinated  $\text{Re}^{\text{IV}}, [\text{ReCl}_4(\text{CN})_2]^{2-}$ , was used as the building block owing to its sizable spin ground state ( $S = 3/2$ ) and strong magneto-anisotropy originating from strong spin-orbit coupling associated with the third-row transition metal ions<sup>117-119</sup>. Magnetic analysis reveals that the chain compounds in this family fall neither in the Ising nor Heisenberg limit<sup>63</sup>, where the theory of  $\Delta$  (as a function of  $S, D$  and  $J$ ) is still under investigation. Given that the magnetic behavior of the chain compounds results from a combination of the magnetic anisotropy of the individual spin centers and the interactions between adjacent spins, the study of molecules mimicking small fragments of the chain (containing one, two, or three metal centers) may afford substantial insight into the mechanisms that lead to the observed magnetic data. Hence, we performed electron paramagnetic resonance (EPR) studies of three compounds,  $(\text{Bu}_4\text{N})_2[\textit{trans}\text{-ReCl}_4(\text{CN})_2]\cdot 2\text{DMA}$  (**1**),  $(\text{DMF})_4\text{ZnReCl}_4(\text{CN})_2$  (**2**), and  $[(\text{PY5Me}_2\text{Mn})_2\text{ReCl}_4(\text{CN})_2](\text{PF}_6)_2$  (**3**) in order to elucidate the influence of the metal coordination environment and magnetic interactions on the magneto anisotropy of the  $\text{Re}^{\text{IV}}$  ion in the  $[\text{ReCl}_4(\text{CN})_2]^{2-}$  magnetic core. Surprisingly, **1-3** exhibit easy-plane anisotropies ( $D > 0$ ) with significant  $E$  values, suggesting the presence of the same type of anisotropy ( $D > 0$ ) in the chain compound  $(\text{DMF})_4\text{MnReCl}_4(\text{CN})_2$  (**4**). We describe a mechanism for slow magnetic relaxation in a single-chain magnet that arises due to a barrier created by the transverse anisotropy  $E$  rather than the axial anisotropy  $D$ . Based on this model and our EPR results, we calculated a relaxation barrier in **4** which is in excellent agreement with the results of magnetic studies. To the best of our knowledge, this is the first observation of slow relaxation arising from  $E$  in any coordination compound.

The studies presented in this chapter were conducted in collaboration with Dr. Jeffrey Long's group at the University of California, Berkeley. The samples were synthesized by Dr. Long's group. X-ray crystallography and magnetometry measurements were performed by Dr. Long's group. EPR measurements and the theoretical analysis was performed at the NHMFL and form the subject of this chapter.

## 5.2 Introduction to the Structures of 1-4

The structures for complexes **1-4** are shown in Figure 5-1. Compound **2** is a structural analogue of **4**, where the  $\text{Mn}^{\text{II}}$  ions are replaced by diamagnetic  $\text{Zn}^{\text{II}}$  ions. The crystal structures of **1-4** reveal an octahedral coordination geometry around the  $\text{Re}^{\text{IV}}$  center, with four chloride ligands in the equatorial positions and two axial cyanide ligands. A comparison of the bond lengths and bond angles is included in Table 5-1, where one can find that the coordination of the  $\text{Re}^{\text{IV}}$  is essentially a constant for all compounds. This reinforces the viability of **1-3** as models for the chain compound **4**. Additionally, within each structure, no significant hydrogen bonding contacts between chains or molecules are evident in any of the structures, ruling out the presence of any significant pathways for long-range magnetic interactions other than those along the chains in **4**.

There are several features of these structures which are noteworthy. We discuss these by using **1** as an example; the following discussion can be applied generally to complexes **1-4**. Complex **1** crystallizes in a triclinic space group  $P-1$  and lies about an inversion center. The molecule only possesses an inversion symmetry, which indicates that a transverse anisotropy,  $E$ , is allowed by symmetry. In particular, we note that the four chloride ions are coplanar, which is guaranteed by the inversion symmetry of the molecule. These four chloride ions determine the molecular  $xy$ -plane with the Re ion located approximately at the center. However, there are two different Re-Cl bond lengths, as indicated in Table 5-1. In addition, we note that the Cl-Re-Cl

bond angle is not 90° (90.1°), while the Re-C bonds are not perpendicular to the plane formed by the chloride ions (the C-Re-Cl bond angle  $\neq$  90°). These features, especially the presence of two different Re-Cl bond lengths, strongly suggest a transverse anisotropy associated with the Re<sup>IV</sup> ion, which is confirmed by the EPR experiments (*vide infra*).

Table 5-1. Selected Interatomic Distances (Å) and Angles (°) for compounds 1-4.

	<b>1</b>	<b>2</b>	<b>3</b>	<b>4</b>
Re-Cl	2.351(1), 2.341(1)	2.312(4), 2.316(3)	2.344(2), 2.330(1)	2.340(1), 2.343(2)
Re-C	2.148(4)	2.123(6)	2.134(5)	2.125(1)
M-N		2.121(2)	2.192(1)	2.228(1)
M-N <sub>py</sub>			2.224(4)	
M-O		2.100(2)		2.181(1)
Re-C-N	177.2(1)	175.0(1)	175.2(1)	175.8(1)
M-N-C		158.8(1)	154.1(1)	158.8(1)
Cl-Re-Cl	90.1 (4)	90.5(1)	90.1(4)	90.6(1)
C-Re-Cl	88.5(1)	88.1(2)	89.0(4)	89.0(1)

### 5.3 Discussions of Magnetometry and EPR Results

#### 5.3.1 Complex 1

Previous analysis of the reduced magnetization measurements on **1** suggested an easy-axis type anisotropy with  $D = -27.4$  K.<sup>63</sup> However, as we discussed in Chapter 2, extracting the sign of  $D$  from magnetic data can often be unreliable. In fact, recent reanalysis of the magnetic data shows that they can also be fitted with the following parameters:  $D = +10.4$  K,  $E = 2.88$  K and  $g = 1.88$ . Furthermore, slow relaxation of magnetization was not observed on **1**, even upon application of a small dc field, which contrasts with expectations for a strong easy-axis type anisotropy ( $|D|(S^2-1/4) = 54.8$  K if  $D = -27.4$  K, which is a sizeable relaxation barrier). Therefore, in order to obtain a definitive determination of the magnetic anisotropy of the  $[\text{Re}(\text{CN})_2\text{Cl}_4]^{2-}$  building block (**1**), EPR measurements were carried out in compound **1** at high fields.

Both single-crystal and powder EPR measurements were performed; experimental details can be found elsewhere.<sup>72, 81</sup> The EPR data can be described by the following spin Hamiltonian:

$$\hat{H} = D\hat{S}_z^2 + E(\hat{S}_x^2 - \hat{S}_y^2) + \mu_B \mathbf{B} \cdot \vec{g} \cdot \hat{S} \quad (5-1)$$

with  $S = 3/2$  and  $0 < |E| < |D|/3$ . Figure 5-2 plots the peak positions of EPR transitions observed via high-field studies at 1.3 K; the crystal was oriented *in situ* so that the field was aligned close to one of the principal axes of the magneto-anisotropy tensor, determined to be the magnetic hard (z-) axis (*vide infra*). The most notable feature of these low-temperature spectra is the fact that three resonances are observed in the frequency range from 60 to 130 GHz (see Figure 5-2 inset): the sharp peak at low field (marked by a blue arrow) corresponds to a transition within the lowest Kramers doublet, while the broad peaks at high field (marked by red arrows) correspond to inter-Kramers transitions. The differences in linewidth can be explained on the basis of  $D$ - and  $E$ -strain which primarily influence inter-Kramers transitions.<sup>77, 78</sup> Figure 5-3 shows the temperature dependence studies at 126.9 GHz which indicate that all three resonances correspond to excitations from the lowest-lying energy level within the  $S = 3/2$  manifold. The thick solid curves in Figure 5-2 correspond to the best simulation employing Equation 5-1, assuming a positive  $D$  value. The obtained parameters are:  $D = +15.8$  K,  $|E| = 4.6$  K and  $g_z = 1.58$ , with the field being close ( $3^\circ$  misalignment) to the molecular z-axis.

The importance of the single-crystal EPR results lies in the fact that the inter-Kramers transitions were observed, which give a direct determination for the zero-field splitting (ZFS) between the  $m = \pm 3/2$  and  $\pm 1/2$  Kramers doublets; hence, the magnitude of  $D$ . However, there are actually two scenarios, i)  $D > 0$  and ii)  $D < 0$ , that can account for the high-field single-crystal data shown in Figure 5-2; both sets of parameters involve a significant biaxiality, i.e., an  $E$  term approaching  $|D|/3$ . Therefore, In order to discriminate between these two cases, low-field powder EPR measurements were performed (see Figure 5-4). The observed EPR transitions correspond to the three principal components of the effective  $g$ -tensor associated with the lowest

Kramers doublet. The powder results are also included in the bottom left part of Figure 5-2. First, note that the highest field (lowest effective  $g$ ) data points for the powder overlay exactly on the single crystal data, thus confirming that the sample was well aligned for the high-field measurements. The thick solid curves in Figure 5-2 and 5-4 correspond to the best simulations of the combined single-crystal and powder data sets employing Equation 5-1 using the aforementioned parameters with the addition of  $g_x = g_y = 1.89$ . A reasonable simulation can be obtained for the negative  $D$  case as well. However, it yields  $g$  values greater than 2.00, whereas the principal Landé values must be less than 2.00 for an orbitally non-degenerate atom with a less than half-filled  $d$  shell, as is the case for octahedrally coordinated  $\text{Re}^{\text{IV}}$  ( $5d^3$ , with  $S = 3/2$  and  $L = 0$ ). In other words, the negative  $D$  (easy-axis) simulation is unphysical. We thus conclude that the  $D$  value is positive for **1**, and we shall see below that the situation is even more definitive in the case of compound **2**.

We return to the discussion of the high-field single-crystal measurements. It is notable that the low-field intra-Kramers transitions in Figure 5-2 do not lie on a straight line that intersects the origin (thin solid line). This may be understood in terms of an avoided level crossing caused by the rhombic  $E$  term in Eq. (1), as illustrated in Figure 5-5, which also explains the broadening of the intra-Kramers resonance with increasing frequency. In the absence of an  $E$  term, there would be no interaction between the  $m_s = -3/2$  and  $+1/2$  states and the spectrum would be linear in  $B_z$  (orange curves in Figure 5-5), i.e., the intra-Kramers data would lie on a straight line passing through the origin. Consequently, the departure of the low-field data from the thin line in Figure 5-2 provides one of the main constraints on  $E$ , the other being the splitting between the  $x$  and  $y$  components of the powder spectrum. Meanwhile, the inter-Kramers transitions above 15 T primarily constrain  $D$  and  $g_z$ . Finally, a small field misalignment of  $\theta = 3^\circ$  was considered due to

the fact that a single-axis crystal rotation does not guarantee exact coincidence with the molecular  $z$ -axis. This misalignment accounts for the 2<sup>nd</sup> avoided crossing at ~28 T, but it does not affect the low field data significantly. Thus, even though the high-field simulation contains four variables, the obtained parameters are well constrained. Moreover, they are further constrained by the powder measurements.

The obtained  $E$  parameter is quite significant, corresponding to  $|D|/3.4$ , i.e., very close to the maximum allowable value. For the extreme biaxial case in which  $E = |D|/3$ , the  $D > 0$  and  $D < 0$  parameterizations are in fact equivalent. It is precisely for this reason that good simulations can be obtained for both cases, i.e., the two parameterizations are similar, though it should be stressed that the powder measurements clearly favor the positive  $D$  scenario. In any case, the underlying magnetic properties resulting from either parameterization would be expected to be quite similar. Moreover, such a strong  $E$  value is of no surprise, since the molecule only possesses  $C_i$  symmetry.

### 5.3.2 Complex 2

Due to the difficulty associated with interpreting EPR data from a dynamic chain system, where collective spin wave resonance is observed instead of discrete paramagnetic resonance,<sup>16</sup> zero-field splitting parameters for  $\text{Re}^{\text{IV}}$  were not directly obtained from the EPR data for the chain compound **4**. As a means of isolating the magnetic anisotropy of the  $\text{Re}^{\text{IV}}$  ions within the chain, the isostructural compound **2** was prepared. Here, the paramagnetic  $\text{Mn}^{\text{II}}$  ions have been replaced by diamagnetic  $\text{Zn}^{\text{II}}$  ions in order to prevent significant exchange interactions involving the  $\text{Re}^{\text{IV}}$  centers, while preserving any effects that stem from connecting  $[\text{ReCl}_4(\text{CN})_2]^{2-}$  units to other metal centers via the cyanide ligands. To confirm the magnetic isolation of the  $\text{Re}^{\text{IV}}$  centers, variable-temperature dc magnetic susceptibility data were collected for a microcrystalline sample of **2**. The measurements shows that the  $\chi_{\text{M}}T$  vs  $T$  plots of **1** and **2** are essentially superimposable,

indicating an absence of inter- and/or intra-chain magnetic interactions in **2**. Importantly, ac magnetic susceptibility measurements as a function of both frequency and temperature on a polycrystalline sample of **2** revealed no slow relaxation behavior at or above 1.8 K.

Due to the reason that sufficiently sized single-crystals were not available, EPR measurements were carried out on a powder sample of **2**, as shown in Figure 5-6. Just like complex **1**, three spectral features are resolved, corresponding to the principal components of the effective  $g$ -tensor associated with the lowest Kramers doublet. In the case of easy-plane anisotropy ( $D > 0$ ), the  $x$ - and  $y$ -components should occur at fields below the spin-only  $g = 2.00$  position (dashed line), while the  $z$ -component should occur above; the opposite would hold for the easy-axis ( $D < 0$ ) case. As seen in Figure 5-6, the powder measurements clearly indicate easy-plane-type anisotropy ( $D > 0$ ), although they do not permit a direct determination of the magnitude of  $D$ . Meanwhile, the sizeable splitting between the  $x$  and  $y$  components of the spectrum again signifies appreciable biaxiality, i.e., a significant  $E$  term. Attempts to detect inter-Kramers transitions were unsuccessful (sufficiently sized single-crystals were not available). Therefore, for the purposes of simulation, we were forced to adopt the  $D$  value obtained for **1**, i.e., +15.8 K. The solid curves in Figure 5-6 represent the best simulation of the peak positions employing Equation 5-1 with  $|E| = 3$  K,  $g_x = g_y = 1.78$  and  $g_z = 1.94$ . As noted already, it is impossible to obtain any reasonable simulation with  $D < 0$ . However, the obtained  $E$  value is rather well constrained by the splitting between the  $x$  and  $y$  components of the powder spectrum. Therefore, these simulations unambiguously demonstrate that **2** possesses easy-plane type anisotropy and appreciable transverse anisotropy, in analogy with complex **1**.

### 5.3.3 Complex 3

To exclude the possibility that magnetic exchange coupling may act to invert the sign of  $D$  in the chain compound **4** relative to its constituent  $[\text{ReCl}_4(\text{CN})_2]^{2-}$  unit, compound **3** was

prepared and investigated. In particular, magnetic and EPR measurements were carried out on polycrystalline samples of **3** to study the ZFS parameters of  $\text{Re}^{\text{IV}}$  in the presence of magnetic exchange coupling. First, the sign and magnitude of  $J$  were probed through variable-temperature dc magnetic susceptibility measurements. A fit to the dc susceptibility results with the following Hamiltonian,  $\hat{H} = 2J(\hat{\mathbf{s}}_{\text{Re}} \cdot \hat{\mathbf{s}}_{\text{Mn1}} + \hat{\mathbf{s}}_{\text{Re}} \cdot \hat{\mathbf{s}}_{\text{Mn2}})$ , gives antiferromagnetic interactions between the  $\text{Re}^{\text{IV}}$  and  $\text{Mn}^{\text{II}}$  ions with  $J = 4.3$  K. This value is comparable to the magnetic coupling observed in **4**, where  $J = 7.2$  K. The slight difference in the magnitude of  $J$  may be due to the different ligand field around  $\text{Mn}^{\text{II}}$  and the small differences in the Mn-N-C angles. Thus, **3** should provide a reasonable model of the Mn...Re...Mn motif in **4**. We note that slow relaxation behavior was not observed in the variable frequency ac susceptibility measurements at temperatures above 1.8 K, even in the presence of an applied field, suggesting the possibility of easy-plane type anisotropy in **3**.

EPR studies on **3** confirm that the  $\text{Re}^{\text{IV}}$  ion possesses a positive  $D$  parameter, lending further weight to arguments that **4** also experiences easy-plane-type anisotropy. Figure 5-7 plots the frequency dependence of high-frequency EPR peak positions obtained from studies of a powder sample of **3** at 3.5 K; the inset displays a representative spectrum collected in first-derivative mode at 208 GHz. Three relatively strong features are observed, which we label  $\alpha_y$ ,  $\alpha_z$  and  $\beta$ . At high fields and frequencies, the slopes of the  $\alpha_y$  and  $\alpha_z$  branches agree with expectations for standard EPR transitions with  $\Delta m = 1$  and  $g \approx 2$ . Meanwhile, the slope associated with the  $\beta$  branch suggests that it is a double quantum transitions with  $\Delta m = 2$  and  $g \approx 4$ . We associate the  $\alpha_y$  and  $\alpha_z$  branches with the parallel ( $z$ ) and perpendicular ( $y$ ) extremes of the high-field spectrum. We note that the low-field spectrum would be rather more complex, thereby illustrating the importance of high field measurements.

Unlike the powder results for **1** and **2**, the  $\alpha_y$  and  $\alpha_z$  resonance branches correspond to excitations within a coupled molecular spin state experiencing zero-field-splitting. It is for this reason that the high-field portions of the spectrum extrapolate to finite zero-field offsets, unlike the transitions within the lowest Kramers doublet in the case of **1** and **2**. Most importantly, the zero-field offsets deduced from Figure 5-7 provide direct information on the anisotropy associated with the  $\text{ReMn}_2$  molecular units of **3**. The results may be interpreted by treating the molecule as a spin  $S = 7/2$  object. This assignment is based on the magnetic measurements that indicate antiferromagnetic coupling between the  $\text{Re}^{\text{IV}}$  and  $\text{Mn}^{\text{II}}$  moments, giving a total ground state spin  $S = 2 \times 5/2 - 3/2 = 7/2$ . The solid lines are the simulations employing Equation 5-1 and the following molecular zero-field-splitting parameters:  $D = +0.43$  K,  $|E| = 0.043$  K and  $g = 2.00$ . As noted above, the  $\alpha_z$  branch corresponds to the ground state transition with the field being parallel to the molecular  $z$ -axis, while  $\alpha_y$  corresponds to the same transition but with the field parallel to  $y$ . The  $x$ -component is buried within the very large signal close to  $g = 2.00$ . The simulations also successfully account for the double quantum transition ( $\beta$ ) assuming that it belongs to the  $y$ -component of the spectrum. It is noteworthy that double quantum transitions usually appear when the field is applied perpendicular to the dominant quantization axis ( $z$ -axis), which is consistent with our observations and provides further confirmation for the peak assignments.

Although fine structure peaks are not resolved, observation of the  $x$  and  $y$  extrema provide an extremely robust constraint on the sign of the  $D$  parameter: the fact that the shift of the  $z$ -component to the high-field side of the isotropic  $g = 2.00$  position is substantially greater than that of the  $y$ -component to the low field side can be taken as a sure sign that the molecular anisotropy is of the easy-plane type.

We can estimate the anisotropy parameters associated with the  $\text{Re}^{\text{IV}}$  ion using the projection method.<sup>120</sup> The zero-field-splitting associated with octahedrally coordinated  $\text{Mn}^{\text{II}}$  may be assumed to be negligible; thus, the anisotropy of **3** will be dominated by  $\text{Re}^{\text{IV}}$ . The projection method gives  $\vec{D}_{\text{mol}} = 0.0143 \times \vec{D}_{\text{Re}}$ , where  $\vec{D}_{\text{mol}}$  and  $\vec{D}_{\text{Re}}$  are the anisotropy tensors of the  $\text{ReMn}_2$  molecule and the  $\text{Re}^{\text{IV}}$  ion, respectively. Therefore, we can deduce that  $D_{\text{Re}} \approx +30$  K, i.e., it is of the easy-plane type, and  $E_{\text{Re}} \approx 3$  K. However, due to the significant uncertainty associated with the resonance positions in Figure 5-7 and the many simplifying assumptions made in the analysis, these values should be considered as highly approximate. Nevertheless, the data once again confirm easy-plane anisotropy and considerable rhombicity.

#### 5.4 Discussion of the Magnetic Relaxation Process

High-spin  $\text{Mn}^{\text{II}}$  ions typically possess near negligible magnetic anisotropy.<sup>82</sup> Consequently, the magnetization relaxation barrier in **4** must arise primarily from the anisotropy of the  $\text{Re}^{\text{IV}}$  ions. However, the EPR studies reported here clearly indicate the presence of a positive  $D$  for  $\text{Re}^{\text{IV}}$ . Moreover, the theoretical relaxation barrier for **4**, obtained using the magnitude of  $D$  deduced both by EPR and magnetic measurements, is in stark disagreement with the experimental barrier of 17.28 K. The estimated anisotropy barriers are 54.8 K and 31 K using the magnitude of  $D$  (assuming  $D$  negative) deduced from the magnetic measurements and EPR, respectively. These factors suggest that new physics may be at play in governing the magnetic relaxation of **4**.

If one considers the doubly degenerate  $M_S = \pm 1/2$  ground levels of an isolated  $S = 3/2$  molecule with positive  $D$ , then extreme quantum tunneling effects prevent localization of the molecular magnetic moment within the  $xy$ -plane, i.e.  $\langle \hat{S}_x \rangle = \langle \hat{S}_y \rangle = 0$ . However, the coupling of such spins, one-by-one, to form a ferrimagnetic chain, results in a gradual suppression of these tunneling effects. In such a description, the chain possesses a giant spin,  $S$ , which scales with the

chain correlation length,  $L$ . In the case of **4**, the coordination environments of the  $\text{Re}^{\text{IV}}$  ions are collinear throughout the chains, with the axial  $z$ -direction approximately parallel to the direction of chain propagation. As such, the preferred orientation of the giant spin,  $S$ , lies in the plane perpendicular to the chain (see Figure 5-8). A transverse anisotropy then creates a preferred axis within this plane, although quantum tunneling may still prevent localization of  $S$  for small chain lengths. However, as the chain correlation length grows, these fluctuations diminish as the quantum tunneling is increasingly suppressed.

The suppression of quantum tunneling is one of the key ingredients for observing slow magnetic relaxation in **4**. To evaluate the correspondence between quantum tunneling and the size of the chain, we treated a finite length chain as a microscopic molecule whose spin is proportional to the number of units,  $N$  ( $= S$ ); each unit has  $s = 1$  due to the antiferromagnetically coupled  $\text{Re}^{\text{IV}}$  and  $\text{Mn}^{\text{II}}$ ,  $s = 5/2 - 3/2 = 1$ . Figure 5-9 shows the dependence of the ground  $k = 0$  tunneling gap as a function of the size of the chain. Because the Hilbert space associated with the chain grows exponentially with increasing  $N$ , we performed simulations with two different approaches (a) a multi-spin (MS) Hamiltonian, which considers the chain as  $N$  coupled  $s = 1$  units, and (b) a giant-spin approximation (GSA) Hamiltonian, which treats the chain as a giant molecule with  $S = N$ . The simulations were performed to study the zero-field ground state tunneling gap ( $k = 0$  gap) as a function of  $N$ . The data points in the figure are simulation employing the MS Hamiltonian, treating the chain as  $s = 1$  units connected in series with a ferromagnetic interaction  $|J| = 7.2$  K. The solid line is the simulation performed with the GSA in which the anisotropy parameters of the molecule is calculated via the projection method.<sup>120</sup> Using this method, the chain possesses only second order anisotropies,  $D_{mol}$  and  $E_{mol}$ ; the high order anisotropies are zero because  $J$  is assumed to be infinite, as discussed in Chapters 2 and 3.

It is interesting to note that, in both methods, the shape of the magneto anisotropy potential energy surface of the system, i.e., the ratio between the molecular axial and transverse anisotropies,  $D_{mol}/E_{mol}$ , remains a constant when the size of the system grows. This is due to the fact that the ZFS tensors of all units in the chain are collinear; therefore, they directly add together forming the anisotropy of the chain. As shown in the figure, in both models, the tunneling gap decreases exponentially as the size of the system grows, which indicates that pure quantum tunneling quickly vanishes as the chain become sizable. Hence, in a chain with reasonable length, quantum tunneling can be neglected and the dynamics of the chain is completely governed by Glauber's theorem. Another method of visualizing such an effect is to consider the probability that all spins within the chain tunnel simultaneously, as would be required if the total spin were to tunnel coherently. Clearly, this probability decreases exponentially with increasing number of spins in the chain. Consequently, in the limit of large correlation length,  $S$  can be treated classically.

Figure 5-10 depicts the classical potential energy surface in spin space corresponding to the zero-field operator equivalent terms given in Equation 5-1, with  $D > 0$  and  $|E/D|$  equal to the ratio found from the present EPR experiments. The radial distance to the surface represents the energy of a spin as a function of its orientation. The minimum energy occurs when the spin points along  $\pm y$ , with an energy barrier separating these two orientations. The barrier maximum occurs in the  $yz$ -plane, and is determined by  $D$ . Meanwhile, it is  $E$  that sets the energy scale of the barrier minimum for rotation in the  $xy$ -plane. In the large length limit, the anisotropy barrier against coherent rotation of an entire chain will be quite considerable, because the anisotropies of the individual  $\text{Re}^{\text{IV}}$  centers sum together. Nevertheless, we propose that magnetization dynamics can still proceed via the Glauber mechanism, except that the relevant anisotropy energy scale is

determined by  $E$  rather than  $D$ . As we discussed in Chapter 1, the anisotropy barrier in the Glauber theorem is characterized by the characteristic relaxation time for flipping an isolated spin unit. According to our previous discussions, the spin flipping process corresponds to the rotation of the spin in its  $xy$ -plane; therefore, it is of no surprise that this characteristic time is determined by  $E$ . As such, the anisotropy energy associated with the reversal of a single  $\text{Re}^{\text{IV}}$  spin within the chain is given by  $\Delta_{\text{A}} = 2|E|S^2$ . Considering the value of  $|E| = 3 \text{ K}$  deduced from the EPR measurements, the anisotropy energy of **4** can be estimated at  $\Delta_{\text{A}} = 13.7 \text{ K}$ . Using the previously obtained value of the correlation energy of  $\Delta_{\zeta} = 27.4 \text{ K}$ , along with the expression for the overall relaxation barrier for a chain in the finite-size limit  $\Delta = \Delta_{\text{A}} + \Delta_{\zeta}$ , a value of  $\Delta = 41.1 \text{ K}$  is obtained for **4**. Remarkably, this value is in excellent agreement with the experimentally determined value of  $\Delta = 44.6 \text{ K}$ , which has heretofore been unexplainable in terms of uniaxial magnetic anisotropy ( $D$ ) and correlation. Moreover, in the previous work on the isostructural chain compounds  $(\text{DMF})_4\text{MReCl}_4(\text{CN})_2$  ( $\text{M} = \text{Mn}, \text{Fe}, \text{Co}, \text{Ni}$ ), the experimental correlation energy of  $(\text{DMF})_4\text{NiReCl}_4(\text{CN})_2$  was found to be  $\Delta_{\zeta} = 12.7 \text{ K}$ . Taking the small contribution of the zero-field splitting of octahedral  $\text{Ni}^{\text{II}}$  ions and the anisotropy barrier ( $\Delta_{\text{A}} = 13.7 \text{ K}$ ) estimated from EPR data into account, the overall relaxation barrier  $\Delta = 26.1 \text{ K}$  agrees very well with the experimental value of  $\Delta = 28.8 \text{ K}$ , providing further support for the relaxation process via transverse anisotropy. Finally, note that the anisotropy energy of the  $\text{CoRe}$  and  $\text{FeRe}$  chain compounds are different, as the important contribution of zero-field splitting from high-spin  $\text{Co}^{\text{II}}$  and  $\text{Fe}^{\text{II}}$  enables a more complicated relaxation mechanism.

## 5.5 Summary

The studies presented in this chapter demonstrate that slow relaxation of magnetization can arise from transverse anisotropy. In particular, high-field, high-frequency EPR measurements on

a series of model compounds (**1-3**) show that the magnetic relaxation in the single-chain magnet  $(\text{DMF})_4\text{MnReCl}_4(\text{CN})_2$  is governed by a nonzero  $E$  term, despite the presence of a positive  $D$ . Based on our model, the theoretical barriers are in great agreement with the experimental results. The observation of slow relaxation arising from  $E$  is, to our knowledge, an unprecedented phenomenon in molecular magnetism, and it represents a fundamentally new design strategy toward constructing low-dimensional magnetic materials.

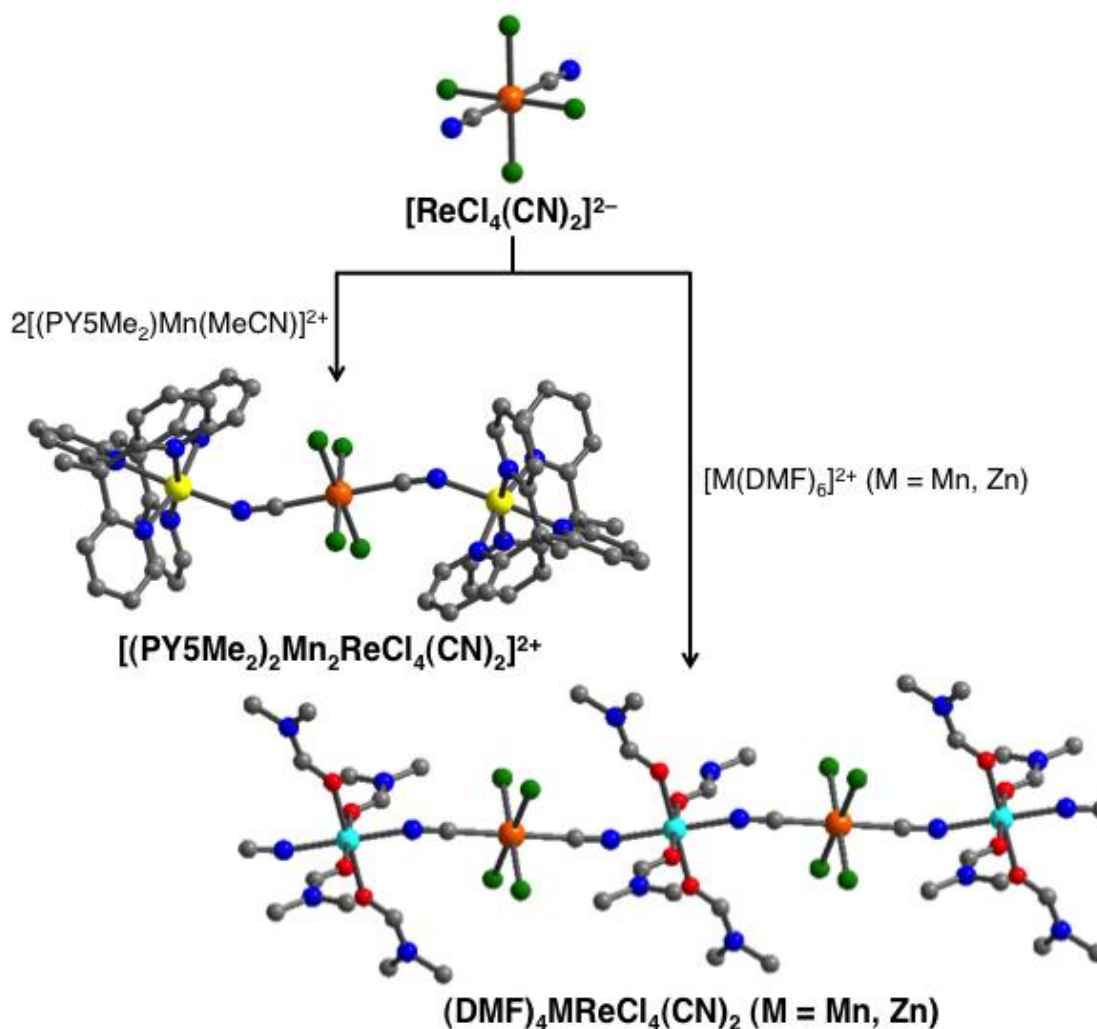


Figure 5-1. The structures of complexes **1-4** presented in Chapter 5. The figure illustrates the reaction of *trans*- $[\text{ReCl}_4(\text{CN})_2]^{2-}$  (upper) with  $[\text{Zn}(\text{DMF})_6]^{2+}$  to form the one-dimensional solids  $(\text{DMF})_4\text{ZnReCl}_4(\text{CN})_2$  (left), with  $[(\text{PY5Me}_2)\text{Mn}(\text{CH}_3\text{CN})]^{2+}$  to form cluster  $[(\text{PY5Me}_2)_2\text{Mn}_2\text{ReCl}_4(\text{CN})_2]^{2+}$ . Orange, yellow, cyan, green, red, blue, and gray spheres represent Re, Mn, Zn, Cl, O, N, and C atoms, respectively; H atoms have been omitted for clarity.

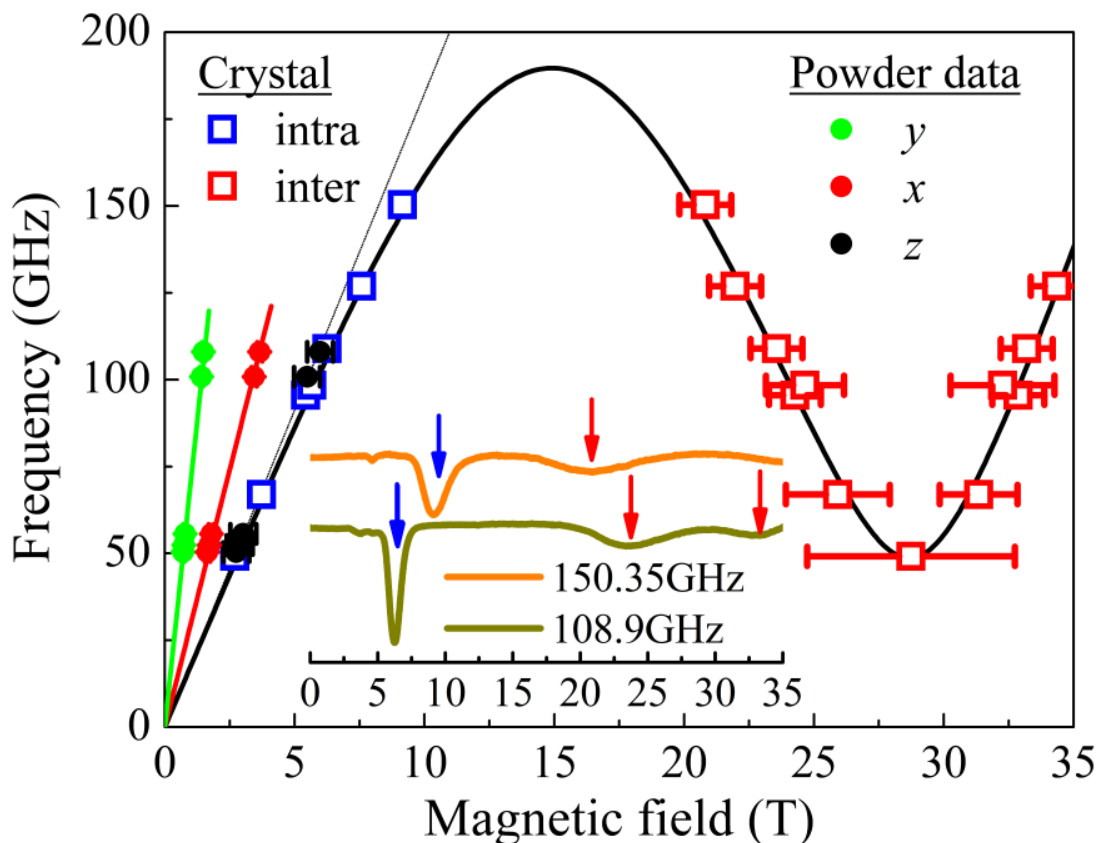


Figure 5-2. The EPR studies for complex **1**. (main panel) EPR peak positions observed for a single crystal of **1** at 1.3 K with the field aligned  $3^\circ$  away from the molecular  $z$ -axis; intra- and inter- Kramers transitions are marked with blue and red data points, respectively. Powder EPR data are included in the low field region; three components are observed at each frequency corresponding to the three components of the effective Lande  $g$  tensor associated with the lowest Kramers doublet (see legend). The solid lines represent the best simulation of the combined data sets (both single crystal and powder measurements), employing Eqn. (1) and the single set of Hamiltonian and parameters given in the main text. The thin solid line would be the expectation for the intra-Kramers transition in the absence of rhombic anisotropy ( $E = 0$ ); the data clearly depart from this expectation, providing a constraint on the  $E$  parameter. (inset) Representative single-crystal EPR spectra for **1** collected at 1.3 K demonstrating the observation of three ground state resonances; intra- and inter- Kramers transitions are marked with blue and red arrows, respectively.

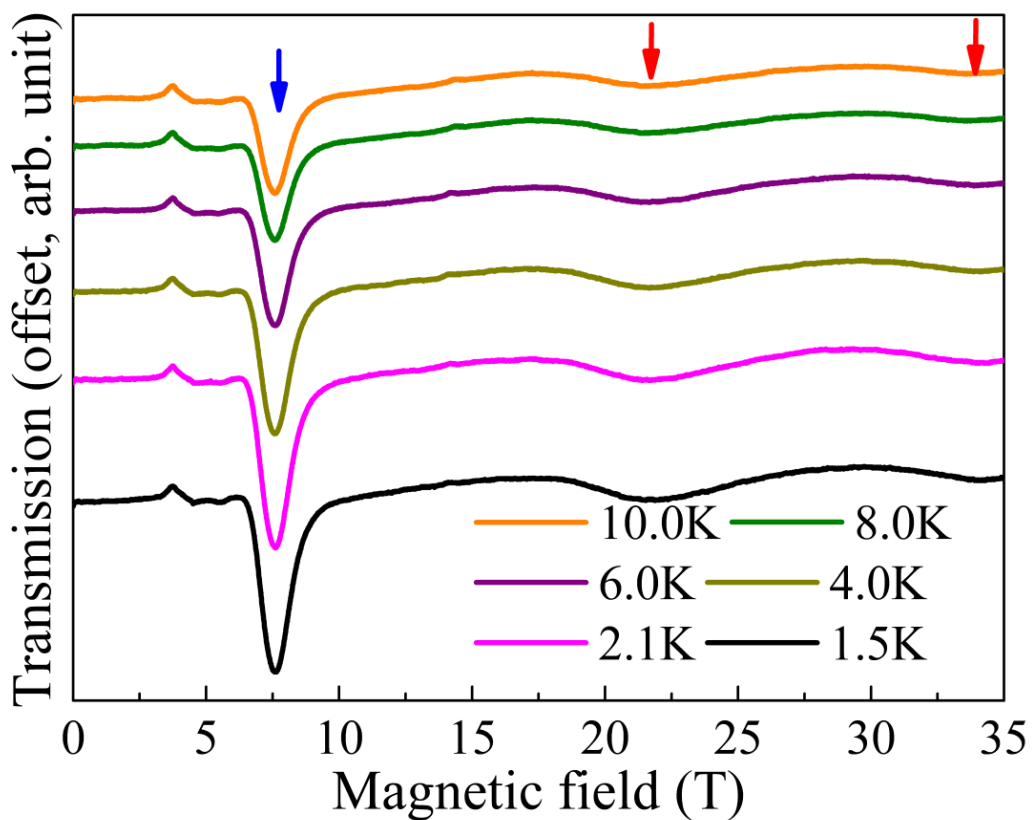


Figure 5-3. Temperature dependence spectra for **1** collected at  $f = 126.9$  GHz. All three resonances strengthen and persist to the lowest temperature, where  $k_B T \ll hf$ . This indicates that all of the transitions correspond to excitations from the ground state of the molecule, with the blue and red arrows denoting intra- and inter-Kramers transitions, respectively.

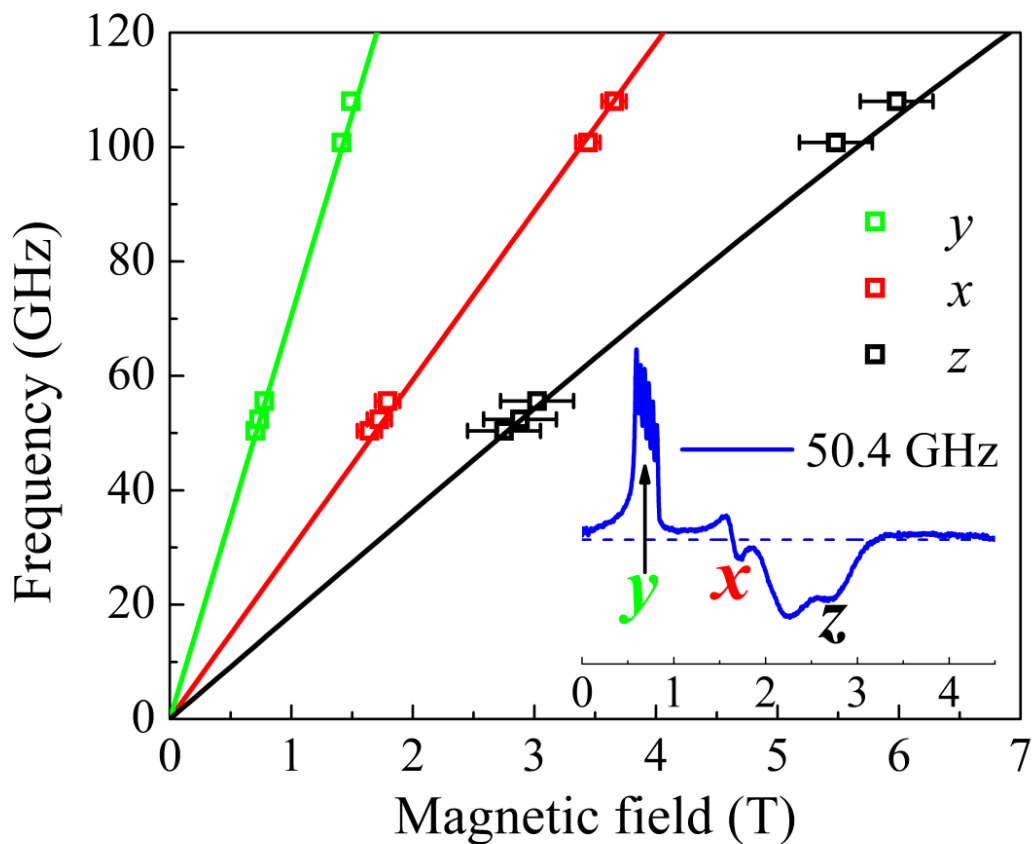


Figure 5-4. Frequency dependence of the high-frequency EPR peak positions deduced from studies of a powder sample of **1** at 5 K. A representative spectrum collected in the first-derivative mode at 50.4 GHz is displayed in the inset. Three branches of resonances are observed, corresponding to the three principal components of the effective Land  $g$  tensor associated with lowest Kramers doublet (field parallel to  $x$ ,  $y$  and  $z$ ). The fine structure seen in the  $y$ -component is due to nuclear hyperfine splitting; the  $y$  resonance position is chosen at the center of the fine structure spectrum. The solid lines in the main panel are simulations of the three resonance branches employing Equation 5-1 and the parameters given in the main text.

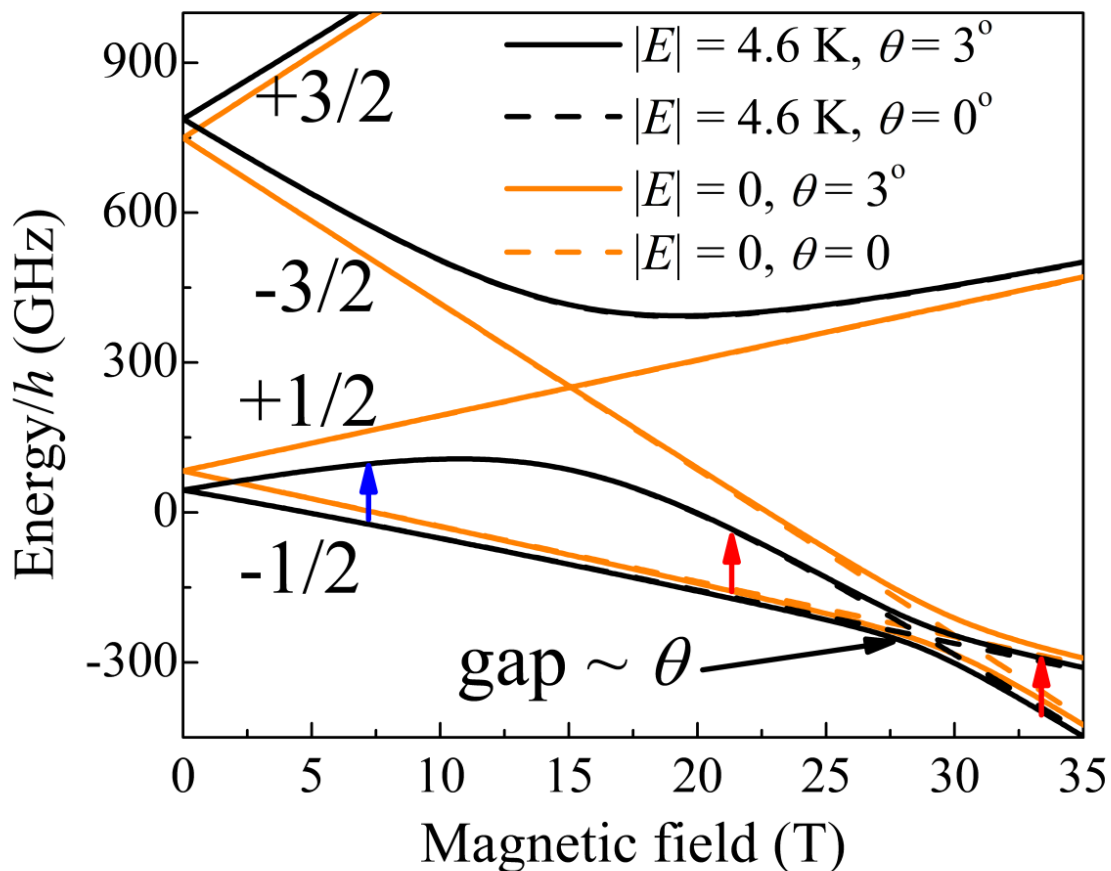


Figure 5-5. Zeeman diagram for complex **1** generated employing Equation 5-1 with  $D = +15.8$  K and  $g_z = 1.58$ . The figure is generated considering different  $E$  values and field misalignment angles  $\theta$  (see legend). The approximate spin projection ( $m_s$ ) of each state is labeled in the low-field region of the figure. The figure demonstrates that the avoided crossing at  $\sim 15$  T is determined entirely by  $E$ , while the one at  $\sim 28$  T is determined entirely by  $\theta$ . Consequently, different regions of the data in Figure 5-2 constrain these two parameters. The blue and red arrows correspond to the intra-Kramers and inter-Kramers transitions  $\sim 120$  GHz in single-crystal experiments, respectively.

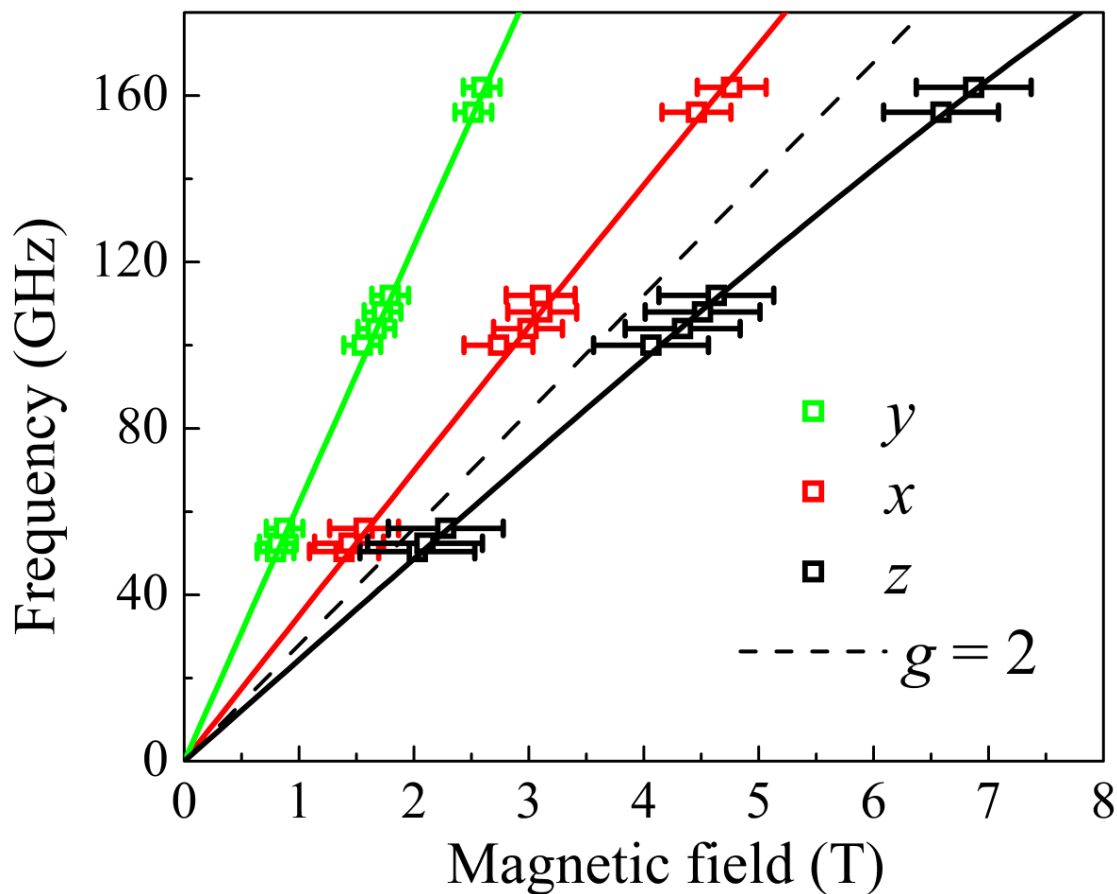


Figure 5-6. Frequency dependence of the EPR peak positions deduced from powder studies of complex **2** at 5 K. Three resonance branches are observed, corresponding to the three principal components of the effective Lande- $g$  tensor associated with the lowest Kramers doublet (field parallel to  $x$ ,  $y$  and  $z$ ). The solid lines are best simulations employing Equation 5-1 and the parameters discussed in the main text. The dashed line represents the  $g = 2.00$  position. The observation of one resonance above  $g = 2.00$ , and two below, is indicative of easy-plane-type anisotropy (see main text for further explanation).

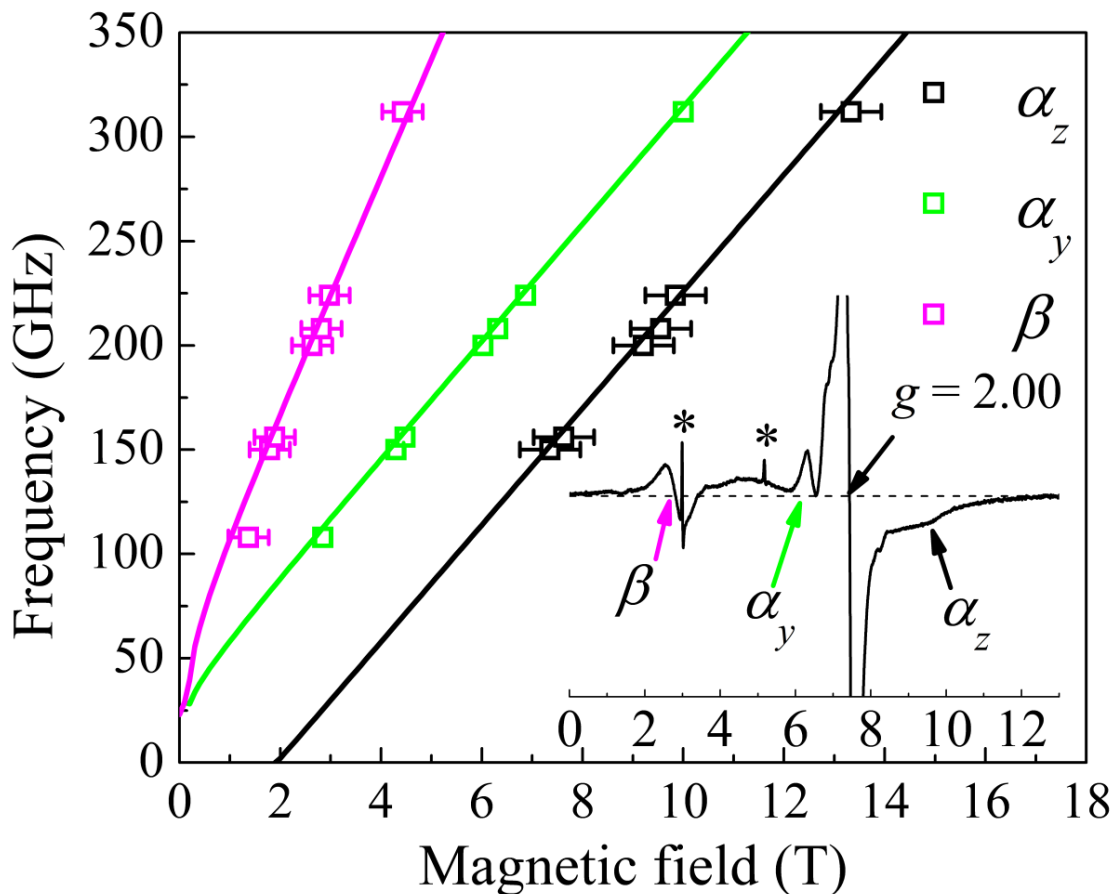


Figure 5-7. Frequency dependence of the EPR peak positions obtained from studies of a powder sample of **3** at 3.5 K. The inset displays a representative spectrum collected in first-derivative mode at 208 GHz. The strong truncated feature at  $g = 2.00$  is likely due to paramagnetic impurities and/or uncoupled  $\text{Mn}^{\text{II}}$  centers, while the sharp signals marked with asterisks are impurity signals from molecular oxygen absorbed in the sample holder. The broader anisotropic signals labeled  $\alpha$  correspond to conventional  $\Delta m = 1$  transitions, while the  $\beta$  resonance corresponds to a double quantum transition (see main text for detailed explanation).

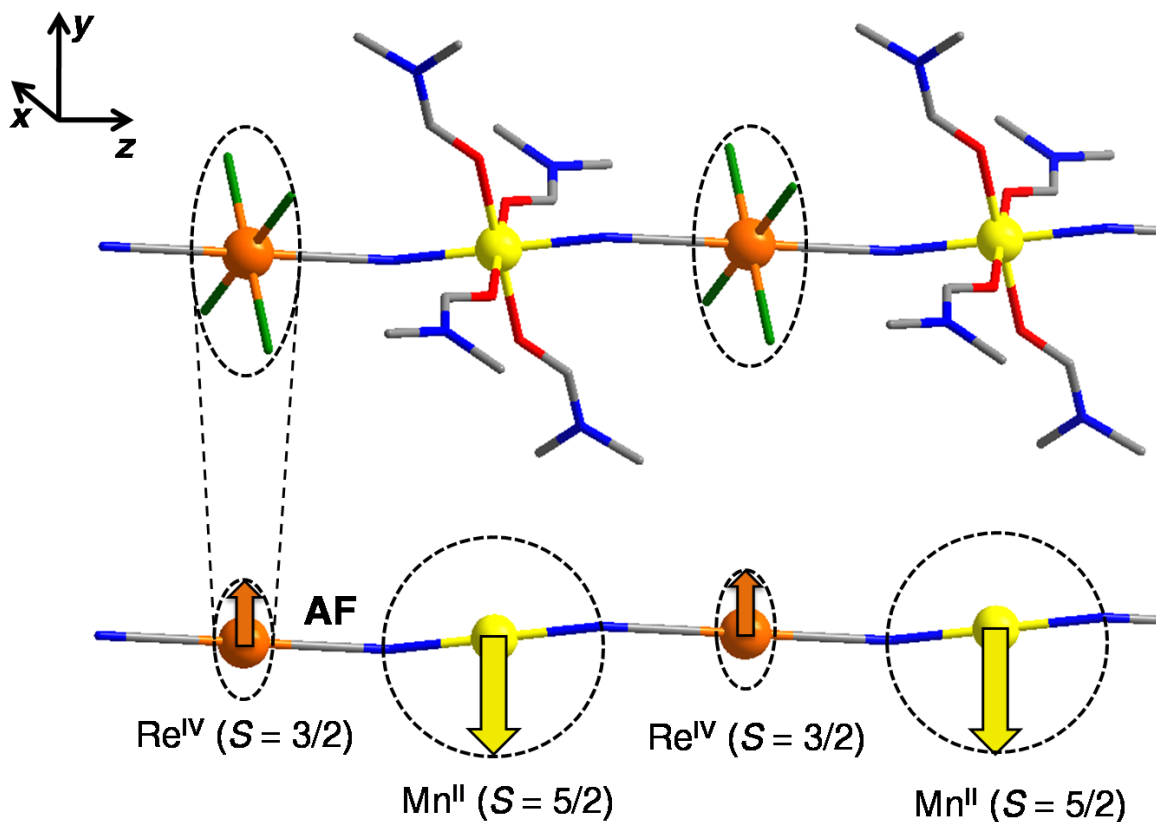


Figure 5-8. Structure and spin arrangement of chain compound **4**. The atoms are colored as follows: Re<sup>IV</sup> = orange, Mn<sup>II</sup> = yellow, Cl = green, N = blue, and C = gray. The black dashed circles denote the local  $xy$ -plane of each Re<sup>IV</sup> center, which is determined by the four coplanar chlorine atoms; the  $z$ -axis is parallel to the chain direction. In the classical ground state, the Mn<sup>II</sup> spins (yellow arrows) are locked into an antiparallel arrangement relative to those of the Re<sup>IV</sup> spins (orange arrows); the easy-plane anisotropy associated with the Re<sup>IV</sup> centers then constrains the spins within the  $xy$ -plane on both sub-lattices.

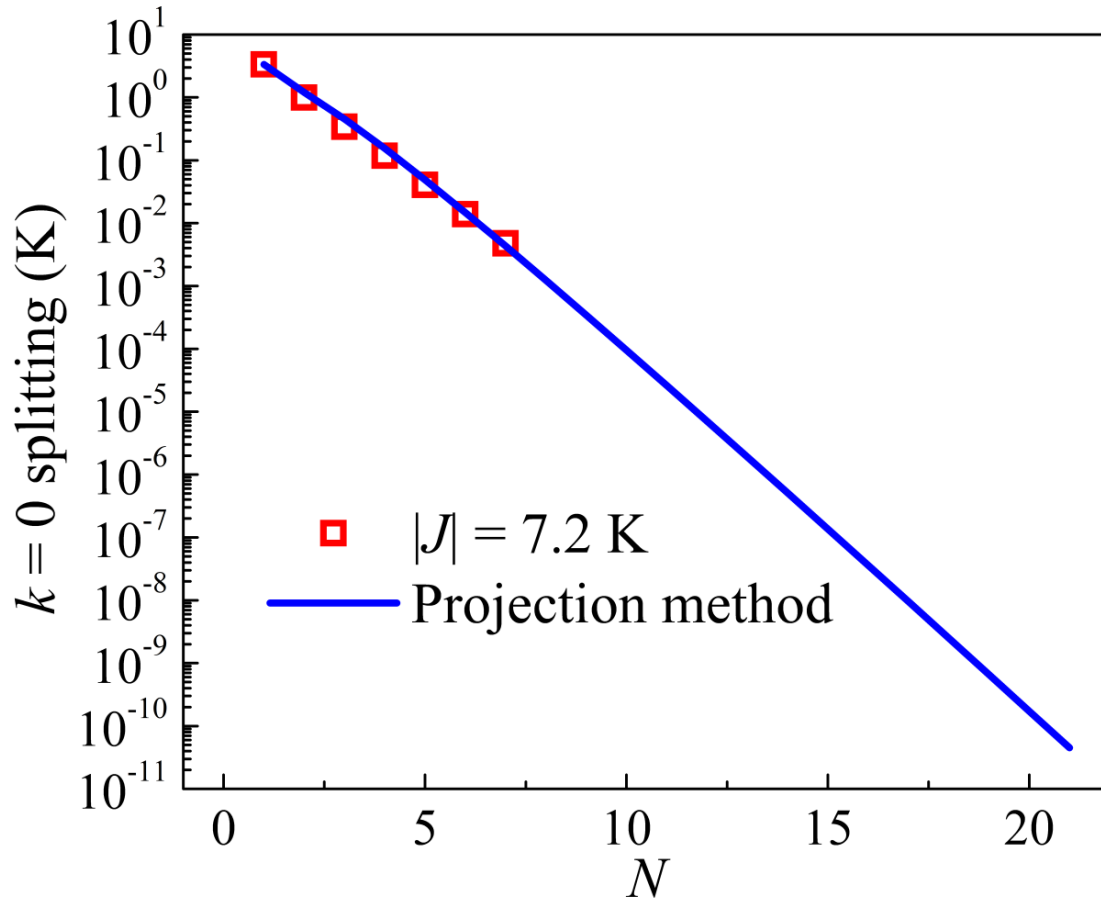


Figure 5-9. The ground tunnel splitting as a function of the size ( $N$ ) of the SCM. The red squares are the numerical simulations performed with  $|J| = 7.2$  K, and the blue solid line is calculated using the projection method. The gaps calculated by the two methods are essentially identical. Quantum fluctuations are exponentially suppressed as the length of a chain increases.

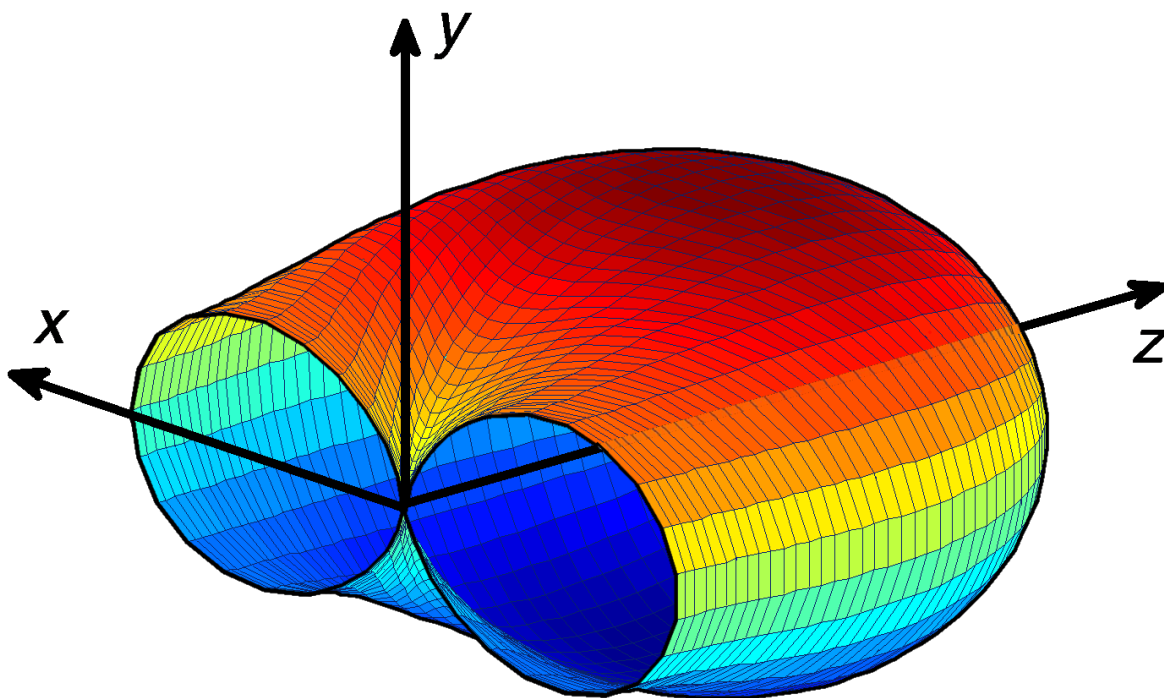


Figure 5-10. Classical magneto-anisotropy energy surface corresponding to the zero-field operator equivalent terms given in Equation 5-1. The surface was generated with  $D > 0$  and  $|E|/|D|$  equal to the ratio found from the present EPR experiments on complex **2**. The radial distance to the surface represents the energy of a spin as a function of its orientation; zero energy has been chosen to correspond to the case when the spin is parallel to  $y$ , and only the  $z > 0$  surface is shown in order to aid viewing of the cross-section in the  $xy$ -plane. As can be seen, the spin experiences an anisotropic kinetic barrier against reversal from  $+y$  to  $y$ , with the barrier minimum occurring along  $\pm x$ .

## CHAPTER 6 SUMMARY

This chapter gives a summary of the work presented in the preceding chapters. This dissertation is focused on studying both the quantum tunneling and thermally assisted relaxation of magnetization in two types of molecule-based magnets, namely single-molecule magnets (SMMs) and single-chain magnets (SCMs). High-frequency and/or high-field electron paramagnetic resonance (EPR) was used as the primary experimental technique in these studies. We also performed extensive numerical and theoretical studies in order to understand the insights into the interesting physics in SMMs and SCMs.

Chapter 1 gives a general introduction to SMMs and SCMs. We introduced two types of spin Hamiltonians, the giant-spin approximation (GSA) Hamiltonian and multi-spin (MS) Hamiltonian. In particular, we discussed the symmetries of the Stevens operators used in the GSA Hamiltonian, which decide the spin selection rules and Berry-phase interference (BPI) patterns associated with the quantum tunneling of magnetization (QTM). We also discussed Glauber's theory in the SCMs to illustrate the thermally assisted magnetic relaxation process in a one dimensional chain.

In Chapter 2, we presented EPR spectra for two  $[\text{Mn}^{\text{III}}]_2$  dinuclear molecular magnets, one ferromagnetic and the other antiferromagnetic. The obtained spectra were analyzed both by exact diagonalization and symmetry based perturbation calculations. In both cases, we have show that EPR is a particularly powerful technique in determining the magneto anisotropy,  $d$ , and exchange interactions,  $J$ , in weakly coupled molecular magnets, where  $J$  is rarely obtained in EPR studies on strongly coupled systems. Furthermore, these studies paved the way for using EPR to study the magneto-structural correlations in these molecules under pressure.

In Chapter 3, we presented several theoretical studies of QTM in a trinuclear  $[\text{Mn}^{\text{III}}]_3$  SMM with idealized  $C_3$  symmetry. By mapping the spectra obtained via a MS Hamiltonian onto a GSA Hamiltonian, we discovered that the three-fold transverse anisotropy,  $\hat{O}_4^3$ , arises when the Jahn-Teller axes of the  $\text{Mn}^{\text{III}}$  ions are tilted away from the molecular  $z$ -axis. The emergence of the  $\hat{O}_4^3$  operator unfreezes  $k$ -odd QTM resonances and shifts the  $k = 0$  ground QTM resonance away from zero longitudinal field. These studies demonstrated the correlations between molecular structure and the symmetry of the Hamiltonian. In addition, we considered QTM in a tetranuclear  $[\text{Ni}^{\text{II}}]_4$  SMM with idealized  $S_4$  symmetry. The studies for  $\text{Mn}_3$  and  $\text{Ni}_4$  illustrated that the ZFS anisotropies of a molecule can unfreezes  $k$ -odd QTM resonances without the presence of a transverse field, which emphasizes the importance of disorder in QTM.

In Chapter 4, we presented EPR and QTM studies on two mixed-valent  $[\text{Mn}_2^{\text{III}}\text{Mn}_2^{\text{II}}]$  SMMs. A motion of BPI minima was observed in the QTM experiments for  $\text{Mn}_4$ -Bet, which has been predicted, but never observed in SMMs. We found that this motion is due to the competition between the ZFS tensors of inequivalent Mn ions. We also showed that the asymmetric BPI pattern can originate from the competition between non-collinear ZFS tensors within a molecule, where a net antisymmetric interaction is forbidden by the structural symmetry of the molecule. These results signify the importance of symmetry in QTM of molecular magnets.

Finally, in Chapter 5, we presented our work on a  $\text{Re}^{\text{IV}}$  based SCM. EPR measurements were performed on three related molecules mimicking small fragments of the chain to elucidate the influences of the local coordinations and magnetic interactions on the anisotropy of the  $[\text{Re}^{\text{IV}}(\text{CN})_2\text{Cl}_4]^{2-}$  building block. The EPR spectra collected for all the three compounds indicate an easy-plane type anisotropy for  $\text{Re}^{\text{IV}}$  with a significant  $E$  term, which seems to be contradictory with the general strategy for building a SCM. Inspired by our findings, we developed a

theoretical model in which the relaxation barrier is determined by the transverse anisotropy,  $E$ , rather than axial anisotropy,  $D$ . Due to the macroscopic spin associated with the chain, QTM is suppressed, which leads to the observation of magnetic bistability induced by the transverse anisotropy. The theoretical barrier predicted by this model is in excellent agreement with the experimental results. This presents the first example of the observation of slow magnetic relaxation arising from  $E$  in either a SMM or SCM.

APPENDIX  
STEVENS OPERATORS

The  $\hat{O}_p^q$  ( $p \leq 6$ ) operators are defined as:

$$\hat{O}_2^0 = 3\hat{S}_z^2 - s$$

$$\hat{O}_2^1 = \frac{1}{2}[\hat{S}_z, \hat{S}_+ + \hat{S}_-]_+$$

$$\hat{O}_2^2 = \frac{1}{2}(\hat{S}_+^2 + \hat{S}_-^2)$$

$$\hat{O}_4^0 = 35\hat{S}_z^4 - (30s - 25)\hat{S}_z^2 + (3s^2 - 6s)$$

$$\hat{O}_4^1 = \frac{1}{2}[7\hat{S}_z^3 - (3s + 1)\hat{S}_z, \hat{S}_+ + \hat{S}_-]_+$$

$$\hat{O}_4^2 = \frac{1}{2}[7\hat{S}_z^2 - (s + 5), \hat{S}_+^2 + \hat{S}_-^2]_+$$

$$\hat{O}_4^3 = \frac{1}{2}[\hat{S}_z, \hat{S}_+^3 + \hat{S}_-^3]_+$$

$$\hat{O}_4^4 = \frac{1}{2}(\hat{S}_+^4 + \hat{S}_-^4)$$

$$\hat{O}_6^0 = 231\hat{S}_z^6 - (315s - 735)\hat{S}_z^4 + (105s^2 - 525s + 294)\hat{S}_z^2 + (5s^3 - 40s^2 - 60s)$$

$$\hat{O}_6^1 = \frac{1}{2}[33\hat{S}_z^5 - (30s - 15)\hat{S}_z^3 + (5s^2 - 10s + 12)\hat{S}_z, \hat{S}_+ + \hat{S}_-]_+$$

$$\hat{O}_6^2 = \frac{1}{2}[33\hat{S}_z^4 - (18s + 123)\hat{S}_z^2 + (s^2 + 10s + 102), \hat{S}_+^2 + \hat{S}_-^2]_+$$

$$\hat{O}_6^3 = \frac{1}{2}[11\hat{S}_z^3 - (3s + 59)\hat{S}_z, \hat{S}_+^3 + \hat{S}_-^3]_+$$

$$\hat{O}_6^4 = \frac{1}{2}[11\hat{S}_z^2 - (s + 38), \hat{S}_+^4 + \hat{S}_-^4]_+$$

$$\hat{O}_6^5 = \frac{1}{2}[\hat{S}_z, \hat{S}_+^5 + \hat{S}_-^5]_+$$

$$\hat{O}_6^6 = \frac{1}{2}(\hat{S}_+^6 + \hat{S}_-^6)$$

where  $[A, B]_+ = (AB + BA)/2$  and  $s = S(S+1)$ .

## LIST OF REFERENCES

- [1] D. Gatteschi, R. Sessoli, and J. Villain, *Molecular Nanomagnets* (Oxford University Press, Oxford, 2006).
- [2] M. N. Leuenberger and D. Loss, *Nature* **410**, 789 (2001).
- [3] M. Affronte, F. Troiani, A. Ghirri, A. Candini, M. Evangelisti, V. Corradini, S. Carretta, P. Santini, G. Amoretti, F. Tuna, G. Timco, and R. E. P. Winpenny, *J. Phys. D: Appl. Phys.* **40**, 2999 (2007).
- [4] A. Caneschi, D. Gatteschi, R. Sessoli, A. L. Barra, L. C. Brunel, and M. Guillot, *J. Am. Chem. Soc.* **113**, 5873 (1991).
- [5] J. R. Friedman, M. P. Sarachik, J. Tejada, and R. Ziolo, *Phys. Rev. Lett.* **76**, 3830 (1996).
- [6] S. M. J. Aubin, M. W. Wemple, D. M. Adams, H.-L. Tsai, G. Christou, and D. N. Hendrickson, *J. Am. Chem. Soc.* **118**, 7746 (1996).
- [7] M. R. Cheesman, V. S. Oganessian, R. Sessoli, D. Gatteschi, and A. J. Thomson, *Chem. Commun.* (1997).
- [8] T. Lis, *Acta Crystallographica Section B* **36**, 2042 (1980).
- [9] A. L. Barra and et al., *EPL (Europhysics Letters)* **35**, 133 (1996).
- [10] A. L. Barra, A. Caneschi, A. Cornia, F. Fabrizi de Biani, D. Gatteschi, C. Sangregorio, R. Sessoli, and L. Sorace, *J. Am. Chem. Soc.* **121**, 5302 (1999).
- [11] W. Wernsdorfer, N. Aliaga-Alcalde, D. N. Hendrickson, and G. Christou, *Nature* **416**, 406 (2002).
- [12] S. Hill, R. S. Edwards, N. Aliaga-Alcalde, and G. Christou, *Science* **302**, 1015 (2003).
- [13] E.-C. Yang, C. Kirman, J. Lawrence, L. N. Zakharov, A. L. Rheingold, S. Hill, and D. N. Hendrickson, *Inorg. Chem.* **44**, 3827 (2005).
- [14] A. J. Tasiopoulos, A. Vinslava, W. Wernsdorfer, K. A. Abboud, and G. Christou, *Angew. Chem.* **116**, 2169 (2004).
- [15] C. J. Milios, A. Vinslava, W. Wernsdorfer, S. Moggach, S. Parsons, S. P. Perlepes, G. Christou, and E. K. Brechin, *J. Am. Chem. Soc.* **129**, 2754 (2007).
- [16] P. L. Feng, C. Koo, J. J. Henderson, P. Manning, M. Nakano, E. del Barco, S. Hill, and D. N. Hendrickson, *Inorg. Chem.* **48**, 3480 (2009).

- [17] D. E. Freedman, W. H. Harman, T. D. Harris, G. J. Long, C. J. Chang, and J. R. Long, *J. Am. Chem. Soc.* **132**, 1224 (2010).
- [18] R. Sessoli, H. L. Tsai, A. R. Schake, S. Wang, J. B. Vincent, K. Folting, D. Gatteschi, G. Christou, and D. N. Hendrickson, *J. Am. Chem. Soc.* **115**, 1804 (1993).
- [19] D. Gatteschi, A. Caneschi, L. Pardi, and R. Sessoli, *Science* **265**, 1054 (1994).
- [20] F. Branzoli, P. Carretta, M. Filibian, G. Zoppellaro, M. J. Graf, J. R. Galan-Mascaros, O. Fuhr, S. Brink, and M. Ruben, *J. Am. Chem. Soc.* **131**, 4387 (2009).
- [21] J. D. Rinehart, M. Fang, W. J. Evans, and J. R. Long, *J. Am. Chem. Soc.* **133**, 14236 (2011).
- [22] J. D. Rinehart, M. Fang, W. J. Evans, and J. R. Long, *Nat Chem* **3**, 538 (2011).
- [23] I. J. Hewitt, J. Tang, N. T. Madhu, C. E. Anson, Y. Lan, J. Luzon, M. Etienne, R. Sessoli, and A. K. Powell, *Angew. Chem. Int. Ed.* **49**, 6352 (2010).
- [24] M. Hołyńska, D. Premužić, I.-R. Jeon, W. Wernsdorfer, R. Clérac, and S. Dehnen, *Chemistry – A European Journal* **17**, 9605 (2011).
- [25] P.-H. Lin, T. J. Burchell, R. Clérac, and M. Murugesu, *Angew. Chem.* **120**, 8980 (2008).
- [26] P.-H. Lin, T. J. Burchell, L. Ungur, L. F. Chibotaru, W. Wernsdorfer, and M. Murugesu, *Angew. Chem. Int. Ed.* **48**, 9489 (2009).
- [27] C. Papatriantafyllopoulou, W. Wernsdorfer, K. A. Abboud, and G. Christou, *Inorg. Chem.* **50**, 421 (2010).
- [28] E. M. Chudnovsky and J. Tejada, *Macroscopic Quantum Tunneling of the Magnetic Moment* (Cambridge University Press, 2005).
- [29] A. Abragam and B. Bleaney, *Electron paramagnetic resonance of transition ions* (Dover, New York, 1986).
- [30] C. Rudowicz and C. Y. Chung, *J. Phys.: Condens. Matter* **16**, 5825 (2004).
- [31] S. Takahashi, R. S. Edwards, J. M. North, S. Hill, and N. S. Dalal, *Phys. Rev. B* **70**, 094429 (2004).
- [32] A. L. Barra, D. Gatteschi, and R. Sessoli, *Chemistry – A European Journal* **6**, 1608 (2000).
- [33] C. Kirman, J. Lawrence, S. Hill, E.-C. Yang, and D. N. Hendrickson, *J. Appl. Phys.* **97**, 10M501 (2005).

- [34] S. Carretta, E. Livioti, N. Magnani, P. Santini, and G. Amoretti, *Phys. Rev. Lett.* **92**, 207205 (2004).
- [35] A. Wilson, J. Lawrence, E. C. Yang, M. Nakano, D. N. Hendrickson, and S. Hill, *Phys. Rev. B* **74**, 140403 (2006).
- [36] C. M. Ramsey, E. del Barco, S. Hill, S. J. Shah, C. C. Beedle, and D. N. Hendrickson, *Nat Phys* **4**, 277 (2008).
- [37] S. Hill, S. Datta, J. Liu, R. Inglis, C. J. Milios, P. L. Feng, J. J. Henderson, E. del Barco, E. K. Brechin, and D. N. Hendrickson, *Dalton Trans.* **39**, 4693 (2010).
- [38] O. Pieper, T. Guidi, S. Carretta, J. van Slageren, F. El Hallak, B. Lake, P. Santini, G. Amoretti, H. Mutka, M. Koza, M. Russina, A. Schnegg, C. J. Milios, E. K. Brechin, A. Julià and J. Tejada, *Phys. Rev. B* **81**, 174420 (2010).
- [39] W. Wernsdorfer and R. Sessoli, *Science* **284**, 133 (1999).
- [40] J. Liu, B. Wu, L. Fu, R. B. Diener, and Q. Niu, *Phys. Rev. B* **65**, 224401 (2002).
- [41] W. Wernsdorfer, R. Sessoli, A. Caneschi, D. Gatteschi, A. Cornia, and D. Mailly, *J. Appl. Phys.* **87**, 5481 (2000).
- [42] L. D. Landau, *Phys. Z. Sowjetunion* **2**, 46 (1932).
- [43] E. C. G. Stueckelberg, *Helv. Phys. Acta* **5**, 369 (1932).
- [44] C. Zener, *Proceedings of the Royal Society of London. Series A* **137**, 696 (1932).
- [45] S. Miyashita, *J. Phys. Soc. Jpn.* **64**, 3207 (1995).
- [46] G. Rose and P. C. E. Stamp, *J. Low Temp. Phys.* **113**, 1153 (1998).
- [47] N. A. Sinitsyn and N. Prokof'ev, *Phys. Rev. B* **67**, 134403 (2003).
- [48] A. Vijayaraghavan and A. Garg, *Phys. Rev. B* **79**, 104423 (2009).
- [49] D. A. Garanin and R. Schilling, *Phys. Rev. B* **71**, 184414 (2005).
- [50] E. M. Chudnovsky and D. A. Garanin, *Phys. Rev. Lett.* **87**, 187203 (2001).
- [51] K. M. Mertes, Y. Suzuki, M. P. Sarachik, Y. Paltiel, H. Shtrikman, E. Zeldov, E. Rumberger, D. N. Hendrickson, and G. Christou, *Phys. Rev. Lett.* **87**, 227205 (2001).
- [52] A. Garg, *EPL (Europhysics Letters)* **22**, 205 (1993).

- [53] D. Loss, D. P. DiVincenzo, and G. Grinstein, *Phys. Rev. Lett.* **69**, 3232 (1992).
- [54] J. von Delft and C. L. Henley, *Phys. Rev. Lett.* **69**, 3236 (1992).
- [55] P. Bruno, *Phys. Rev. Lett.* **96**, 117208 (2006).
- [56] M. V. Berry and M. Wilkinson, *Proceedings of the Royal Society of London. A. Mathematical and Physical Sciences* **392**, 15 (1984).
- [57] A. Caneschi, D. Gatteschi, N. Lalioti, C. Sangregorio, R. Sessoli, G. Venturi, A. Vindigni, A. Rettori, M. G. Pini, and M. A. Novak, *Angew. Chem. Int. Ed.* **40**, 1760 (2001).
- [58] R. Cl  rac, H. Miyasaka, M. Yamashita, and C. Coulon, *J. Am. Chem. Soc.* **124**, 12837 (2002).
- [59] P. Gambardella, A. Dallmeyer, K. Maiti, M. C. Malagoli, W. Eberhardt, K. Kern, and C. Carbone, *Nature* **416**, 301 (2002).
- [60] M. Ferbinteanu, H. Miyasaka, W. Wernsdorfer, K. Nakata, K.-i. Sugiura, M. Yamashita, C. Coulon, and R. Cl  rac, *J. Am. Chem. Soc.* **127**, 3090 (2005).
- [61] T. Kajiwara, M. Nakano, Y. Kaneko, S. Takaishi, T. Ito, M. Yamashita, A. Igashira-Kamiyama, H. Nojiri, Y. Ono, and N. Kojima, *J. Am. Chem. Soc.* **127**, 10150 (2005).
- [62] H. Miyasaka, T. Madanbashi, K. Sugimoto, Y. Nakazawa, W. Wernsdorfer, K.-i. Sugiura, M. Yamashita, C. Coulon, and R. Cl  rac, *Chemistry – A European Journal* **12**, 7028 (2006).
- [63] T. D. Harris, M. V. Bennett, R. Clerac, and J. R. Long, *J. Am. Chem. Soc.* **132**, 3980 (2010).
- [64] H. Miyasaka, M. Julve, M. Yamashita, and R. Clerac, *Inorg. Chem.* **48**, 3420 (2009).
- [65] R. J. Glauber, *Journal of Mathematical Physics* **4**, 294 (1963).
- [66] B. Barbara, *Journal De Physique* **34**, 1039 (1973).
- [67] J. H. Luscombe, M. Luban, and J. P. Reynolds, *Phys. Rev. E* **53**, 5852 (1996).
- [68] H. Miyasaka, T. Madanbashi, A. Saitoh, N. Motokawa, R. Ishikawa, M. Yamashita, S. Bahr, W. Wernsdorfer, and R. Cl  rac, *Chemistry – A European Journal* **18**, 3942 (2012).
- [69] R. Inglis, E. Houton, J. Liu, A. Prescimone, J. Cano, S. Piligkos, S. Hill, L. F. Jones, and E. K. Brechin, *Dalton Trans.* **40**, 9999 (2011).

- [70] G. Arom í P. Gamez, O. Roubeau, P. C. Berzal, H. Kooijman, A. L. Spek, W. L. Driessen, and J. Reedijk, *Inorg. Chem.* **41**, 3673 (2002).
- [71] M. Mola, S. Hill, P. Goy, and M. Gross, *Rev. Sci. Instrum.* **71**, 186 (2000).
- [72] S. Takahashi and S. Hill, *Rev. Sci. Instrum.* **76**, 023114 (2005).
- [73] S. Hill, R. S. Edwards, S. I. Jones, N. S. Dalal, and J. M. North, *Phys. Rev. Lett.* **90**, 217204 (2003).
- [74] S. Hill, N. Anderson, A. Wilson, S. Takahashi, N. E. Chakov, M. Murugesu, J. M. North, N. S. Dalal, and G. Christou, *J. Appl. Phys.* **97**, 10M510 (2005).
- [75] J. Lawrence, E.-C. Yang, R. Edwards, M. M. Olmstead, C. Ramsey, N. S. Dalal, P. K. Gantzel, S. Hill, and D. N. Hendrickson, *Inorg. Chem.* **47**, 1965 (2008).
- [76] J. Lawrence, E. C. Yang, D. N. Hendrickson, and S. Hill, *PCCP* **11**, 6743 (2009).
- [77] K. Park, M. A. Novotny, N. S. Dalal, S. Hill, and P. A. Rikvold, *Phys. Rev. B* **65**, 014426 (2001).
- [78] S. Hill, S. Maccagnano, K. Park, R. M. Achey, J. M. North, and N. S. Dalal, *Phys. Rev. B* **65**, 224410 (2002).
- [79] D. E. Graf, R. L. Stillwell, K. M. Purcell, and S. W. Tozer, *High Pressure Research* **31**, 533 (2011).
- [80] E. del Barco, S. Hill, C. C. Beedle, D. N. Hendrickson, I. S. Tupitsyn, and P. C. E. Stamp, *Phys. Rev. B* **82**, 104426 (2010).
- [81] A. K. Hassan, L. A. Pardi, J. Krzystek, A. Sienkiewicz, P. Goy, M. Rohrer, and L. C. Brunel, *Journal of Magnetic Resonance* **142**, 300 (2000).
- [82] J. Krzystek, A. Ozarowski, and J. Telser, *Coord. Chem. Rev.* **250**, 2308 (2006).
- [83] A. Garg, *Phys. Rev. Lett.* **83**, 4385 (1999).
- [84] F. Li and A. Garg, *Phys. Rev. B* **83**, 132401 (2011).
- [85] C.-S. Park and A. Garg, *Phys. Rev. B* **65**, 064411 (2002).
- [86] E. Keçecioglu and A. Garg, *Phys. Rev. Lett.* **88**, 237205 (2002).
- [87] E. del Barco, A. D. Kent, S. Hill, J. M. North, N. S. Dalal, E. M. Rumberger, D. N. Hendrickson, N. Chakov, and G. Christou, *J. Low Temp. Phys.* **140**, 119 (2005).

- [88] M. S. Foss-Feig and R. F. Jonathan, EPL (Europhysics Letters) **86**, 27002 (2009).
- [89] W. Wernsdorfer, S. Bhaduri, C. Boskovic, G. Christou, and D. N. Hendrickson, Phys. Rev. B **65**, 180403 (2002).
- [90] P. L. Feng, C. Koo, J. J. Henderson, M. Nakano, S. Hill, E. del Barco, and D. N. Hendrickson, Inorg. Chem. **47**, 8610 (2008).
- [91] J. J. Henderson, C. Koo, P. L. Feng, E. del Barco, S. Hill, I. S. Tupitsyn, P. C. E. Stamp, and D. N. Hendrickson, Phys. Rev. Lett. **103**, 017202 (2009).
- [92] E.-C. Yang, W. Wernsdorfer, S. Hill, R. S. Edwards, M. Nakano, S. Maccagnano, L. N. Zakharov, A. L. Rheingold, G. Christou, and D. N. Hendrickson, Polyhedron **22**, 1727 (2003).
- [93] E.-C. Yang, W. Wernsdorfer, L. N. Zakharov, Y. Karaki, A. Yamaguchi, R. M. Isidro, G.-D. Lu, S. A. Wilson, A. L. Rheingold, H. Ishimoto, and D. N. Hendrickson, Inorg. Chem. **45**, 529 (2005).
- [94] G. Redler, C. Lampropoulos, S. Datta, C. Koo, T. C. Stamatatos, N. E. Chakov, G. Christou, and S. Hill, Phys. Rev. B **80**, 094408 (2009).
- [95] J. O. D. George F. Koster, Pobert G. Wheeler and Hermann Statz, *Properties of the Thirty-Two Point Groups* (M.I.T. Press, Cambridge, MA, 1963).
- [96] F. A. Cotton, *Chemical Applications of Group Theory* (A Wiley-Interscience Publication, 1990).
- [97] J. van Slageren, S. Vongtragool, B. Gorshunov, A. Mukhin, and M. Dressel, Phys. Rev. B **79**, 224406 (2009).
- [98] E. Liviotti, S. Carretta, and G. Amoretti, The Journal of Chemical Physics **117**, 3361 (2002).
- [99] A.-L. Barra, A. Caneschi, A. Cornia, D. Gatteschi, L. Gorini, L.-P. Heiniger, R. Sessoli, and L. Sorace, J. Am. Chem. Soc. **129**, 10754 (2007).
- [100] R. Maurice, eacute, mi, C. de Graaf, Guih, and N. ry, Phys. Rev. B **81**, 214427 (2010).
- [101] J. Liu, C. Koo, A. Amjad, P. L. Feng, E. S. Choi, E. del Barco, D. N. Hendrickson, and S. Hill, Phys. Rev. B **84**, 094443 (2011).
- [102] H. M. Quddusi, J. Liu, S. Singh, K. J. Heroux, E. del Barco, S. Hill, and D. N. Hendrickson, Phys. Rev. Lett. **106**, 227201 (2011).

- [103] K. J. Heroux, H. M. Quddusi, J. Liu, J. R. O'Brien, M. Nakano, E. del Barco, S. Hill, and D. N. Hendrickson, *Inorg. Chem.* **50**, 7367 (2011).
- [104] J. Liu, C. C. Beedle, H. M. Quddusi, E. d. Barco, D. N. Hendrickson, and S. Hill, *Polyhedron* **30**, 2965 (2011).
- [105] C. C. Beedle, University of Californian, San Diego, 2010.
- [106] J. C. Hempel, *The Journal of Chemical Physics* **64**, 4307 (1976).
- [107] W. B. Lynch, R. S. Boorse, and J. H. Freed, *J. Am. Chem. Soc.* **115**, 10909 (1993).
- [108] K. Hijii and S. Miyashita, *Phys. Rev. B* **78**, 214434 (2008).
- [109] J. Liu, E. del Barco, and S. Hill, *Phys. Rev. B* **85**, 012406 (2012).
- [110] S. Bahr, C. J. Milios, L. F. Jones, E. K. Brechin, V. Mosser, and W. Wernsdorfer, *Phys. Rev. B* **78**, 132401 (2008).
- [111] W. Wernsdorfer, T. C. Stamatatos, and G. Christou, *Phys. Rev. Lett.* **101**, 237204 (2008).
- [112] O. Waldmann, A. M. Ako, H. U. Güdel, and A. K. Powell, *Inorg. Chem.* **47**, 3486 (2008).
- [113] Y. Sanakis, M. Pissas, J. Krzystek, J. Telsler, and R. G. Raptis, *Chem. Phys. Lett.* **493**, 185 (2010).
- [114] J. M. Zadrozny, J. Liu, N. A. Piro, C. J. Chang, S. Hill, and J. R. Long, *Chem. Commun.* (2012).
- [115] C. Coulon, Cl, eacute, R. rac, L. Lecren, W. Wernsdorfer, and H. Miyasaka, *Phys. Rev. B* **69**, 132408 (2004).
- [116] L. Bogani, A. Vindigni, R. Sessoli, and D. Gatteschi, *J. Mater. Chem.* **18**, 4750 (2008).
- [117] A. Tomkiewicz, F. Villain, and J. Mrozinski, *J. Mol. Struct.* **555**, 383 (2000).
- [118] A. Tomkiewicz, T. J. Bartczak, R. Kruszyński, and J. Mroziński, *J. Mol. Struct.* **595**, 225 (2001).
- [119] J. Martínez-Lillo, D. Armentano, G. De Munno, F. Lloret, M. Julve, and J. Faus, *Inorg. Chim. Acta* **359**, 4343 (2006).
- [120] A. Bencini and D. Gatteschi, *Electron Paramagnetic Resonance of Exchange Coupled Clusters* (Springer, Berlin, 1990).

## BIOGRAPHICAL SKETCH

Junjie Liu was born in Changsha, the capital city of Hunan province, in China. He spent the early part of his education in Changsha. In the summer of 2003, he graduated from high school and joined the Tsinghua University in Beijing, China. During his undergraduate studies, Junjie Liu joined the program called “fundamental science, mathematics and physics” which emphasizes fundamental education in both mathematics and physics. In 2007, he received his bachelor degree in physics from Tsinghua University and then joined the University of Florida in Gainesville, Florida, in the same year.

After finished his core courses, Junjie Liu joined Dr. Stephen Hill's lab in the summer of 2008. Later in 2009, he moved with Dr. Hill's lab to the National High Magnetic Field Laboratory at Tallahassee, where he kept working on his research projects. His PhD project mainly focuses on using high-frequency/high-field electron paramagnetic resonance to study the spin dynamics in molecule-based magnets. These projects include wide-range collaborative interdisciplinary research projects with condensed matter physics and inorganic chemistry groups. Meanwhile, he also carried out many theoretical studies to understand the correlations between the symmetry and quantum tunneling of magnetizations in molecule-based magnets.